Aus dem Nationalen Zentrum für Strahlenforschung in der Onkologie – OncoRay
Direktorin: Prof. Dr. Mechthild Krause

Technical Feasibility of MR-Integrated Proton Therapy: Beam Deflection and Image Quality

D i s s e r t a t i o n s s c h r i f t

zur Erlangung des akademischen Grades
Doktor der Medizintechnologie
Doctor rerum medicinalium (Dr. rer. medic.)

vorgelegt

der Medizinischen Fakultät Carl Gustav Carus
der Technischen Universität Dresden

von

Sonja Schellhammer
aus Mannheim

Dresden 2019

1. Gutachter: Prof. Dr. Wolfgang Enghardt

2. Gutachter: Prof. Dr. Oliver Jäkel

Tag der mündlichen Prüfung: 10. April 2019

gez.: .....

Prof. Dr. Esther Troost

Vorsitzende der Promotionskommission

Contents

List of Figures

List of Tables

1 General Introduction

Cancer is one of the leading causes of death and morbidity worldwide (Steward and Wild, 2014). While incidence has been rising, the mortality rate has been decreasing over the last decades for most tumour sites, which can be attributed to improvements in diagnosis and treatment (American Cancer Society, 2017). Radiation therapy is, next to surgery and chemotherapy, one of the main modalities used for cancer treatment, and is used to treat about half of all cancer patients (Rosenblatt and Zubizarreta, 2017).

The goal of radiotherapy is to impede proliferation of tumour cells by damaging the genetic material through ionising radiation (Baskar et al., 2012). This technique can be applied with either curative or palliative intent, either solely or in combination with surgery or chemotherapy, with either external or internal ionising radiation sources, and using different types of radiation (Baskar et al., 2012). Current developments are targeted on increasing tumour control rates while sparing healthy tissue in order to reduce inadvertent side effects (Baumann et al., 2016).

Proton therapy is a type of external beam radiation treatment that uses high-energy protons to treat cancer. As compared to conventional, photon-based radiotherapy, its main advantage lies in a pronounced dose maximum, the Bragg peak, which can be tailored to a predefined tumour volume while sparing healthy tissue behind the tumour (Jäkel, 2009). However, the steep gradient of this maximum and the dependence of its position on the traversed material make the dose distribution very sensitive to inter- and intrafractional uncertainties resulting from setup errors and anatomical variations (i.e. organ motion and deformation), which gives rise to considerable range uncertainties (Lomax, 2008). About 75 % of cancer cases worldwide involve solid tumours situated in the thorax and abdomen (Bray et al., 2018), which makes them prone to motion uncertainties due to respiration, cardiac motion, and digestion.

The aim of real-time image-guided radiotherapy is to reduce these uncertainties by imaging essential parts of the patient anatomy in treatment position during irradiation. Ideally, tissue motions and deformations shall be tracked in real-time, such that dynamic beam de-

livery with enhanced dose conformality and reduced safety margins is rendered possible. Magnetic resonance imaging (MRI) has been suggested to be a promising candidate for this task, offering a fast real-time imaging modality with excellent soft tissue contrast without using ionising radiation for image formation (Lagendijk et al., 2014a). The concept feasibility to integrate MRI with photon-based radiotherapy into a hybrid system has been shown by several research groups (Lagendijk et al., 2014b; Fallone, 2014; Keall et al., 2014).

Because of the increased sensitivity of proton therapy to anatomical variations, this technique is expected to profit even more from an integration with MRI than photon-based radiotherapy. However, as of the beginning of this work in 2015, MR-integrated proton therapy (MRiPT) has only been described as a hypothetical modality in simulation studies, since there are specific technological and physical problems that need to be solved before clinical implementation (Schippers and Lomax, 2011; Oborn et al., 2017). Specifically, the therapeutic protons, being charged particles, will be deflected by the magnetic field of the MR scanner (Raaymakers et al., 2008) and, vice versa, the MR image quality may be affected by the electromagnetic fields of the proton therapy facility and by the beam itself.

So far, the accuracy of deflection predictions has not been evaluated, and no experimental data exists on either the deflection or MR image quality in an integrated setup. In order to assess the technical feasibility of MRiPT, the aim of this thesis is therefore to quantify and improve the accuracy of magnetic-field induced proton beam deflection calculations in media (chapter 3), and to analyse and quantify the effects of the proton therapy facility and the proton beam on MR images in a first experimental MRiPT setup (chapter 4).

In preparation to this, the physical principles of proton therapy, MR imaging and MR-integrated radiotherapy are outlined in sections 2.1 to 2.3. On this basis, the rationale and challenges for MR-integrated proton therapy are specified, the state of the art is summarised, and the research objectives of this work are defined (section 2.4). The advances in knowledge and implications for future research of this work are discussed in section 5. The work is concluded in section 6 by a summary in English and German language.

2 State of the Art: Proton Therapy and Magnetic Resonance Imaging

2.1 Proton Therapy

Proton beams have gained increasing interest for radiotherapeutic applications in the last years. Since the first treatment in 1954, about 150 000 patients have been treated worldwide, and there are 81 proton facilities in operation and further 73 in a planning stage or under construction (Particle Therapy Co-Operative Group, 2018). The main reason for this development in spite of the increased costs lies in the energy deposition mechanism of protons, which differs from the one of uncharged particles such as conventionally used X-rays. This mechanism, as well as the beam generation principle and the role of organ motion in proton beam therapy are discussed in the following.

2.1.1 Physical Principle

Protons with kinetic energies E of up to 250 MeV are typically used for radiotherapeutic applications. Their most important physical interactions with the electrons and nuclei of the human body and material in the beam path are outlined in this section, namely inelastic Coulomb interactions with electrons, elastic Coulomb scattering on nuclei, and inelastic nuclear interactions.

Interactions with Target Electrons

The primary mechanism of energy transfer from the proton beam to the target material are multiple inelastic Coulomb interactions between the proton and the electrons in the target. In these interactions, target electrons are excited and may leave the atomic shell, and the traversing proton loses a small amount of energy. This way, the particle deposits its energy to the medium almost continuously, leading to a deceleration until stopping at a certain depth referred to as the proton range. The ionisation can damage the affected molecules in the body, especially the DNA, which can lead to cell death or impeded cell division (Paganetti, 2011).

The mean energy loss of a proton $\mathrm{d}E$ per path length $\mathrm{d}x$ due to its inelastic collisions with electrons is called stopping power S. It can be approximated for therapeutic energies using the Bethe-Bloch formula (Bethe, 1930; Bloch, 1933; Ziegler, 1999; Gottschalk, 2011)

$$S = -\frac{\mathrm{d}E}{\mathrm{d}x} \approx K \cdot \rho \, \frac{Z}{A} \cdot \frac{z^2}{\beta^2} \cdot \left[\ln\left(\frac{2 m_e c^2 \beta^2}{I(1-\beta^2)}\right) - \beta^2 \right] \tag{2.1}$$

with the speed of light c, the electron mass m_e and the prefactor $K = 0.3072\,\mathrm{MeVcm^2\,g^{-1}}$. Thus, the energy loss depends not only on the projectile (charge $z = 1$ in multiples of the electron charge, and velocity $v = \beta c$), but also strongly on the target material (density ρ, charge number Z and mass number A of the nuclei, and mean excitation energy of the electrons I). The linear energy transfer (LET) describes the energy locally transferred to the medium per path length and is defined as the stopping power restricted to secondary electrons in the vicinity of the proton track.

The stopping power is proportional to the most prevalent physical quantity in radiation therapy, the dose. The dose D describes the mean energy $\mathrm{d}E_{\mathrm{beam}}$ transferred by the beam to matter per unit mass $\mathrm{d}m$

$$D = \frac{\mathrm{d}E_{\mathrm{beam}}}{\mathrm{d}m} = \frac{1}{\rho}\frac{\mathrm{d}E}{\mathrm{d}x}\frac{\mathrm{d}N}{\mathrm{d}A} = \frac{S \cdot \Phi}{\rho} \tag{2.2}$$

with the particle fluence $\Phi = \frac{\mathrm{d}N}{\mathrm{d}A}$, i.e. the number of protons $\mathrm{d}N$ crossing the area element $\mathrm{d}A$ (Gottschalk, 2011). This quantity is known to correlate with cell death and tumour control in a sigmoid form (Holthusen, 1936), and therefore commonly used to generate and evaluate treatment plans in radiotherapy. Its SI unit is the Gray ($1\,\mathrm{Gy} = 1\,\mathrm{J\,kg^{-1}} = 6.24 \cdot 10^{12}\,\mathrm{MeVkg^{-1}}$). About 10^{11} protons are needed to generate a dose of 1 Gy inside a volume of 1 liter. The proton treatment is typically applied in about 30 fractions of 2 Gy per day with a dose rate of about $1\,\mathrm{Gy\,min^{-1}}$, which latter translates into an effective proton current of about 0.3 nA.

From equation 2.1 it follows that the proton deposits an increasing amount of energy to the medium per path length while slowing down, since the electrons stay longer in the vicinity of the Coulomb field of the passing proton. The typical depth-dose distribution profile of a mono-energetic proton beam therefore shows a plateau region in the entrance region of the material and a sharp maximum at the end of its range, the so-called Bragg peak, shortly before the protons stop (see Fig. 2.1). This sharp dose maximum is used in proton radiotherapy to selectively destroy tissue identified as malignant on a CT or MRI scan while sparing healthy tissue behind the tumour volume.

The fluctuation of energy loss of a particle follows a Landau distribution (Landau, 1944; Vavilov, 1957). Events with a very low energy deposition as compared to the particle energy (in the order of 10 eV) are most probable (Pimblott and LaVerne, 2007). Thus, the energy is transferred to a quite small volume around the track of the primary proton, as compared to

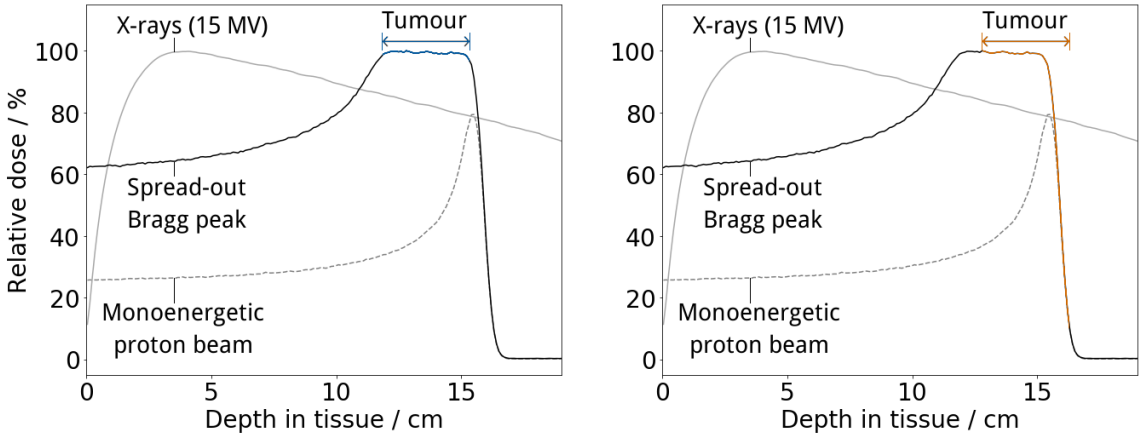

Figure 2.1: Relative dose as a function of depth in water for photons and protons. (a) Proton beams show a distinguished maximum (Bragg peak) at the end of their range, which can be spread out to cover a predefined tumour volume (blue), whereas photon beams deposit extra dose in front of and behind the tumour. (b) Tumour motion (in this example by 1 cm) can cause strong tumour underdosage (orange) and healthy tissue overdosage in proton therapy if not accounted for. Data courtesy of Jan Eulitz (OncoRay, Dresden, Germany).

therapeutic X-rays with a mean secondary electron energy in the order of 1 MeV (Jursinic and Mackie, 1996).

The mean range R of a proton with initial energy E can be calculated using the continuous slowing down approximation (CSDA)

$$R(E) = -\int_{E}^{0} \frac{1}{S(E')} \mathrm{d}E' \,. \tag{2.3}$$

In practice, range tables as a function of energy (Berger et al., 2005) or analytical approximations (Bortfeld, 1997) can be used for range estimation. To cover the whole tumour volume, usually several beams with different initial energies, and therefore different ranges inside tissue, are applied. By optimising their relative intensities (i.e. their weights) and adding up the resulting energy deposition, a so-called spread-out Bragg peak (SOBP, see Fig. 2.1) is created, covering the tumour extent in depth.

Interaction with Target Nuclei

In contrast to the target electrons, the target nuclei have a rest mass comparable to that of a proton. Due to multiple elastic Coulomb interactions with the target nuclei, the traversing protons therefore undergo lateral scattering in a medium (Molière, 1947; Molière, 1948;

Rutherford, 1911). Scattering leads to a setup-dependent broadening of the beam, whose central lateral shape can be approximated by a Gaussian (Gottschalk, 2011). The resulting full width at half maximum (FWHM) of the beam can range up to the order of 4 cm for 250 MeV at the end of range (Mertens et al., 2010). In contrast to the depth-dose distribution, the lateral dose distribution can be less sharp for protons than for therapeutic X-rays due to scattering (Suit et al., 2003).

In addition to the beam broadening, the different paths of the scattered protons lead to fluctuations in the range as projected on the initial beam direction. Combined with the statistical fluctuations in the number of interactions between the proton and the material and in the energy transferred per collision, this results in a broadening of the Bragg peak (range straggling) to about 1 % of the proton range (Gottschalk, 2011).

Furthermore, nuclear target fragmentation processes can occur in inelastic interactions of the proton beam with the target nuclei (Serber, 1947). Uncharged particles (neutrons and γ-rays), charged fragments (such as secondary protons and α-particles), as well as excited and radioactive nuclei can be produced in this and subsequent processes. Their dose contributions are orders of magnitude smaller than those of the primary particles and therefore negligible for most applications (Gottschalk, 2011). However, the radioactivation of material, especially metal, in the beam path can become relevant for radiation protection (Faßbender et al., 1997). Both radioactive decay and prompt de-excitation processes of the nuclear fragments are under research to be used for quality assurance, i.e. to verify the proton range in the patient (Maccabee et al., 1969; Stichelbaut and Jongen, 2003).

2.1.2 Beam Delivery

In order to accelerate and guide the proton beam to the patient, a number of electromagnetic fields are applied. This process is outlined in the following.

Acceleration and Energy Selection

Free protons are typically generated in a proton source from hydrogen gas by ionisation via free electrons (Penning, 1927) or microwaves (Brown, 2004). They are then accelerated to the necessary kinetic energy by either a cyclotron or a synchrotron (Schippers, 2009).

A cyclotron mainly consists of four electrodes arranged like wind mill vanes, and an electromagnet producing a 2 T to 4 T transversal magnetic field (Schippers, 2011). A radio-

frequency (RF) generator induces an oscillating voltage at the electrodes, which switches polarity with a frequency of 50 MHz to 100 MHz. While being guided on a spiral trajectory by the magnetic field, the protons are thus accelerated from one electrode to the next until being extracted at their final energy. The magnetic flux density increases from the centre of the magnet with increasing radius to account for relativistic effects. The time required for one turn in the cyclotron is as a result independent from the proton velocity, which allows for quasi-continuous beam extraction and fast intensity adjustments. A cyclotron has a typical diameter of 2 m to 5 m (Cheng et al., 2016; Schippers, 2009).

A synchrotron is a ring accelerator consisting of a series of magnets with a flux density of about 1.5 T and an RF acceleration cavity, which subsequently deflect and accelerate a proton bunch on a circular path (Schippers, 2011). An initial energy of 2 MeV to 7 MeV is required, which is achieved by a linear accelerator placed in an injection system which precedes the synchrotron. Protons are accelerated in bunches within about a second, and can be extracted in spills in the order of seconds. A proton synchrotron has a typical diameter of 5 m to 8 m, and the injection system has a typical length of 3 m to 10 m (Wang et al., 2012; Schippers, 2009).

While the final proton energy can be adjusted at a synchrotron, a cyclotron only delivers a fixed energy, which is suitable for deep-seated tumours. When lower energies are required, the proton beam is decelerated downstream the cyclotron using a degrader, such as a graphite wedge and a subsequent arrangement of dipole magnets to reduce the energy spread (Reist et al., 2001). As a result, the beam intensity decreases with decreasing energy (by up to 99.9 %), and the activation of the stopping material increases, which is a disadvantage of cyclotrons as compared to synchrotrons. On the other hand, a cyclotron is more compact than a synchrotron and allows for faster beam energy and intensity adjustment (Schippers, 2009).

Beam Guidance and Gantry

The patient is positioned in a neighbouring room which is shielded from ionising radiation emerging from activation of the material in and around the accelerator. The beam is guided to this treatment room by a beam line, i.e. vacuum pipes which are surrounded by quadrupole and dipole magnets designed to focus and direct the beam with a magnetic flux density of approximately 0.5 T and 2 T, respectively.

The beam can then be delivered immediately to the patient in a fixed horizontal beam line, or rotated around the patient by a beam line mounted onto an isocentric gantry, which allows irradiation of the patient from different directions without rotating the patient. A gantry is a rotatable, usually ferromagnetic construction with a typical diameter and radius of 10 m and 5 m, respectively, a weight of about 100 tons, and a rotation speed below 10° per second (Weinrich, 2006; Schippers, 2009). The distance between the patient and the closest magnet in the gantry, which is a dipole magnet, is usually about 2 m. Although many patients may be treated without a gantry (Yan et al., 2016), most proton therapy centres are equipped with at least one (Particle Therapy Co-Operative Group, 2018).

Field Formation

By optimizing the fluence and energy of the charged particles, the shape of the spread-out Bragg peak can be modulated according to the tumour volume (see Figure 2.1). This is realized in the treatment facilities in two different ways (Wiedemann, 2007; Schippers, 2009; Engelsman et al., 2013).

During the classically used passive beam delivery (Engelsman et al., 2009), a large beam field is created by means of one or more scatterers made up of lead and polycarbonate, and adjusted to the tumour cross-section by either individually designed solid brass or multi-leaf collimators. For the creation of the SOBP, rotating modulator wheels or ridge filters are placed in the beam line. An individually manufactured compensator is used to tailor the range of the beam to the distal end of the tumour.

An increasingly used alternative technique is active beam scanning (Kanai et al., 1980). Here, the target volume is divided into slices of equal beam range. For each of these slices, a beam of an energy corresponding to the specific range is created. It is then deflected laterally by two pairs of magnets of 1 T to 2 T in two dimensions. This way, the beam is scanned subsequently over each slice. Depending on the system design and the treatment field, the scanning time is usually in the order of tens to hundreds of milliseconds per line and hundreds of milliseconds to few seconds per slice, and changing the beam energy takes about one to two seconds (Seco et al., 2009; Flanz, 2011; Shen et al., 2017). Consequently, the magnetic field of the scanning magnets changes dynamically during beam delivery. Ionisation chambers and multi-wire proportional chambers (MWPCs) provide online feedback on the beam fluence and position, respectively. This setup does not require

patient-specific hardware and enables improved proximal normal tissue sparing as compared to the passive setup (Engelsman et al., 2013), but is also more sensitive to organ motion, as discussed in the following section.

2.1.3 Motion Management and the Role of Image Guidance

One of the key challenges of proton therapy is the treatment of moving organs (Engelsman et al., 2013; De Ruysscher et al., 2015; Mori et al., 2018; Landry and Hua, 2018). Respiration, cardiac motion, peristalsis, muscle relaxation, bowel, rectum and bladder filling, and spontaneous motion such as swallowing during irradiation can compromise targeting precision, especially of tumours in the thorax and abdomen, such as lung and liver tumours (Landry and Hua, 2018). The applied dose distribution is not only blurred or shifted by motion, but can be significantly distorted due to the steepness of the Bragg peak and the strong dependence of its position on the traversed material composition (De Ruysscher et al., 2015; Landry and Hua, 2018). Furthermore, when using the active scanning technique, the motion patterns of the pencil beam and the patient organs can interfere (interplay effect), which can cause tumour underdosage or healthy tissue overdosage (Seco et al., 2009). Current strategies to mitigate these effects are summarised in the following.

Treatment Planning

Methods to manage motion during the planning stage previous to the treatment include:

- **Motion minimisation.** Respiratory motion can be minimised for example by an abdominal corset (Heerkens et al., 2017) or by voluntary breath-hold (Boda-Heggemann et al., 2016). However, not all patients are eligible for this practice, and residual motion remains (Mori et al., 2018).
- **Margins.** Treatment margins can be added to the target volume delineation to cover the target in each stage of the respiratory cycle based on a retrospectively reconstructed four-dimensional CT or MRI scan (Engelsman and Kooy, 2005; Kang et al., 2007). While assuring tumour coverage in spite of regular respiration, this approach increases the dose to healthy tissue, does not account for aperiodic movements, patient variability and the interplay effect.

- **Robust planning.** The uncertainties introduced by setup and range uncertainties, breathing motion, and interplay effects can be incorporated into the treatment planning process to effectively render the treatment more robust (Inoue et al., 2016). More sophisticated but similar to the margin approach, this method leads to increased healthy tissue dosage (Engelsman et al., 2013).

Interfractional Treatment Adaption

Anatomical changes occurring between treatment fractions, such as weight loss or gain, tumour shrinkage, inflammatory swelling, and setup fluctuations may severely alter the dose distribution and can be accounted for by acquiring anatomical images immediately before treatment fractions and adapting the patient position or treatment plan if necessary (Cheung et al., 2013; Mori et al., 2018). Possible imaging modalities include:

- **Orthogonal X-ray.** The current standard in proton therapy is the acquisition of two orthogonal kV X-ray radiographs for pre-fraction position verification, with or without implanted fiducial markers (Bolsi et al., 2018). Its main disadvantage is the lack of soft-tissue contrast and of volumetric information on the material in the proton path.

- **In-room CT**. Cone-beam CT (Jaffray et al., 2002) and CT-on-rails (Ma and Paskalev, 2006) allow for volumetric in-room X-ray imaging. They are the standard of care in conventional X-ray therapy (Engelsman et al., 2013) and are becoming increasingly available for proton therapy (Veiga et al., 2016; Mori et al., 2018). While in-room CT scanners provide better image quality, flexibility and acquisition speed, only cone-beam CT scanners allow for imaging in treatment position at the beam isocentre. The effective ionising dose exposure to the patient ranges up to about 10 mSv and the individual organ dose up to 30 mGy per acquisition for frequent imaging (Marchant and Joshi, 2016). Organ visibility is very limited in these modalities due to a low soft-tissue contrast, such that position verification has to be performed based on surrogates such as the bony anatomy or surgically implanted fiducial markers (Noel et al., 2015; Chandarana et al., 2018).

- **Proton radiography.** Using the proton beam for imaging could allow for direct proton attenuation measurements, thus removing the uncertainty-prone step of converting X-ray-based images to stopping power (Schneider and Pedroni, 1995; Schulte et al.,

2004). This technique is still in a research state due to the need for high energy beams and due to limitations in image quality caused by scattering (Poludniowski et al., 2015).

Intrafractional Treatment Adaption

It has been shown that the proton beam irradiation needs to be adapted to intrafractional motion in real-time in cases involving a high dose per fraction, motion perpendicular to the beam direction, irregular motion, or motion amplitudes above 5 mm (Knopf et al., 2011; Jakobi et al., 2018; Mori et al., 2018). Such an adaption can be realised by gating the beam depending on the tumour position (Ohara et al., 1989; Mori et al., 2010), by tracking the tumour volume with the beam (Grozinger et al., 2006; Bert et al., 2007; Riboldi et al., 2012), by rescanning the tumour volume multiple times to smoothen out the interplay effect (Phillips et al., 1992; Zhang et al., 2015), or a combination thereof. For this, the position of the tumour, or ideally the three-dimensional patient geometry, has to be acquired in real-time, which can be realised by the following techniques:

- **External tracking.** Cameras monitoring the patient surface (Gilles et al., 2016), on-body infrared-visible markers (Dong et al., 2012), gauge sensors (Bengua et al., 2010), and spirometers (Hanley et al., 1999) can generate respiratory signals of the patient during irradiation (Mori et al., 2018). They are non-invasive and easily implemented but do not correlate reliably with the tumour and organ motion (Gierga et al., 2005; Korreman et al., 2008).
- **Ultrasound imaging.** The use of ultrasound for real-time image guidance has been proven feasible in principle for the diaphragm, liver, prostate and lung surface (O'Shea et al., 2016). This method is cost-effective and provides high contrast and resolution images without applying ionising irradiation, but volumetric imaging, speed of sound aberration artefacts, the placement of the transducer, and lung imaging remain problematic (Camps et al., 2018; Mori et al., 2018).
- **Fluoroscopy.** The process of monitoring the tumour position or the bony anatomy by continuous planar X-ray imaging, with or without fiducial markers, is called fluoroscopy (Shirato et al., 1999; Li et al., 2010). While being easy to implement, this technique suffers from a limited correlation of the markers with the tumour position, size and

shape (Shirato et al., 2006; Newhauser et al., 2007), a lack of volumetric information of the tissue traversed by the beam, and additional dose to the patient (Mori et al., 2018).

In conclusion, current image guidance possibilities have critical limitations such as the lack of volumetric imaging data of the beam path, insufficient soft-tissue contrast, poor correlation of markers and organ motion, and the use of ionising radiation. However, a detailed understanding of intra- and interfractional changes is essential for accurate treatment planning and delivery. While image guidance is less developed for proton than for X-ray based radiotherapy, the imaging requirements are more stringent for protons since the depth-dose distribution is steeper, less beam directions are used, and morphological changes in the beam path directly affect the proton range.

An integration with MRI could allow for high-contrast on-line imaging in treatment position without additional dose to the patient, but such integrated systems do not exist for proton therapy (Liney et al., 2018b). This possibility is therefore further discussed in the following sections.

2.2 Magnetic Resonance Imaging

Magnetic resonance imaging (MRI) appears to be an ideal candidate for inter- and intrafractional image guidance, as it offers excellent soft-tissue contrast, a high spatio-temporal resolution and absence of ionising radiation. The physical principle and application of MRI are therefore summarized in the following.

2.2.1 Physical Principle

MRI is predicated on the manipulation of magnetic moments in the patient body via three distinct types of electromagnetic fields: a homogeneous static magnetic field $\vec{B}_0$, a radio-frequency (RF) pulse $\vec{B}_1$, and magnetic gradient fields $\vec{G}_x, \vec{G}_y$ and $\vec{G}_z$. The basics of this process which are necessary to comprehend mutual effects of the proton therapy and the MRI system in an MRiPT setting are described in this section.

Energy separation in a static magnetic field

Hydrogen nuclei (i.e. protons) possess a nuclear spin $\vec{I}$ and a resulting magnetic dipole moment $\vec{\mu} = \gamma\vec{I}$, which are proportional via the gyromagnetic ratio $\gamma \approx 2.7 \cdot 10^8\,\mathrm{rad\,s^{-1}T^{-1}}$ (Estermann et al., 1933). When placed in an external magnetic field $\vec{B}_0 = B_0\vec{e}_z$, their components I_z and μ_z oriented parallel to $\vec{B}_0$ are quantised at two energy levels ($I_z = \pm\frac{1}{2}\hbar$ and $\mu_z = \pm\frac{1}{2}\gamma\hbar$ with the reduced Planck constant $\hbar \approx 6.6 \cdot 10^{-34}\,\mathrm{Js}$) with an energy separation of $\Delta E = \gamma\hbar B_0$.

This quantum-mechanical effect can be understood semi-classically as a torque $\vec{T_0} = \vec{\mu} \times \vec{B}_0$ exhibited on the proton magnetic moment $\vec{\mu}$, which forces it into a precession on a cone around $\vec{B}_0$, comparable to a spinning top in gravity. The precession frequency, also called Larmor frequency,

$$f_0 = \frac{\gamma}{2\pi} B_0 \approx 42.6\,\mathrm{MHz\,T^{-1}} \cdot B_0 \tag{2.4}$$

then follows from its equation of motion $\frac{\mathrm{d}\vec{I}}{\mathrm{d}t} = \vec{T_0}$. The two energy states correspond to a precession parallel and antiparallel to $\vec{e}_z$.

The ratio of occupation of these two states N_+ and N_- at body temperature $T \approx 36\,^\circ\mathrm{C}$ is given by the Boltzmann factor $\frac{N_-}{N_+} = e^{\frac{\Delta E}{k_\mathrm{B}T}} \approx 1 + 6 \cdot 10^{-6}\,\mathrm{T^{-1}}B_0$ with the Boltzmann

constant $k_\mathrm{B} \approx 1.4 \cdot 10^{-23}\,\mathrm{J\,K^{-1}}$. As an example, the total number of protons in a water-filled volume of $V = 1\,\mathrm{l}$ is $N = N_- + N_+ = \frac{2N_\mathrm{A}\rho V}{M} \approx 6.7 \cdot 10^{25}$ with Avogadro's constant $N_\mathrm{A} \approx 6.0 \cdot 10^{22}\,\mathrm{mol^{-1}}$ and the molar mass of water $M = 18\,\mathrm{g\,mol^{-1}}$. Thus, the number of excess protons in the lower energy state is $N_- - N_+ = N\frac{(N_-/N_+)-1}{(N_-/N_+)+1} \approx 2.0 \cdot 10^{20}$*. Due to these excess protons, the vector sum of the magnetic moments per unit volume, the magnetisation $\vec{M}_0 = M_0\vec{e}_z$, is non-zero and points along the direction of the magnetic field with $M_0 = \frac{N\gamma^2\hbar^2}{4k_\mathrm{B}T}B_0$ per litre (Gultekin and Gore, 2005).

The buildup of $\vec{M}_0$ in $\vec{B}_0$ is not instantaneous, but increases proportionally to the difference of the longitudinal magnetisation M_z to its equilibrium value M_0 with a time constant denoted as T_1 (Bloch, 1946):

$$\frac{\mathrm{d}M_z}{\mathrm{d}t} = -(M_z - M_0)/T_1\,. \tag{2.5}$$

T_1, also called spin-lattice or longitudinal relaxation time, depends on the material-specific probability of transitions between the two spin states.

Excitation by radio-frequency pulses

A short RF pulse with a time-varying magnetic component $\vec{B}_1(t)$, which rotates exactly with the Larmor frequency ω_0 around $\vec{B}_0$, can be used to manipulate the magnetisation built up by $\vec{B}_0$ (Bloch et al., 1946; Purcell et al., 1946). $\vec{B}_1(t)$ induces a torque $\vec{T}_1(t) = \vec{M} \times \vec{B}_1(t)$ on the magnetisation $\vec{M}$ and tips it towards the xy-plane perpendicular to $\vec{B}_0$ (Bloch, 1946). The component of $\vec{M}$ rotating in the plane perpendicular to $\vec{B}_0$, denoted as M_{xy}, then produces a periodic electromagnetic signal $S(t) \propto M_{xy}e^{-2\pi i f_0 t}$ that can be detected via induction in a suitable receiver coil.

Since the local Larmor frequency slightly fluctuates due to material-specific molecular rotations, translations and vibrations, groups of proton spins of different frequency, and thus the components of $\vec{M}$, start to dephase after the excitation. Furthermore, $\vec{M}$ relaxes back to its equilibrium orientation $\vec{M}_0$. As a result of both effects, M_{xy} decreases with a time constant T_2 (lateral or spin-spin relaxation time), with $T_2 < T_1$. The motion of $\vec{M}$ can then be described by (Bloch, 1946)

$$\frac{\mathrm{d}M_{xy}}{\mathrm{d}t} = -M_{xy}/T_2\,. \tag{2.6}$$

*i.e. nine orders of magnitude larger than the number of protons of a therapeutic proton beam in the same volume (see section 2.1.1)

This phenomenon is known as nuclear magnetic resonance (NMR), and equations 2.5 and 2.6 are the so-called Bloch equations (Bloch, 1946)†. Under the initial condition that the magnetisation is tipped by the flip angle α after the RF pulse, i.e. $M_z(t=0) = M_0 \cos\alpha$ and $M_{xy}(t=0) = M_0 \sin\alpha$, their solution is

$$M_z(t) = M_0\, e^{-t/T_1}\, \cos\alpha + M_0(1 - e^{-t/T_1}) \quad \text{and} \quad M_{xy}(t) = M_0\, e^{-t/T_2}\, \sin\alpha \tag{2.7}$$

Thus, M_{xy} decreases while M_z increases back to the equilibrium value M_0. Since both time constants T_1 and T_2 are highly material specific, they can be used for tissue discrimination with a high soft-tissue contrast. This way, T_1, T_2 and therefore $\vec{M}$ depend on the material at each position (x, y, z). The periodic signal of decreasing amplitude picked up by the receiver coil is called free induction decay (FID).

From a quantum-mechanical point of view, $\vec{B}_1(t)$ can be understood as photons of frequency $\omega_0 = 2\pi f_0$, whose energy is identical to the energy separation between the two states $\Delta E = \gamma\hbar B_0 = \hbar\omega_0$ and therefore allow for a spin state transition. The described effects occur analogously for all nuclei with an odd number of protons or neutrons, but hydrogen nuclei are most commonly used in MRI since their high abundance in the human body and their large gyromagnetic ratio lead to the largest NMR signal (Brix et al., 2008).

Spatial encoding by magnetic gradient fields

To create an MR image, the Larmor frequency is rendered position-dependent by introducing a linearly increasing magnetic gradient field $\vec{G}_x(x) = G_x \cdot x \cdot \vec{e}_z$ (Lauterbur, 1973). The superposition with $\vec{B}_0$ leads to a spatially dependent Larmor frequency (see equation 2.4)

$$f(x) = \frac{\gamma}{2\pi}(B_0 + G_x \cdot x) \quad \Leftrightarrow \quad x = \frac{2\pi f(x)}{\gamma G_x} - \frac{B_0}{G_x}\,. \tag{2.8}$$

This method is called frequency encoding. The bandwidth of the resulting signal is $\Delta f_{\mathrm{rec}} = \frac{\gamma}{2\pi} G_x L_x$ with L_x the size of the field-of-view (FOV) to be covered in x-direction.

The second dimension of the image, y, can be encoded in the spin precession by applying a second gradient $\vec{G}_y(y) = G_y \cdot y \cdot \vec{e}_z$ for a short period of time T_{PE} at time point t_{PE} after applying the excitation pulse (i.e. $\vec{G}_y(y,t) = G_y(t) \cdot y \cdot \vec{e}_z = G_y \cdot y \cdot \mathrm{rect}(\frac{t - t_{\mathrm{PE}}}{T_{\mathrm{PE}}}) \cdot \vec{e}_z$ with

† Both the Bethe-Bloch formula in proton therapy (equation 2.1) and the Bloch equations in MRI (equations 2.5 and 2.6) are named after the physicist Felix Bloch (1905-1983).

the rectangular function rect). During the application of $\vec{G}_y(y)$, the proton spins experience a y-position-dependent phase shift ϕ due to the temporary change in Larmor frequency $\Delta f(y)$:

$$\phi(y,t) = e^{2\pi i \Delta f(y) \cdot T_{\mathrm{PE}}} = e^{i\gamma G_y \cdot y \cdot T_{\mathrm{PE}}} = e^{i\gamma \int_0^t G_y(y,t')\mathrm{d}t'} \tag{2.9}$$

After the application of this gradient, the Larmor frequency is restored, but the relative phase differences remain dependent on y. This process is called phase encoding and was developed by Mansfield et al. (1976) and Edelstein et al. (1980).

Typically, the third dimension is encoded by a third gradient $\vec{G}_z(z) = G_z \cdot z \cdot \vec{e}_z$ which is only switched on during the RF pulse (Mansfield et al., 1976). By matching the RF frequency f_{RF} to the local frequency at a slice position z, i.e.

$$f_{\mathrm{RF}} = \frac{\gamma}{2\pi}(B_0 + G_z \cdot z)\,, \tag{2.10}$$

the slice z is selectively excited. The thickness of the slice d_z is determined by the gradient amplitude G_z and the spectral bandwidth Δf_{RF} of the RF pulse as $d_z = \frac{2\pi\Delta f_{\mathrm{RF}}}{\gamma G_z}$. The sum of the magnetisation in the z-direction of one slice $\bar{M}_{xy}(x,y) = \int_{\Delta f_{\mathrm{RF}}} M_{xy}(x,y,z)\mathrm{d}z$ determines the NMR signal of the excited slice. This method is often referred to as slice encoding.

The resulting FID signal S picked up by the receiver coil

$$\begin{aligned}
S(t) &\propto \iint_{\mathrm{FOV}} \bar{M}_{xy}(x,y,t) e^{-2\pi i f_0 t} e^{i\gamma \cdot x \int_0^t G_x(t')\mathrm{d}t'} e^{i\gamma \cdot y \int_0^t G_y(t')\mathrm{d}t'} \mathrm{d}x\mathrm{d}y \\
&= e^{-2\pi i f_0 t} \iint_{\mathrm{FOV}} \bar{M}_{xy}(x,y,t) e^{i\gamma \cdot (x \int_0^t G_x(t')\mathrm{d}t' + y \int_0^t G_y(t')\mathrm{d}t')} \mathrm{d}x\mathrm{d}y \\
&= e^{-2\pi i f_0 t} \iint_{\mathrm{FOV}} \bar{M}_{xy}(x,y,t) e^{i\gamma \cdot (x \cdot k_x + y \cdot k_y)} \mathrm{d}x\mathrm{d}y \\
&\propto e^{-2\pi i f_0 t} \cdot \mathcal{F}(\bar{M}_{xy}(x,y,t)) = \; e^{-2\pi i f_0 t} \cdot K(k_x, k_y, t)
\end{aligned}$$

can be converted back into the spatial distribution of the magnetisation $\bar{M}_{xy}(x,y,t)$ by an inverse two-dimensional Fourier transform $\mathcal{F}^{-1}$ (Mansfield et al., 1976). The function $K = \mathcal{F}(\bar{M}_{xy})$ depending on the variables $k_x = \int_0^t G_x(t')\mathrm{d}t'$ and $k_y = \int_0^t G_y(t')\mathrm{d}t'$ is called k-space. k-space is conventionally sampled by acquiring the time-resolved FID signal during the application of G_x and repeating this acquisition for different phase encoding gradient amplitudes G_y (see Figure 2.2). This sampling defines the image resolution, and the time

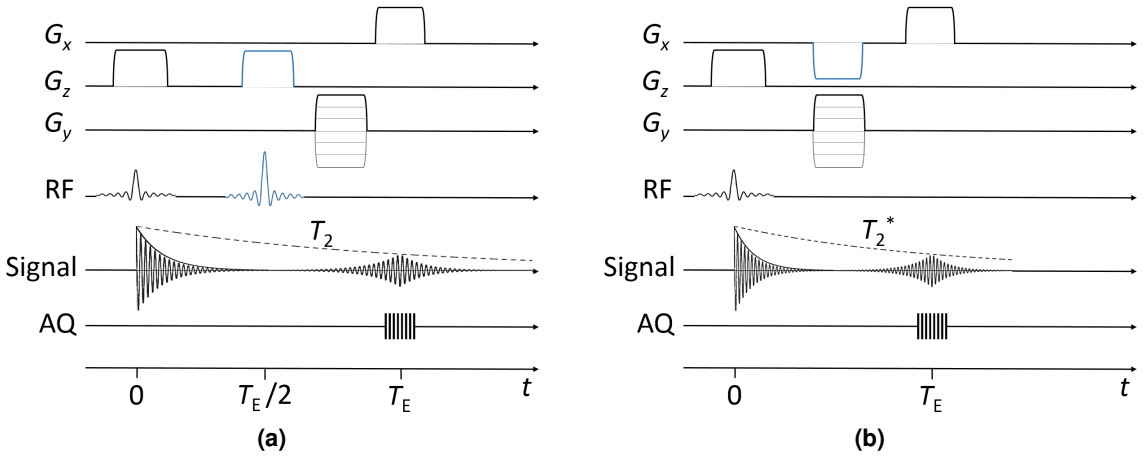

Figure 2.2: Simplified sequence diagram for a spin echo (a) and a gradient echo (b) sequence, i.e. the amplitude of the gradient fields $\vec{G}_x, \vec{G}_y$ and $\vec{G}_z$, the RF pulse, and the signal generated by the magnetisation, as a function of time. The image acquisition phase is denoted as "AQ".

between repeated acquisitions is called repetition time T_R.

Following equations 2.8 to 2.10, it can be concluded that external changes in $\vec{B}_0$ can induce image shifts in the frequency and slice encoding directions, whereas the phase encoding direction is unaffected. Typical clinical values for B_0 and $G_{x,y,z}$ are 0.2 T to 7 T and 1 mT/m to 80 mT/m, respectively (Brix et al., 2008; Ansorge and Graves, 2016).

2.2.2 Image Generation by Pulse Sequences

A commonly used alternative to measuring the FID signal immediately after the RF excitation is the creation of so-called echoes by pulse sequences. This way, a large variety of contrasts can be achieved (McRobbie et al., 2017). The sequences which are most relevant for this thesis are introduced in the following.

Spin echo (SE)

Due to machine- and patient-related inhomogeneities in B_0, spin dephasing and thus the decrease of the FID signal occur rapidly with a time constant T_2^* which is smaller than the idealised constant T_2 ($\frac{1}{T_2^*} = \frac{1}{T_2} + \frac{1}{T_2'}$ with the static inhomogeneity-induced dephasing time T_2'). To counterbalance this, the spin echo (SE) technique can be applied (Carr and Purcell, 1954; Hahn, 1980). Here, another RF pulse with $\alpha = 180°$ is applied at time τ after the first pulse, which inverts the dephased components of $\vec{M}$ (see Figure 2.2a). Since the frequency

differences remain, the components point again in the same direction (i.e. they rephase) at time $T_{\mathrm{E}} = 2\tau$, yielding a measurable signal maximum (a so-called echo), which does not depend on T_2^* but on T_2. Thus, M_{xy} can be measured at the so-called echo time $t = T_{\mathrm{E}}$ (cf. equation 2.7). In a dual echo (DE) sequence, the 180° RF pulse and acquisition are repeated before the next 90° excitation pulse, such that two images are acquired.

Gradient echo (GE)

The second commonly used sequence is called gradient echo (GE) (Edelstein et al., 1980; Markl and Leupold, 2012). Here, instead of a second RF pulse, an inverted frequency-encoding gradient $-G_x$ is applied, which dephases the components of $\vec{M}$. The gradient is then reverted to $+G_x$, which causes a spin rephasing at the echo time T_{E} (see Figure 2.2b). Here, only the dephasing caused by $-G_x$ is counterbalanced, and not that of T_2^*-related effects. Therefore, GE sequences are more sensitive to magnetic field inhomogeneities, but faster than SE sequences since the echo is formed immediately when applying $+G_x$ and since flip angles α below 90° can be used.

Inversion recovery (IR)

In an inversion recovery sequence, the magnetisation is inverted by applying an additional RF pulse with $\alpha = 180°$ before a regular SE or GE sequence (Doyle et al., 1981). This way, the magnetisation component induced by all spins with a common relaxation time T_1 is relaxed back to zero at the inversion time $T_{\mathrm{I}} \approx 0.7\, T_1$. Since the following RF pulse of the standard image sequence cannot tip this magnetisation component, no signal is detected from this group of spins (i.e. their signal is "nulled"). This method can be used either to increase the T_1-contrast or to selectively suppress the signal of specific tissue types, such as fat or fluids. It is one of the most commonly used sequences for musculoskeletal imaging.

Spoiling

For fast imaging, gradient echo sequences with a repetition time T_{R} which is considerably smaller than the lateral relaxation time T_2 are often used. Since $T_{\mathrm{R}} \ll T_2$, a remaining transverse magnetisation M_{xy} is transferred into the next repetition cycle, which can accumulate and adulterate the image. Possibilities to avoid this include applying a gradient with variable

amplitude at the end of each cycle, which causes a spin dephasing due to varied Larmor frequencies, or incrementally increasing the phase of the RF pulse. These techniques are called gradient-spoiling and RF-spoiling, respectively (Epstein et al., 1996).

Weighting

The above mentioned sequences can be used to generate different types of tissue contrast by varying the sequence parameters T_{R} and T_{E}. The longer the echo time T_{E}, the more pronounced are differences in the lateral magnetisation decrease described by T_2 (i.e. the more is the sequence T_2-weighted). On the other hand, the longer the repetition time T_{R} is chosen, the smaller are remaining differences in the T_1-related longitudinal recovery (i.e. the less is the sequence T_1-weighted). If both a short T_{E} and a long T_{R} are applied, the influence of differences in both relaxation mechanisms is minimised and the signal mainly depends on the number of excited protons (i.e. the sequence is proton density (PD)-weighted). Typical echo and repetition times are in the order of 50 ms and 1 s, respectively[‡].

Motion in MRI

Organ motion, especially due to respiration, is commonly handled by two different strategies depending on the imaging purpose. One strategy is to acquire four-dimensional image sets by acquiring a train of three-dimensional images over multiple breathing cycles and retrospectively correlating these to the respiratory phase as indicated by a surrogate signal such as the lung-liver interface (Stemkens et al., 2018). The resulting dataset can then be used for motion characterisation and radiation treatment planning.

If real-time MR images are required, such as is the case in tumour tracking in MR-integrated radiotherapy, commonly two-dimensional so-called cine MR images are acquired. The most often used sequence for this is the balanced steady-state free precession (bSSFP) gradient echo sequence (Bieri and Scheffler, 2013), which applies very short repetition times ($T_{\mathrm{R}} \leq 5$ ms) to make use of remaining transverse magnetisation from previous repetition cycles (as opposed to spoiling them). The two-dimensional cine MR images acquired of a single or three orthogonal slices can be registered to previously acquired four-dimensional image sets to generate quasi-four-dimensional image sets at a high speed (Paganelli et al., 2015).

[‡]which is comparable to the time constants of proton pencil beam scanning (see section 2.1.2).

Another common source of motion are flowing liquids. If a liquid, e.g. blood, flows out of the excited slice during image acquisition, it creates either a hyper- or a hypointense signal, depending on the pulse sequence. In a SE image, only those protons that experience both pulses create a signal. Material which flows out of the plane between both RF pulses therefore creates less signal. In a GE sequence, all spins excited by the initial RF pulse contribute to the signal. In each repetition cycle, a new volume of the fluid is excited, which is at that point fully relaxed and therefore produces a high signal. Furthermore, the movement of the protons along the gradient fields can lead to phase differences which cause a spatial misencoding in the phase encoding direction.

2.2.3 Image Quality

The image quality of MRI can be quantified for system characterisation and quality assurance by a number of standardised parameters (Price et al., 1990; American College of Radiology, 2017; National Electrical Manufacturers Association, 2014). These are summarised in the following.

Geometrical parameters

The accuracy of geometrical lengths and distances depicted on an MR image is described by a parameter called 'spatial linearity', 'distortion' or 'geometric accuracy' in different standard protocols. It is defined as the difference of lengths measured on the image to the actual lengths of an imaged object.

Another important parameter is the spatial resolution, which is used to quantify the minimum size of objects that can be detected in the image. It is mainly influenced by the pixel dimensions and can be measured by line pairs or grid structures in an imaging phantom.

The position and width of the excited slice depend on the accuracy of the peak frequency and bandwidth of the RF pulse, respectively. They can only be measured indirectly by ramps or wedges placed at a defined angle to the imaging slice in dedicated phantoms.

Signal parameters

The signal-to-noise ratio (SNR) describes the mean signal intensity relative to the surrounding noise in a homogeneous phantom. It is approximately proportional to $\frac{B_0}{\sqrt{\Delta f_{\mathrm{rec}}}}$ and

therefore considerably smaller for low-field scanners than for high-field scanners (Trattnig et al., 1997) due to the low number of excess protons in the lower energy state (see section 2.2.1). A low SNR is often counteracted by using large receiver bandwidths Δf_{rec} and correspondingly large frequency-encoding gradient amplitudes (cf. equation 2.8). Further strategies to improve the SNR include averaging over multiple image acquisitions (i.e. increasing the number of excitations and thus the acquisition time), increasing the voxel volume (i.e. degrading image resolution), and reducing the distance between receiver coil and imaged object. A similar parameter is the image uniformity, which describes the difference of the highest and lowest signal in a homogeneous phantom divided by their sum.

The signal-to-noise ratio is considered to be less important for MR-guided radiotherapy, specifically for tumour delineation, position verification and tracking, than for diagnostic imaging. On the other hand, the contrast-to-noise ratio (CNR), i.e. the difference between the mean signal of two tissue types divided by their standard deviation, is considered to be more relevant for this purpose, and this parameter is not directly correlated with B_0 (Wachowicz et al., 2016). Furthermore, the geometrical accuracy of MR images is rated more important for MR-guided radiotherapy than for diagnostic imaging. A geometrical accuracy of ≤ 2 mm has been recently suggested for real-time MRI-guided X-ray radiotherapy, which is rather challenging for conventional systems due to gradient nonlinearities which do not need to be compensated for in diagnostic imaging (Chandarana et al., 2018). However, standardised image quality parameters are only established for diagnostic imaging so far.

Artefacts

If the scanned object is larger than the FOV in the phase encoding direction, shifted images of the object (so-called image ghosts) can appear overlaid on the image due to spatial misencoding. Similar, but more blurred ghosting artefacts can also be caused by motion and by mechanical vibrations induced by the gradient coils. The ghosting ratio of an image is defined by the mean signal difference of two regions with and without ghosting (i.e. next to the object in the phase and frequency encoding direction, respectively), divided by the mean signal in a homogeneous image phantom.

Another common artefact is the chemical shift. Due to differences in the surrounding electron distribution, protons in large molecules, such as fat, experience a slightly different

magnetic field B_0 than protons in small molecules, such as water. The resulting difference in Larmor frequency of 3.5 ppm can lead to spatial misencoding in the frequency encoding direction. This effect is is proportional to B_0 and therefore less pronounced in low-field scanners. The same is true for susceptibility artefacts, which are signal voids caused by differences in the magnetisation of different tissues that cause a spin dephasing at tissue borders.

Magnets and scanners

MR scanners mainly differ in their construction type (i.e. open or closed-bore), the used magnet (i.e. permanent, resistive or superconducting), and the resulting value of the B_0 field (Overweg, 2006). Typically, open scanners comprise a permanent magnet producing a relatively low magnetic field ($\leq$ 0.4 T), whereas high-field scanners ($\geq$ 1.0 T) have a closed bore design based on superconducting electromagnets. In general, open low-field designs provide better access to the patient and objects in the field-of-view, a lower heat transfer to the patient (as expressed by the specific absorption rate, SAR), and lower costs as compared to closed-bore high-field scanners (Hayashi et al., 2004; Simonetti and Ahmed, 2017), but are more prone to temperature-dependent field drifts (Paciok and Blümich, 2015). The image quality for MR-guided radiotherapy purposes is not clearly superior for either low- or high-field scanners (see above). The question whether high or low-field scanners are preferable for MR-guided radiotherapy is therefore to date not answered (Wachowicz et al., 2016).

2.3 MR-Guided Radiotherapy

The aim of radiotherapy to increase tumour control while reducing side effects on healthy tissue is being pursued by applying dose distributions with increasingly steep gradients between the tumour and healthy organs at risk. As a consequence, these dose distributions are increasingly sensitive to delineation uncertainties as well as organ motion and deformation during treatment, which has given rise to the increasingly important role of image guidance (Mackie et al., 2003). Generally, image guidance in proton therapy lags behind that of X-ray radiotherapy due to the historically delayed commercial development and the system complexity (Engelsman et al., 2013; Bolsi et al., 2018). This is especially the case for MRI-guidance, which is considered one of the most promising tools for image guidance due to its high and versatile soft-tissue contrast, the high achievable imaging speed, and the absence of ionising radiation (Mori et al., 2018; Liney et al., 2018b; Paganelli et al., 2018; Landry and Hua, 2018; Chandarana et al., 2018). The current status of MR image guidance in X-ray based radiotherapy is outlined in this section as a basis to discuss the possibility of MR-integrated proton therapy in section 2.4.

2.3.1 Offline MR Guidance

MR guidance is currently used in clinical routine mainly before and after the radiation treatment course. Here, the high and versatile soft-tissue contrast, which allows for both structural and functional imaging, is utilised to increase the accuracy of CT-based target volume identification an delineation for many tumour sites (Lagendijk et al., 2014a; Schmidt and Payne, 2015; Paganelli et al., 2018). After completion of the radiation treatment, the treatment response can furthermore be monitored by use of MRI (Chandarana et al., 2018).

For research purposes, the absence of ionising radiation enables repeated and longer image acquisitions, which allow for example to quantify the variation of tumour motion over different breathing cycles (Menten et al., 2017; Thomas et al., 2018), the uncertainties induced by motion surrogates (Liu et al., 2004; Feng et al., 2009), or the probability density functions of the tumour position for robust planning (Cai et al., 2006). Furthermore, the use of MRI for treatment adaption based either on the tumour size or on physiological factors such as hypoxia, neural activity, and permeability is being investigated (Liney et al., 2018b).

2.3.2 On-line MR Guidance

Apart from these offline applications, on-line image guidance during irradiation has gained increasing research interest in the last decade (Paganelli et al., 2018). Targeting accuracy is expected to be significantly improved by synchronising the beam delivery to the patient anatomy, which changes during irradiation due to respiration, digestion, muscle relaxation and cardiac motion. For this purpose, MR-integrated X-ray therapy (MRiXT) devices are necessary.

Electromagnetic interference

The main challenges for the design of such systems are mutual electromagnetic interactions between the MR and the radiotherapy system.

The typical magnetic field tolerance of a linear accelerator and the magnetic encoders driving the leafs of multi-leaf collimators is 0.1 mT and 45 mT, respectively (Liney et al., 2018b). Furthermore, electrons in the linear accelerator are deflected if the magnetic fringe field of the MR scanner is too high, such that beam loss occurs between 1 and 60 mT (Liney et al., 2018b). Therefore, passive or active magnetic shielding systems are required to shield the linac from the magnetic field of the MR scanner. Moreover, the secondary electrons generated in the patient are affected by the magnetic field of the MR scanner. In an inline system, i.e. with a parallel beam and main magnetic field direction, they are focussed by the field leading to increased skin dose if they are not shielded (Bielajew, 1993; Oborn et al., 2010). In a perpendicular setting, the secondary electrons are deflected in the magnetic field, which leads to a widened beam penumbra and asymmetric dose distributions, and they may return to the patient (electron return effect), leading to an increased exit dose (Raaijmakers et al., 2005). This effect can be partly mitigated by applying opposing fields or by incorporating the magnetic field in the treatment planning system (Liney et al., 2018b).

Vice versa, the X-ray system also affects the MRI scanner. Electromagnetic shielding must be applied to avoid MR image artefacts induced by the linear accelerator (Liney et al., 2018b). While the static influence of the linear accelerator on the homogeneity of the magnetic field of the MR scanner can be compensated for by passive shimming, dynamic alterations such as a change of the gantry angle or of the distance between the X-ray source and the magnet can only be compensated for by active shimming using dedicated shimming coils (Liney et al., 2016). Furthermore, the interaction of the beam with the MR

Table 2.1: Existing MR-integrated X-ray therapy (MRiXT) systems. The systems mainly differ in the magnetic flux density of the main field of the MR scanner B_0 and the orientation of the magnetic field relative to beam direction.

Name	B_0 / T	Field orientation	Current status	Reference
ViewRay MRidian	0.35	perpendicular	clinical since 2014	Mutic and Dempsey (2014)
Elekta Unity	1.5	perpendicular	clinical since 2017	Raaymakers et al. (2017)
AuroraRT	0.5	inline	working prototype	Fallone (2014)
Australian MR-Linac	1.0	inline	working prototype	Keall et al. (2014)

receiver coil can lead to beam attenuation, increased skin dose, and image artefacts (Liney et al., 2016; Burke et al., 2012) such that dedicated radiotranslucent or radiotransparent receiver coils are required (Hoogcarspel et al., 2018; Liney et al., 2018a).

System design

Four MRiXT systems have been realised so far (see Table 2.1). Two of these are commercially available, namely the ViewRay MRidian (Mutic and Dempsey, 2014) and the Elekta Unity (Raaymakers et al., 2017), and two are in a working prototype phase, namely the AuroraRT (Fallone, 2014) and the Australian MR-Linac (Keall et al., 2014).

The magnetic flux density of the MR scanner in these systems ranges from 0.35 T (MRidian) to 1.5 T (Elekta Unity). MR scanners with a lower magnetic flux density have the advantage of interfering less with the radiotherapy unit, a lower SAR, and lower costs, but the potential disadvantage of a lower signal-to-noise ratio (see section 2.2.3). The systems furthermore differ in the orientation of the main magnetic field of the MR scanner relative to the beam direction, which can be either parallel (AuroraRT, Australian MR-Linac) or perpendicular (ViewRay MRidian, Elekta Unity). While a gantry can rotate the linac around the patient independently of the MR scanner in perpendicular systems, either the MR scanner (AuroraRT) or the patient (Australian MR-Linac) need to be rotated to irradiate treatment fields with different beam directions in the inline systems (Whelan et al., 2016). For all systems, the treatment couch is either fixed or movable by only small amounts (Paganelli et al., 2018), such that patient shifts for interfractional adaption need to be replaced by shifting the treatment field via adjusting the multi-leaf collimator (Ruschin et al., 2017) or by replanning

(Raaymakers et al., 2017). None of these four systems has been shown to be superior so far regarding beam delivery, image quality or targeting accuracy.

Clinical workflow

In clinical practice, a treatment plan is generated based on CT images before treatment. Before each irradiation fraction, the acquisition of high-quality volumetric MR images in treatment position and subsequent deformable image registration to the planning CT allows for position verification and, if necessary, treatment plan adaption to the anatomy of the day (Bohoudi et al., 2017; Henke et al., 2018). Replanning is performed by means of Monte Carlo based dose calculation, which currently takes between 5 minutes (Raaymakers et al., 2017) and 12 minutes (Bohoudi et al., 2017).

During irradiation, the patient breathes with intermittent breath-hold and two-dimensional cine MR images are acquired with a frequency of about 5 frames per second (Henke et al., 2018). Several methods exist to convert these images into a motion signal to be used for gated beam delivery, including template matching, neural networks, and image registration (Paganelli et al., 2018). Since MR image acquisition and reconstruction can lead to a considerable time delay, motion prediction models are applied (Seregni et al., 2016).

In the near future, motion models are expected to be useful to extract out-of-plane motion from the cine images (McClelland et al., 2017; Paganelli et al., 2018). Furthermore, beamlets which were delivered suboptimally due to motion could be corrected for on-line by adapting upcoming beamlets of the irradiation plan (Kontaxis et al., 2015). However, the conversion of MR images to electron density, as required for X-ray dose calculation, is currently not performable in real-time but only retrospectively (Bohoudi et al., 2017; Stemkens et al., 2017).

First clinical findings have shown that organ motion description can be substantially improved by MR-based motion tracking relative to external surrogates (Stemkens et al., 2015) and that the overall survival of inoperable pancreatic cancer patients can be improved by dose escalation and daily treatment adaption via MR-guidance (Rudra et al., 2017). More extensive, prospective studies on the treatment outcome of MRiXT are currently being conducted (Henke et al., 2018).

2.4 MR-Integrated Proton Therapy

Because of the high sensitivity of proton therapy to anatomical variations (see section 2.1), the integration of MRI into proton therapy (MRiPT) is expected to be even more beneficial than for X-ray radiotherapy and thus has gained interest in the last years (Oborn et al., 2017; Landry and Hua, 2018; Lomax, 2018). The overall workflow is expected to be transferable from MR-integrated photon therapy (Oborn et al., 2017). However, since a number of technical and physical challenges need to be overcome, MRiPT has only been studied on a conceptual level thus far. To investigate the technological feasibility and exploit the potential of MRiPT, mutual interactions between both systems have to be taken into account. These include:

1. **Beam deflection.** If components of the magnetic field of the MR scanner are directed perpendicularly to the direction of the incident beam, Lorentz force-induced deflection of the proton beam occurs. Magnetic field components directed parallel to the direction of the incident beam rotate the radiation field around the central beam axis (Oborn et al., 2015).

   This affects both the beam transport to the treatment volume and the dose deposition inside the patient. For the deflection inside the patient, the simultaneous anatomy-dependent energy loss and energy-dependent deflection of the beam and its consequences on the Bragg peak position and the dose distribution have been approximated analytically (Wolf and Bortfeld, 2012; Hartman et al., 2015) and calculated by Monte Carlo simulations (Raaymakers et al., 2008; Moteabbed et al., 2014; Hartman et al., 2015). However, neither the structural differences of these studies nor their degree of accordance have been analysed in a systematic way. Furthermore, a ground truth of experimental benchmark data is lacking, hindering the verification and comparison of these simulation studies.

   Outside of the patient, energy loss can be mostly neglected for beam deflection, whereas the setup-specific magnetic fringe field has to be taken into account (Oborn et al., 2015). It has been suggested to generate machine- and field-specific look-up-tables for the deflection in air and use the resulting phase space as a starting point for patient-specific dose deflection inside the patient (Oborn et al., 2017). The deflection both inside and outside of the patient produces dose distortions that need to be

quantified and either compensated for or directly implemented in treatment planning systems, and both calculation parts need dedicated procedures for commissioning and quality assurance.

2. **System design.** For an acceptable magnetic field strength and homogeneity in the FOV of the MR scanner, the MR magnets need to closely surround the patient. At the same time, the proton beam needs to be transported to the patient, preferably from different directions, without interacting with the MR scanner. This leads to geometrical restrictions and challenges in the construction of MRiPT systems, and a number of layouts have been suggested (Overweg, 2009; P Forthmann, 2016; Oborn et al., 2017). No integrated systems have been realised so far.

   To facilitate unattenuated beam transmission to the patient, a split-bore or open MR scanner construction appears necessary. Isocentric irradiation with different beam directions can be facilitated either by mounting the beam line magnets on a rotating gantry or by installing a rotating patient couch (Oborn et al., 2017). The main problems of a rotating couch are the setup reproducibilty and gravity-induced organ deformations hampering an accurate registration to the planning CT (Whelan et al., 2016). For a gantry construction, the weight of the MR scanner, which is in the order of tens of tons, needs to be accounted for. An alternative is to use a setup with a fixed beam direction, which has been shown to be sufficient for a large number of patients treated with proton therapy (Yan et al., 2016). Either way, the use of lasers, markers or phantoms needs to be studied to determine the position of the isocentre of the MR scanner relative to the isocentre of the proton beam.

   Furthermore, since external RF signals can interfere with the MR imaging process and lead to image artefacts, the MR scanner must be surrounded by a Faraday cage, typically made of a thin copper foil. The proton beam needs to enter into the cage either through this foil, leading to increased beam stopping and scattering, or through a dedicated hollow tube used as waveguide port (Oborn et al., 2017).

3. **Magnetic field effects on MR image quality.** The magnetic fields of the proton facility may interfere with MR image acquisition and compromise the MR image quality. While the magnetic field of the cyclotron is expected to be manageable by proper shimming and by installing the MR scanner at an adequate distance (Hofman et al.,

2013; Cheng et al., 2016), the influence of the beam line and scanning magnets closest to the MR scanner is expected to be relevant, since their magnetic fields change dynamically and can have large components parallel to B_0 (Oborn et al., 2016). Experimental data on the influence of the beam line magnets, the beam scanning magnets, and gantry rotation is lacking so far, but necessary to determine whether magnetic shielding is required in addition to RF shielding.

4. **Beam effects on MR imaging.** The proton beam itself may alter the MR signal, for example by current-induced magnetic fields, local heating, formation of radicals or by interaction with the electronics of the MR receiver coil. This can be regarded both as a risk for MR image quality and as a potential opportunity to verify the proton range using the MR scanner. A number of patent applications exist on this issue (Kuhn and Overweg, 2009; Field and Bryning, 2013; Hoffmann and Speck, 2016; Prieels et al., 2017a; Prieels et al., 2017b), but quantitative simulation studies as well as experimental evidence are lacking.

5. **Dosimetry.** The response of dosimetry equipment used to characterise the beam during commissioning and quality assurance is expected to be distorted by the magnetic field of the MR scanner, as is the case in MR-integrated X-ray therapy (MRiXT) (Reynolds et al., 2014; Spindeldreier et al., 2017). Generally, signal distorting effects such as the electron return effect are expected to be smaller for MRiPT than for MRiXT due to the reduced range of secondary electrons (Raaymakers et al., 2008; Lühr et al., 2018). However, studies on the suitability of dosimeters and phantoms for proton dose measurements in the presence of magnetic fields and on necessary correction factors are lacking so far, except for one study on radiochromic films in a 1 T magnetic field, which mainly focussed on the electron return effect (Lühr et al., 2018). Furthermore, there is no data in literature on the effect of the magnetic field of the MR scanner on the multiwire ionisation chamber arrays in the proton beam nozzle, which are used for beam monitoring (Oborn et al., 2017). Since beam deflection and magnetic field effects on dosimetry equipment are expected to affect the procedures for beam commissioning and quality assurance, these procedures need to be adjusted and redefined.

6. **Adaptive planning on MR images.** For adaptive treatment planning on MR images

acquired in treatment position at the beginning of each treatment fraction, the stopping power and dose distribution need to be calculated from MR images.

The conversion of MR images to stopping power distributions can be achieved by a deformable image registration of the planning CT on the daily MR image (Dolde et al., 2018). While this gives the possibility to make use of the various MR contrast possibilities, the image registration process introduces uncertainties, especially if the changes between the patient anatomy during acquisition of the planning CT and the daily MR are large (Brock et al., 2017). Another possibility is the direct translation of MR image information into electronic stopping power, for which purpose a number of algorithms are being developed and tested (Rank et al., 2013b; Rank et al., 2013a; Edmund et al., 2013; Maspero et al., 2017; Koivula et al., 2016; Uh et al., 2018). Here, clinically acceptable levels of dosimetric accuracy have been achieved in homogeneous tissue, but considerable uncertainties remain in heterogeneous regions of bone and air (Koivula et al., 2016). Experimental evidence for a dosimetric comparison of both methods is lacking so far.

After conversion of the MR image to a stopping power distribution, a fast dose calculation algorithm is required (Giantsoudi et al., 2015; Tseung et al., 2015; Marmitt et al., 2018), which needs to be adapted to take into account beam deflection (see above). An alternative first approach would be to avoid the dose calculation by only extracting a motion signal from the real-time MR images, as is current practice in many MRiXT facilities (Stemkens et al., 2015).

7. **Gating and motion interplay.** To synchronise the proton irradiation to the moving patient anatomy acquired on the real-time MR images via gating or tracking, a close integration of the MR system and the beam control system is required including the conversion of MR images to a gating or tracking signal (Yun et al., 2016). As for all motion-adaptive treatments, the interplay between pencil beam scanning treatment and tumour motion may become an issue, and various strategies exist to mitigate this effect (Dowdell et al., 2013; Grassberger et al., 2015; Zhang et al., 2014). The use of the acquired real-time MR images has been suggested to further improve these mitigation strategies (Oborn et al., 2016). In general, tracking is more complex for proton than for photon therapy, since the proton range has to be adapted in addition to the beam position, which requires an adaption of the energy layers.

8. **Radiation damage.** Radiation-induced demagnetisation by direct irradiation with ion beams and secondary neutron fluxes is a known phenomenon for permanent magnets, which is thought to be due to thermal effects and alterations in the microstructure of the magnet materials (Ito et al., 2001; Blackmore, 1985; Danly et al., 2014; Samin et al., 2015). Furthermore, radiation damage to components of electronic equipment present in the treatment room is of concern when neutrons are produced by high-energy radiation beams. This has been shown for in-room CT scanners (Kry et al., 2011) and is expected to be an issue for in-room MR scanners as well. Studies that quantify these effects for an MRiPT setup are lacking so far, and procedures for quality assurance of the magnetic field and electronic performance of the MR scanner need to be developed.

In addition to these physical and technical challenges, the benefit and area of application of MR-integrated proton therapy need to be determined clinically. For this, the definition of imaging requirements (geometric accuracy, contrast, spatial and temporal resolution) and treatment sites, and extensive planning studies as well as clinical studies will be necessary. While the clinical translation will most likely start with static and hardly moving tumours (e.g. brain, extremities, head and neck), it is expected that the more challenging moving organs (e.g. lung, liver, pancreas, esophagus) will benefit most from MRiPT.

2.4.1 Aims of this Thesis

To summarise the current status of MR-integrated proton therapy, its development has only just begun. The work described in this thesis focusses on the first four challenges, namely (1) proton beam deflection, (2) MRiPT system design, (3) MR image quality, and (4) proton beam effects on the MR images. More specifically, the following research objectives are addressed:

1. **Beam deflection** (chapter 3). Previously published analytical and Monte Carlo calculations to predict the magnetic field induced displacement of the Bragg peak are compared to assess the current level of consensus. On this basis, it is hypothesised that a method can be developed that overcomes shortcomings of these methods with respect to accuracy, speed, and applicability to inhomogeneous magnetic fields and target geometries. Such a method is developed, and the prediction of Bragg peak

displacement by existing analytical methods and the newly developed method are compared against Monte Carlo based results to rate their accuracy.

In a second step, the hypothesis that Monte Carlo simulations can accurately predict experimentally measured beam deflection is tested. For this purpose, radiochromic film measurements are acquired on the proton beam and Bragg peak deflection in a tissue-mimicking slab phantom in a 1 T magnet and compared against Monte Carlo simulations in order to verify their applicability as a gold standard for dose calculation in magnetic fields.

2. **System design** (chapter 4.1). It is hypothesised that a low-field MR scanner can be combined with a static proton beam line, and that simultaneous proton beam irradiation and MR imaging of a phantom is feasible without visible distortions of the MR image and beam profile. To test this, a C-shaped 0.22 T MR scanner is placed at a fixed horizontal research proton beam line while accounting for RF interference and beam deflection during system design. The feasibility of simultaneous irradiation and imaging is evaluated qualitatively on anatomical MR images and lateral beam profiles.

3. **Magnetic field effects on MR image quality** (chapter 4.2). In the next step, the dynamic magnetic influences of the proton therapy facility on the MR scanner are evaluated. The hypothesis that motion of a gantry in the neighbouring treatment room does not relevantly affect the MR imaging process is tested by magnetic field camera measurements in the FOV of the MR scanner. Furthermore, the hypothesis is tested that the magnetic field of the proton beam line magnets do show a significant but manageable effect on the MR image quality. This is accomplished by measuring standardised image quality parameters both with and without simultaneous irradiation and statistically testing the resulting parameter distributions for equivalence.

4. **Beam effects on MR imaging** (chapter 4.3). The last hypothesis of this thesis is that proton beam irradiation of a water phantom induces a visible effect in MR images, from which the proton beam range can be deduced. To test this, MR images for six different sequences are acquired during high-current proton beam irradiation. An effect is observed, and its dependence on the proton current and energy and on the target material are assessed in order to determine its possible cause and area of application.

The main findings are then discussed in the general context of MR-integrated proton therapy in chapter 5, and the work is summarised in chapter 6. The contents of sections 3.1, 3.2 and 4.1 have been published by Schellhammer and Hoffmann (2017), Schellhammer et al. (2018b), and Schellhammer et al. (2018a), respectively.

3 Magnetic Field-Induced Beam Deflection and Bragg Peak Displacement

Being charged particles, the therapeutic protons will be deflected in an MRiPT setup if a component of their velocity is transversal to the magnetic field of the MR scanner. As this deflection is energy-dependent, the quasi-continuous energy loss of protons interacting with the human body will affect the local curvature of the beam as it penetrates the body. A number of theoretical studies have been performed using Monte Carlo simulations (Raaymakers et al., 2008; Moteabbed et al., 2014; Li, 2015; Hartman et al., 2015) and analytical models (Wolf and Bortfeld, 2012; Hartman et al., 2015) to investigate deflected beam trajectories of mono-energetic beams in a water phantom placed in a uniform magnetic field. Four studies have extended this work to Monte Carlo simulations in a patient geometry (Hartman et al., 2015; Moteabbed et al., 2014; Kurz et al., 2017; Burigo, 2018), and one has included the three-dimensional magnetic fringe field of the MR scanner (Oborn et al., 2015).

As pointed out by Oborn et al. (2015), the general consensus from these works is that the proton beam deflection within a patient or water phantom is relevant but predictable and therefore in principle correctable during treatment planning stages. However, different approaches have been introduced to assess this effect, and neither their structural differences nor their degree of accordance have been analysed in a systematic way. Differences can be expected, since all approaches are subject to their respective shortcomings. For instance, previously published analytical models imply critical assumptions, and are only applicable to the simplified case of a uniform (i.e. unrealistic) magnetic field. Monte Carlo simulations are potentially more accurate, but very time-consuming, which inhibits their use for routine treatment plan optimisation and real-time treatment plan adaptation. Thus, a method is required to quantify and correct for the deflection, which is accurate, applicable to inhomogeneous targets and magnetic fields, and fast. Furthermore, experimental benchmark data for a verification of these simulation studies is lacking.

The aim of this chapter is, therefore, three-fold. Firstly, studies published so far on the beam deflection are analysed and compared, and the limitations of the different methods are discussed (section 3.1.1). On this basis, a new model is developed to estimate the trajectory of a mono-energetic proton beam traversing a slab phantom inside a uniform transverse magnetic field, and its performance is evaluated against results of the previous models and Monte Carlo simulations (sections 3.1.2 to 3.1.4). Thirdly, the Monte Carlo-based prediction of beam deflection is verified experimentally by radiochromic film measurements for 80 to 180 MeV protons in a magnetic field of 1 T (section 3.2). The contents of this chapter have been published in similar form by Schellhammer and Hoffmann (2017) and Schellhammer et al. (2018b).

3.1 Analytical Description

To help understand the limitations of previously published analytical models, a condensed review and analysis thereof is given in section 3.1.1. On this basis, a new model to estimate and compensate for the magnetic field induced proton beam deflection is presented in section 3.1.2. The subsequent evaluation and comparison of this model in relation to existing approaches is presented in section 3.1.3. In section 3.1.4, the main findings and most important implications are discussed, and a short conclusion and outlook to further investigations are provided.

3.1.1 Review of Analytical Models

Previously published analytical models are shortly reviewed in this section. Being first order approaches, the methods model a monoenergetic proton beam traversing a water/air phantom inside a uniform transverse magnetic field.

General considerations

Let us consider a uniform magnetic field in vacuum of flux density $\vec{B} = B_0 \cdot \vec{e}_z$ which is aligned parallel to the z-axis and translation invariant. Let a monoenergetic proton pencil beam of kinetic energy E_0 with an initial velocity $\vec{v}_0 = v_0 \cdot \vec{e}_x$ perpendicular to $\vec{B}$ traverse the field (see Figure 3.1a). The entrance velocity $v_0 = c \cdot \sqrt{\frac{E_0\left(E_0+2m_0c^2\right)}{(E_0+m_0c^2)^2}}$ is connected to E_0

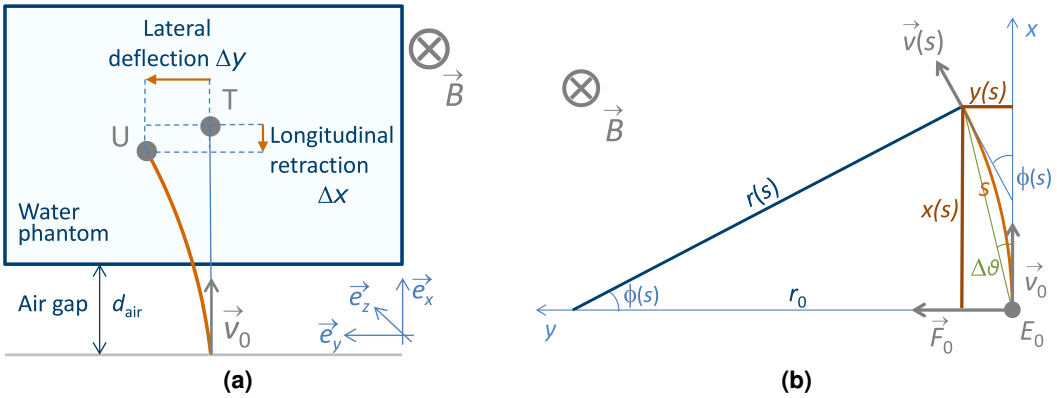

Figure 3.1: Setup geometry with omnipresent uniform transverse magnetic field $\vec{B}$. Starting from the beam nozzle, the proton beam (orange) traverses an air gap of length d_{air} before entering a water phantom. It is deflected by the magnetic field resulting in a deflection and retraction from its intended Bragg peak position T to the position U (a). The geometrical representation of the beam trajectory (b) is discussed in the text. Figure adapted from Schellhammer and Hoffmann (2017).

through the proton rest mass m_0 and the speed of light c. Carrying the elementary electric charge $q = 1e$, the equation of motion of the proton is governed by the Lorentz force

$$\vec{F} = \frac{\mathrm{d}\vec{p}}{\mathrm{d}t} = \gamma m_0 \frac{\mathrm{d}\vec{v}}{\mathrm{d}t} + m_0 \vec{v} \frac{\mathrm{d}\gamma}{\mathrm{d}t} = q(\vec{v} \times \vec{B}) \tag{3.1}$$

with the relativistic momentum $\vec{p} = \gamma m_0 \vec{v}$ and the Lorentz factor $\gamma = \frac{1}{\sqrt{1-(\frac{v_0}{c})^2}}$. As v_0 is constant, which yields $\frac{\mathrm{d}\gamma}{\mathrm{d}t} = 0$, this differential equation has a simple analytical solution

$$v_x = v_0 \cos(\frac{qB_0}{\gamma m_0} t),\ v_y = -v_0 \sin(\frac{qB_0}{\gamma m_0} t),\ v_z = 0 \tag{3.2}$$

for the velocity components v_x, v_y and v_z in x-, y- and z-direction, respectively. The protons thus move in a circular course with an angular frequency $\omega_0 = \frac{qB_0}{\gamma m_0}$. The radius of this course, the gyroradius, is given by

$$r = \frac{v_0}{\omega_0} = \frac{\gamma m_0 v_0}{qB_0}\,. \tag{3.3}$$

Now let us consider a setup geometry with a water phantom placed inside a virtual gantry-based MRiPT system. The distance between the proton beam nozzle and the surface of the water phantom is denoted by d_{air}. As opposed to the vacuum situation, protons deposit energy when traversing media until stopping at a finite range R_0. The range in water

can be approximated by a power-law range-energy relationship (Bortfeld, 1997)

$$R_0 = \alpha E_0^p \tag{3.4}$$

with $p \approx 1.75$ and $\alpha \approx 2.43 \cdot 10^{-3}\,\mathrm{MeV}^{-p}\mathrm{cm}$ (Wolf and Bortfeld, 2012). The protons slow down quasi continuously (ICRU, 1993) and hence the gyroradius decreases with increasing depth according to equation 3.3, which leads to a curled-up beam trajectory. Consequently, the Bragg peak experiences both a lateral deflection Δy from the entrance direction of the beam $\vec{e}_x$ and a longitudinal retraction Δx from its expected depth (see Figure 3.1a).

Analytical integration model

Wolf and Bortfeld (2012) have assessed the Bragg peak deflection and retraction by analytical integration (AI) of geometrical deflection steps. In accordance with Figure 3.1b and equation 3.3, they have described the deflection angle ϕ between the particle motion and the x-axis by

$$\frac{\mathrm{d}\phi}{\mathrm{d}s} = \frac{1}{r(s)} = \frac{qB_0}{\gamma(s) m_0 v(s)} \tag{3.5}$$

with the gyroradius $r(s)$, the velocity $v(s)$ and the Lorentz factor $\gamma(s) = \frac{1}{\sqrt{1-(\frac{v(s)}{c})^2}}$ as functions of the travelled distance s along its curved path. A small angle approximation $\frac{\mathrm{d}y}{\mathrm{d}s} = \sin\phi(s) \approx \phi(s)$ has been applied, yielding the lateral deflection as a function of s

$$y(s) = \int_0^s \phi(s')\mathrm{d}s' \,. \tag{3.6}$$

The deflection at the end of the trajectory in a water phantom without air gap (i.e. $d_{\mathrm{air}} = 0$) has thus been obtained by analytical integration as

$$\begin{aligned} \Delta y &= y(s = R_0) \\ &= \frac{7}{30}\frac{qB_0\alpha^2}{\sqrt{2m_0}}(2m_0c^2)^3 \left[\sqrt{1+\frac{E_0}{2m_0c^2}}\left(3\left(\frac{E_0}{2m_0c^2}\right)^2 - 4\left(\frac{E_0}{2m_0c^2}\right) + 8\right) - 8\right]. \end{aligned} \tag{3.7}$$

In an analogous manner, the longitudinal position $x(s)$ has been obtained by assuming $\frac{\mathrm{d}x}{\mathrm{d}s} = \cos\phi(s) \approx 1 - \frac{\phi(s)^2}{2}$ which yields

$$x(s) = s - \frac{1}{2}\int_0^s \phi^2(s')\mathrm{d}s' \,. \tag{3.8}$$

This term has been treated non-relativistically $\left(\text{i.e. } \gamma = 1 \text{ and } v(s) = \sqrt{\frac{2E(s)}{m_0}}\right)$ and thus the overall retraction length was quantified by

$$\Delta x = R_0 - x(R_0) = \frac{q^2 B_0^2 \alpha^3 E_0^{3p-1}}{2m_0} \frac{2p^2}{(4p-1)(3p-1)} \,. \tag{3.9}$$

The model was stated to be applicable to slab phantom geometries of arbitrary material thickness and composition by addition of the deflections obtained in each layer. For air gaps, energy loss has been assumed to be negligible, yielding

$$d_{\mathrm{air}} = x_{\mathrm{air}}(s) = s - \frac{q^2 B_0^2 s^3}{12 m_0 E_0} \text{ and } y_{\mathrm{air}}(s) = \frac{q B_0 s^2}{2\sqrt{2 m_0 E_0}} \,. \tag{3.10}$$

An advantage of the AI model is that the whole curved beam trajectory can be calculated from $x(s)$ and $y(s)$, which is important for treatment planning and dosimetric verification. However, the model cannot be easily adapted to realistic, inhomogeneous magnetic fields due to the pathlength parametrisation and the need for an analytical description of the magnetic flux density distribution.

Trigonometric model

In the work of Wolf and Bortfeld (2012), no concrete compensation strategy for the beam deflection has been proposed. This problem has been addressed by a more recent paper (Hartman et al., 2015). Here, a simplified trigonometric (TG) model has been introduced in order to propose a beam deflection correction strategy. Several assumptions have been made to enable a direct trigonometric quantification of the proton beam deflection without the use of more complex methods such as integration. Firstly, the change of the gyroradius due to energy loss in matter has been neglected, i.e. $r(s) = r_0$. Secondly, longitudinal beam retraction was not taken into account, i.e. $\Delta x = 0$ and $x(s = R_0) = R_0$. Following these approximations and Figure 3.1b, the lateral deflection in the water phantom (with $d_{\mathrm{air}} = 0$)

has been expressed as

$$\Delta y = r_0 \left(1 - \cos \left[\arcsin \left(\frac{R_0}{r_0} \right) \right] \right) , \tag{3.11}$$

which can be simplified to

$$\Delta y = r_0 - \sqrt{r_0^2 - R_0^2} \, . \tag{3.12}$$

As a third approximation, the proton motion was assumed to be non-relativistic ($\gamma = 1$ and $v(s) = \sqrt{\frac{2E(s)}{m}}$), which yields a constant gyroradius of

$$r_0 = \frac{\sqrt{2mE_0}}{qB_0} \approx 14.4 \frac{\sqrt{E_0}}{B_0} \, \mathsf{T} \;\; \mathsf{cm} \;\; (\mathsf{MeV})^{-1/2} \, . \tag{3.13}$$

The airgap of thickness d_{air} in front of the water phantom has been accounted for by replacing R_0 with $(R_0 + d_{\mathrm{air}})$, assuming that energy loss in air is negligible.

A correction strategy for the deflection has been proposed by applying an angle correction to the entrance direction $\vec{v_0}$ of the beam. According to Figure 3.1b, it was obtained by

$$\Delta \vartheta = \arctan \left(\frac{y(R_0)}{x(R_0)} \right) = \arctan \left(\frac{\Delta y}{R_0} \right) . \tag{3.14}$$

The authors stated that this angle correction could be implemented either by pencil beam scanning magnets or by an isocentric gantry rotation around the phantom. This will be discussed in section 3.1.3.

Summary

Although both the AI and the TG model offer a reasonable first approach to the problem of magnetic proton beam deflection in a transverse uniform magnetic field, they have their respective shortcomings. The AI model relies on a small angle approximation which is problematic for large deflection angles, treats retraction non-relativistically and does not offer a compensation strategy for the Bragg peak deflection. The TG model neglects relativistic effects, beam retraction and the decreasing gyroradius as a function of penetration depth. Neither the AI nor the TG model seem applicable to a realistic, i.e. non-uniform, magnetic field and patient anatomy. Aiming to provide a solution which is more accurate and versatile than these two models, but faster than Monte Carlo approaches, an alternative model

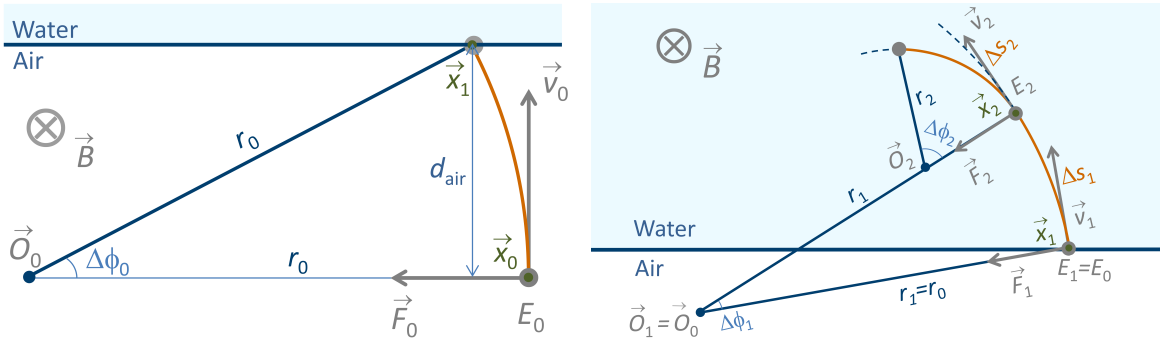

Figure 3.2: Geometrical representation of the proposed model (RAMDIM). The proton beam deflection in air is calculated trigonometrically assuming no energy loss (a), whereas a changing gyroradius due to energy loss is taken into account in water (b). Symbols are explained in the text. Figure reprinted from Schellhammer and Hoffmann (2017).

is therefore presented and verified in the following sections.

3.1.2 New Model Formulation

The model proposed in this thesis is an iterative analytical method to reconstruct the trajectory of a monoenergetic proton beam based on simple physics principles and geometrical considerations. It contains less critical approximations than currently available analytical models and offers a correction strategy for the predicted beam deflection and retraction. It is called Raytracing Algorithm for Magnetic Deflection of Ions in Media (RAMDIM).

Incremental reconstruction of the proton beam trajectory

Let us consider the geometry presented in section 3.1.1 and Figure 3.2 and let the entry position of the proton beam to the magnetic field be $\vec{x}_0 = (x_0, y_0, z_0)$. The initial gyroradius caused by the magnetic field is (cf. equation 3.3)

$$r_0 = \frac{\gamma m_0 v_0}{qB_0} = \frac{\sqrt{2m_0E_0(1+\frac{E_0}{2m_0c^2})}}{qB_0}\,. \tag{3.15}$$

The first relevant point of the trajectory is the entrance position of the proton beam at the surface of the water phantom $\vec{x}_1$. Energy loss inside the airgap is considered to be

negligible, therefore $\vec{x}_1$ is obtained by

$$\vec{x}_1 = \boldsymbol{R}(\Delta\phi_0) \cdot \vec{x}_0 \,, \tag{3.16}$$

with the rotation matrix $\boldsymbol{R}(\Delta\phi_0)$ rotating the point $\vec{x}_0$ counterclockwise through an angle $\Delta\phi_0$ about the center of rotation $\vec{O}_0 = (x_0, y_0 + r_0, z_0)$ (see Figure 3.2a). $\Delta\phi_0$ satisfies

$$\Delta\phi_0 = \arcsin(\frac{d_{\text{air}}}{r_0}) \,. \tag{3.17}$$

Inside the water phantom, the energy loss is modeled by the continuous slowing down approximation (ICRU, 1993) and discretised into small steps of constant energy and hence constant gyroradius (analogous to Figure 3.2b). The energy step size ϵ is chosen for every simulation such that the studied parameters, i.e. Δy, Δx and the correction parameters, are independent of ϵ within the decimal precision they are given in. Following equation 3.4, for each energy step i ($i = 1, ..., n$ with $n = \lfloor \frac{E_0}{\epsilon} \rfloor$) the travelled path length in water, s_i, can be calculated from (see eq. 3.4)

$$s_i = R_0 - \alpha E_i^p \,, \tag{3.18}$$

which results in an incremental deflection angle of

$$\Delta\phi_i = \frac{s_{i+1} - s_i}{r_i} = \frac{\Delta s_i}{r_i} \tag{3.19}$$

with the energy-dependent gyroradius $r_i = \frac{\sqrt{2m_0 E_i (1 + \frac{E_i}{2m_0 c^2})}}{qB_0}$ (in analogy to equation 3.15). The next particle position $\vec{x}_{i+1}$ is obtained by applying the rotational matrix of angle $\Delta\phi_i$ to $\vec{x}_i$, i.e. $\vec{x}_{i+1} = \boldsymbol{R}(\Delta\phi_i) \cdot \vec{x}_i$. Here, the center of rotation $\vec{O}_i$ is determined by (cf. Figure 3.2a)

$$\vec{O}_i = \frac{r_i}{|\vec{O}_{i-1} - \vec{x}_i|} (\vec{O}_{i-1} - \vec{x}_i) \,. \tag{3.20}$$

Thus, the proton trajectory is fully reconstructed until reaching the Bragg peak at step $i = n$. The overall deflection Δy and retraction Δx are then obtained as the projections of the difference between the Bragg peak positions $\vec{x}_n$ with and without magnetic field. It was verified that the total travelled pathlength is equal to the proton range within 0.1 mm accuracy, i.e. $s_n - R_0 < 0.1$ mm.

The algorithm has been realised in MATLAB (Release 2015b, The MathWorks, Inc., Nat-

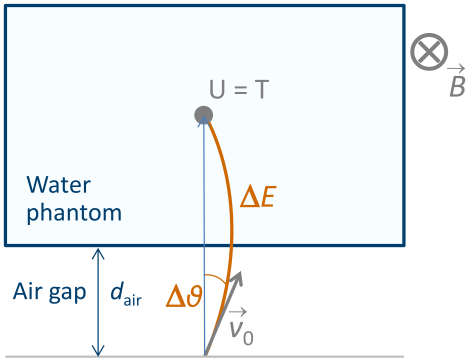

Figure 3.3: The proposed correction algorithm includes a correction of the proton energy ΔE_0 and entrance angle $\Delta\vartheta$ such that the actual Bragg peak location U coincides with the intended position T. Figure adapted from Schellhammer and Hoffmann (2017).

ick, Massachusetts, United States).

Correction strategy

As an advancement to the TG model, a correction strategy is proposed that simultaneously adjusts the proton beam entrance angle and energy (see Figure 3.3). The angle correction $\Delta\vartheta$ compensates for the lateral deflection of the Bragg peak and can only be applied by pencil beam scanning magnets. The energy correction ΔE_0 accounts for the retraction caused by the path curvature and has not been considered before. Both correction parameters are optimised such that the distance to agreement (DTA) between the corrected Bragg peak position $\vec{x}_{n,\mathrm{corr}} = \vec{x}_n(\vec{B}, \vartheta_0 + \Delta\vartheta, E_0 + \Delta E_0)$ and the intended position $\vec{x}_{n,0} = \vec{x}_n(0\,\mathrm{T}, \vartheta_0, E_0)$

$$DTA = |\vec{x}_{n,\mathrm{corr}} - \vec{x}_{n,0}| \tag{3.21}$$

is minimised. This bi-parameter optimisation is performed numerically using the MATLAB Optimisation Toolbox function `fminsearch`, which implements the simplex search method (Lagarias et al., 1998).

As an alternative to the angle correction, a patient shift has been suggested by Moteabbed et al. (2014). However, the deflection of a single Bragg peak strongly depends on the beam energy, entrance angle and the irradiated geometry, and therefore cannot completely be compensated for by a constant shift. Another alternative is the direct implementation of the magnetic field-induced beam deflection into the treatment planning system.

3.1.3 Evaluation of Analytical and Numerical Models

Setup and parameters

The RAMDIM method, as described in section 3.1.2, has been used to predict the trajectories of monoenergetic proton pencil beams of energies E_0 between 60 MeV and 250 MeV in a uniform transversal magnetic field of magnetic flux density B_0. Selected example values for B_0 were 0.5 T as a commonly used flux density in open MRI systems, and 1.5 T and 3 T as typical values for diagnostic imaging (Lagendijk et al., 2014a). The trajectories were studied in two different geometries: one with a water phantom alone, and one with an air gap between the phantom and the beam nozzle of thickness d_{air}. The parameter $d_{\mathrm{air}} = 25$ cm was chosen by way of example as a typical distance between the beam nozzle and the patient.

The lateral deflection Δy and longitudinal retraction Δx were calculated as functions of E_0 and B_0 with both the new model (RAMDIM) and the two analytical models (AI and TG, as discussed in section 3.1.1). Currently being the most accurate method for proton trajectory prediction, published values obtained by Monte Carlo particle tracking (Raaymakers et al., 2008; Moteabbed et al., 2014; Li, 2015; Moser, 2015) were compared to the results gained with the three models. Furthermore, the capability of RAMDIM to handle anatomical heterogeneities was tested exemplarily by calculating the proton beam trajectory in a phantom consisting of both bone and water. Correction parameters $\Delta\vartheta$ and ΔE_0 were calculated and compared to the TG method, and beam trajectories obtained with both correction methods were reconstructed in order to evaluate whether a distance remains to the intended Bragg peak position.

The required decimal precision of results was chosen to be 0.1 mm for Δx and Δy, 0.1° for $\Delta\vartheta$, and 0.1 MeV for ΔE_0. Accordingly, the energy step size ϵ was reduced until these parameters were constant on the first decimal place, yielding a required step size of $\epsilon = 0.1$ MeV. This corresponds to a steplength in water Δs (see eq. 3.18 and 3.19) of up to 0.3 mm for high proton energies ($E_i = 250$ MeV) and down to $4 \cdot 10^{-4}$ mm for low energies ($E_i = 0.1$ MeV).

Calculations were carried out on a PC workstation with 8 GB RAM and a 64 Bit Intel Core i3-3220 dual core processor running at 3.3 GHz. The calculation for one experiment (defined by E_0, B_0 and d_{air}) took less than 0.07 s for Δx and Δy, and less than 28 s for $\Delta\vartheta$ and ΔE_0 for all studied energies and magnetic flux densities.

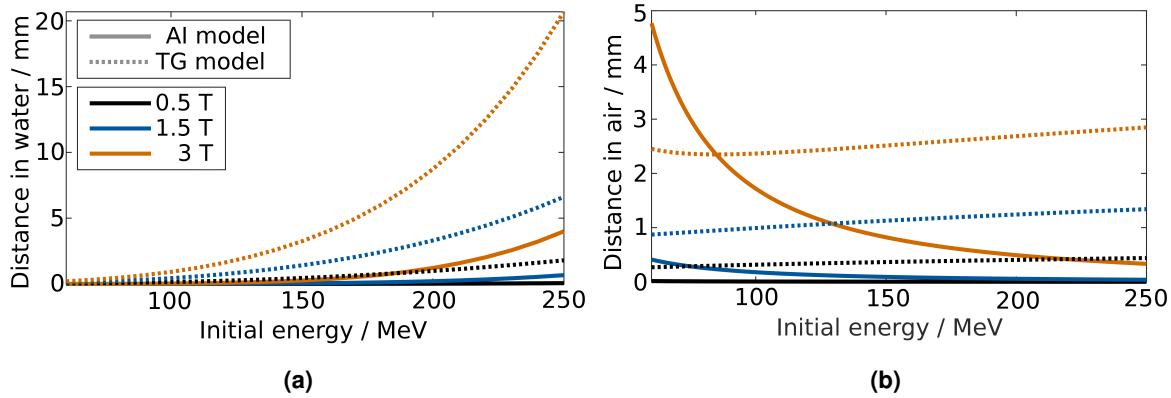

(a) (b)

Figure 3.4: Euclidean distance of positions calculated with the two previously published analytical models to those calculated with RAMDIM. (a): Distance in water between Bragg peak positions inside the phantom alone, (b): distance in air of beam entrance position to the water phantom behind an airgap of $d_{\mathrm{air}} = 25\,\mathrm{cm}$. Figure adapted from Schellhammer and Hoffmann (2017).

Bragg peak deflection and retraction

First, the results obtained with RAMDIM are compared to those of the two analytical models discussed in section 3.1.1. A discussion of differences and an interpretation of results follow in section 3.1.4.

Figure 3.4a depicts the Euclidean distance of Bragg peak positions obtained by the AI and TG model to those obtained with RAMDIM in water. As can be appreciated from this figure, the distance increases with increasing energy and magnetic flux density from 0 cm for 60 MeV and 0.5 T up to 2.1 cm for the TG model and 0.4 cm for the AI model at 250 MeV and 3 T.

For a comparison of the models inside the air gap, the difference in water phantom entrance positions behind an air gap of thickness $d_{\mathrm{air}} = 25\,\mathrm{cm}$ are depicted in Figure 3.4b. The distance to the results of the TG model increases with increasing proton energy up to 2.8 mm for 250 MeV and 3 T. As opposed to that, for the AI model it increases with decreasing energy up to 4.8 mm at 60 MeV and 3 T.

In the next step, the AI, TG and RAMDIM are compared to published results obtained by Monte Carlo particle tracking in a water phantom ($d_{\mathrm{air}} = 0$). An overview of calculated deflection and retraction values Δy and Δx in water is given for different uniform magnetic flux densities and beam energies in Table 3.1. Differences of the three analytical models to the reference results are displayed in Figure 3.5.

Table 3.1: Predicted lateral deflection Δy and longitudinal retraction Δx of a monoenergetic proton beam with initial energy E_0 at the Bragg peak. The beam traverses a water phantom ($d_{\mathrm{air}} = 0$) in a uniform transverse magnetic field of flux density B_0. Results are given for the new method (RAMDIM) and the AI and TG models (eq. 3.7, 3.9 and 3.11) in relation to published Monte Carlo results (ref.).

B_0/	E_0/	Δy / mm				Δx / mm			Reference
T	MeV	RAMDIM	AI	TG	ref.	RAMDIM	AI	ref.	(ref.)
0.35	60	0.2	0.2	0.2	0.2	0.0	0.0	0.0	Moser et al. 2015
	150	2.7	2.7	2.4	2.5	0.0	0.0	0.1	Moser et al. 2015
	250	12.4	12.4	11.2	11.8	0.3	0.3	1.2	Moser et al. 2015
0.5	90	0.9	0.9	0.8	1.0				Raaymakers et al. 2008
	90				1.2				Moteabbed et al. 2014
	200	9.2	9.2	8.2	10.0				Moteabbed et al. 2014
1.0	60	0.5	0.5	0.4	0.5	0.0	0.0	0.0	Moser et al. 2015
	150	7.8	7.8	6.9	7.3	0.3	0.3	1.5	Moser et al. 2015
	250	35.4	35.5	32.3	32.8	2.3	2.6	3.5	Moser et al. 2015
1.5	90	2.6	2.6	2.2	3.0				Moteabbed et al. 2014
	200	27.4	27.5	24.8	28				Moteabbed et al. 2014
3.0	60	1.5	1.5	1.3	1.4	0.1	0.1	0.1	Moser et al. 2015
	90	5.1	5.1	4.5	5.0				Raaymakers et al. 2008
	120	12.0	12.1	10.7	11.0	1.0	1.0	2.0	Li 2015
	150	23.2	23.5	21.1	22.8	2.5	2.6	3.5	Moser et al. 2015
	180	39.7	40.3	36.9	38	5.3	5.7	6.0	Li 2015
	250	103.4	106.6	103.1	98.9	20.7	23.1	20.5	Moser et al. 2015

For all the models, the differences increase with increasing proton energy and magnetic flux density. This can be expected, as Δx and Δy increase with increasing path length and Lorentz force, so that differences due to approximations become more pronounced. However, deviations of the three models behave differently from each other.

For the AI model, the lateral deflection Δy agrees within 2.5 mm with Monte Carlo reference results up to proton energies of 200 MeV for all B_0 considered, except for 250 MeV at 3 T (8 mm). The calculated longitudinal retraction Δx agrees within 1.5 mm with the reference for all studied setups, except for 250 MeV at 3 T (3 mm). Here, the lateral deflection tends to be overestimated, whereas retraction by trend seems to be underestimated by the AI model.

For the TG model, the deflection Δy agrees with Monte Carlo results within 2 mm for all setups except for 200 MeV and 1.5 T, and 250 MeV and 3 T, where the deviations amount to 3.2 mm and 4.2 mm, respectively. The TG model tends to underestimate Δy. The full neglection of the longitudinal retraction of the Bragg peak leads to differences in Δx of up

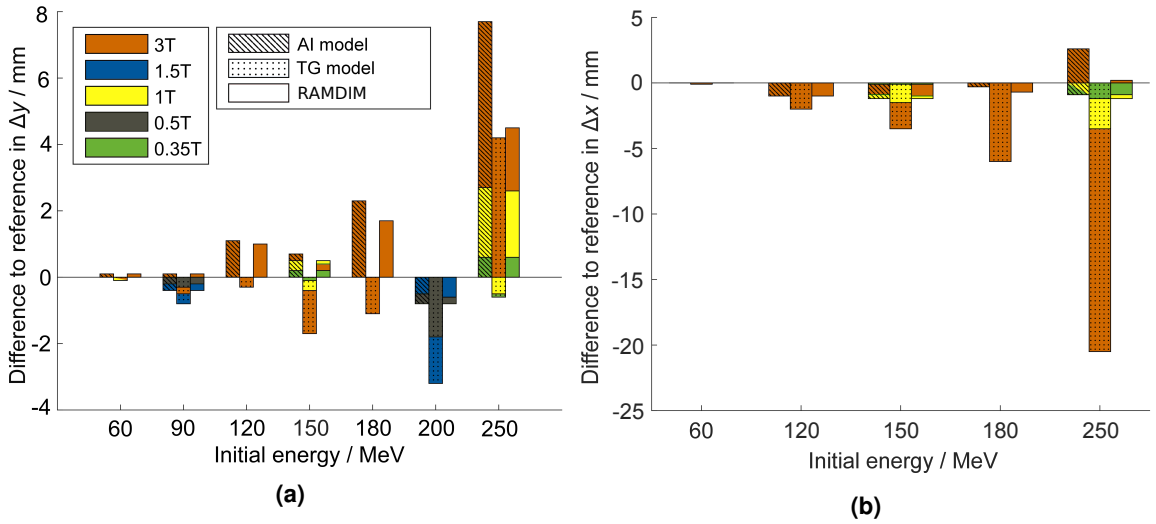

Figure 3.5: Difference in Bragg peak deflection Δy and retraction Δx between results of the analytical models and Monte Carlo results for the studied set of proton energies and magnetic flux densities (see Table 3.1). Positive values indicate an overestimation of the three models in relation to the particle tracking results, and negative values indicate an underestimation. Colored bars individually span from zero (i.e., no stacking). Figure reprinted from Schellhammer and Hoffmann (2017).

to 2.1 cm for 250 MeV and 3 T.

Results obtained with RAMDIM show an agreement with the reference results in Δy within 2 mm for all studies setups, except for 250 MeV at 1.5 T (2.6 mm) and 3 T (4.6 mm). The retraction Δx agrees within 1.5 mm for all studied energies and magnetic flux densities. RAMDIM shows a trend of overestimating lateral deflection and underestimating longitudinal retraction.

A statistical comparison of the accuracy of the three models in relation to the Monte Carlo results is displayed in Figure 3.6. Regarding the lateral deflection Δy, the three models show only small differences in both median and average deviation, which amount to 0.5 mm and 1 mm, respectively. However, the upper percentiles (i.e. 75 % and 91 %) deviate stronger from zero for the TG model than for the other two models, and the AI model shows a strong outlier of 8 mm at 250 MeV and 3 T. For the longitudinal retraction Δx, the median and average deviation of the new model and the AI model are comparably low (below 1 mm), but RAMDIM shows a smaller 91 %-percentile and no outlier. As retraction is neglected in the TG model, all studied statistical measures are highly increased as compared to the two other models. The sample size for this inter-model comparison has been

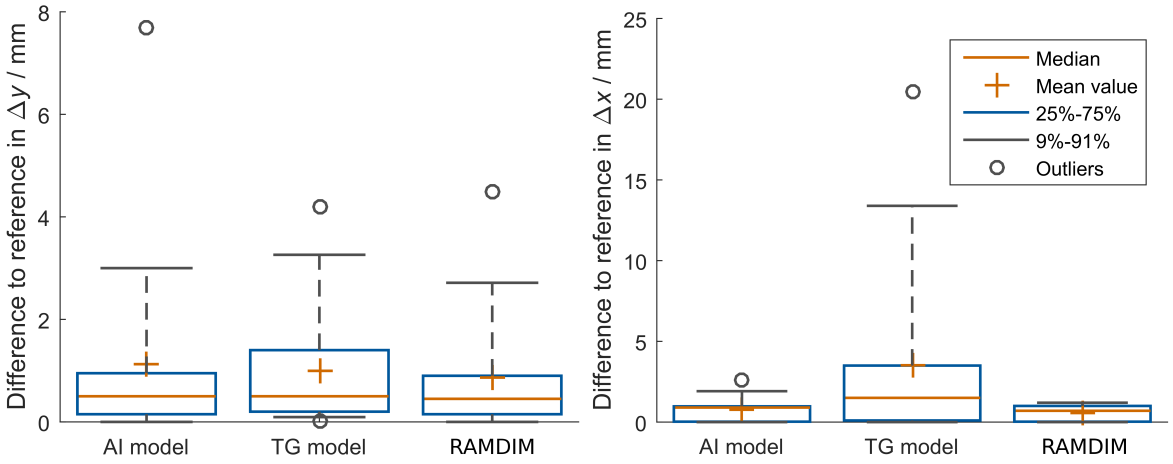

Figure 3.6: Boxplots of absolute differences in Bragg peak deflection Δy and retraction Δx between the different models and Monte Carlo reference results (see Table 3.1). Figure reprinted from Schellhammer and Hoffmann (2017).

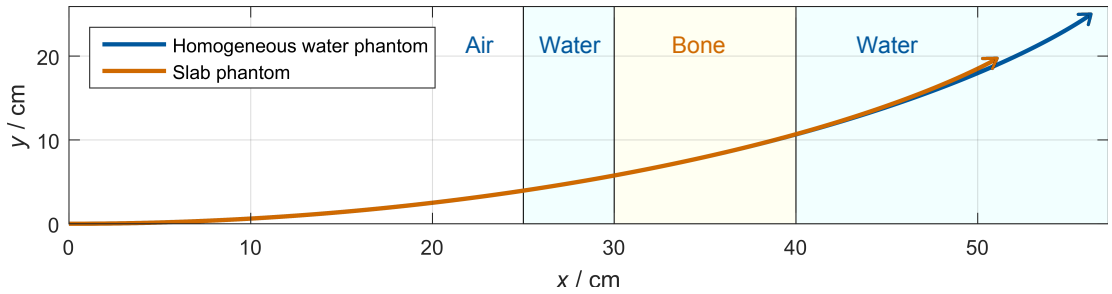

Figure 3.7: 250 MeV proton beam trajectory in a magnetic field of 3 T through different phantoms behind an airgap of $d_{\mathrm{air}} = 25$ cm calculated with RAMDIM. Blue: homogeneous water phantom, orange: slab phantom with bone insert of 10 cm thickness. The Bragg peak position is indicated by the arrowhead of the trajectory.

limited to 11 and 16 data points for retraction and deflection, respectively.

The capability of RAMDIM to predict the proton beam trajectory in heterogeneous media is shown in Figure 3.7. As a demonstration case, a 250 MeV proton beam traversing a water phantom with a 10 cm bone insert has been modelled in a field of $B_0 = 3$ T. As expected, the proton range is reduced according to equation 3.4. Additionally, for the same depth, the curvature of the beam behind the bone insert is stronger than in a homogeneous water phantom due to the increased energy loss in bone. In the same manner, arbitrary geometries can be studied using this model.

Table 3.2: Beam energy and angle correction parameters for different initial energies and magnetic flux densities for a distance between the phantom surface and the entrance position of the beam to the magnetic field of $d_{\mathrm{air}} = 25\,\mathrm{cm}$.

B_0/ T	E_0 / MeV	RAMDIM ΔE_0 / MeV	RAMDIM $\Delta\vartheta/^\circ$	TG model $\Delta\vartheta/^\circ$
0.5	60	0.1	3.6	3.3
	100	0.1	3.2	3.3
	150	0.1	3.3	3.3
	200	0.1	3.6	3.6
	250	0.1	4.0	4.0
1.5	60	0.5	10.7	11.1
	100	0.5	9.6	10.0
	150	0.6	9.8	10.1
	200	0.8	10.7	11.0
	250	1.1	12.0	12.3
3	60	2.0	21.5	24.6
	100	2.1	19.3	21.5
	150	2.5	19.7	21.9
	200	3.3	21.6	24.3
	250	4.7	24.4	28.2

Beam correction parameters

To compensate for the deflection of the Bragg peak, the calculated correction parameters $\Delta\vartheta$ and ΔE_0 are presented for different proton energies E_0 and magnetic flux densities B_0 in Table 3.2. The beam energy correction calculated with our model ranges from $\Delta E_0 =$ 0.1 MeV (0.2 %) for 60 MeV and 0.5 T up to $\Delta E_0 = 4.7\,\mathrm{MeV}$ (2 %) for 250 MeV and 3 T. The angle correction ranges from $\Delta\vartheta = 3.6^\circ$ for 60 MeV and 0.5 T up to $\Delta\vartheta = 24.4^\circ$ for 250 MeV and 3 T. The difference to the correction angle from the TG model is smaller than 0.5° for magnetic flux densities up to 1.5 T, but exceeds to 3.8° (16 %) at 250 MeV and 3 T.

As an example, proton trajectories modelled with RAMDIM for both correction parameter sets are depicted for $E_0 = 200\,\mathrm{MeV}$ and $B_0 = 3\,\mathrm{T}$ in Figure 3.8. As the correction method of the TG model does not include an energy correction, the Bragg peak retraction is not compensated for. Additionally, the lateral deflection Δy is overcompensated by a too large correction angle. Therefore, the DTA between the intended Bragg peak position without a magnetic field and its corrected position inside the field (see equation 3.21 and Figure 3.9) is non-zero. It ranges from 0.3 mm for 60 MeV and 0.5 T up to 4.3 cm for 250 MeV and 3 T. With the new correction method presented here, the calculated DTA is below 0.1 mm for all

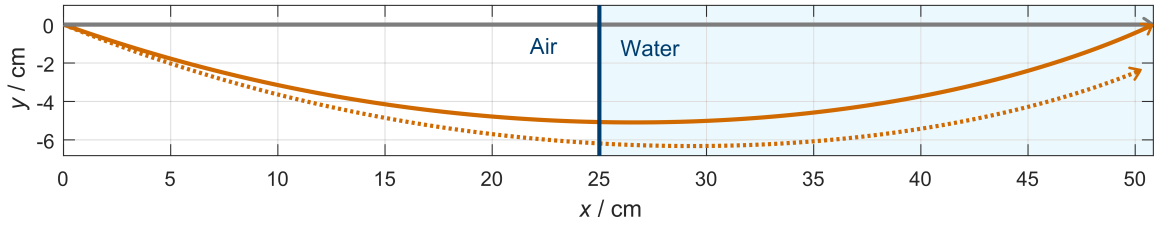

Figure 3.8: 200 MeV proton beam trajectory through an airgap of thickness $d_{\mathrm{air}} = 25\,\mathrm{cm}$ and a water phantom calculated with RAMDIM. Grey: without magnetic field, orange: $B_0 = 3\,\mathrm{T}$. The RAMDIM correction method ($\Delta\vartheta = 21.6°$, $\Delta E_0 = 3.3\,\mathrm{MeV}$, solid line) and that of the TG model ($\Delta\vartheta = 24.3°$, $\Delta E_0 = 0$, dotted line) have been applied to the beam. The Bragg peak position is indicated by the arrowhead of the trajectory. Figure reprinted from Schellhammer and Hoffmann (2017).

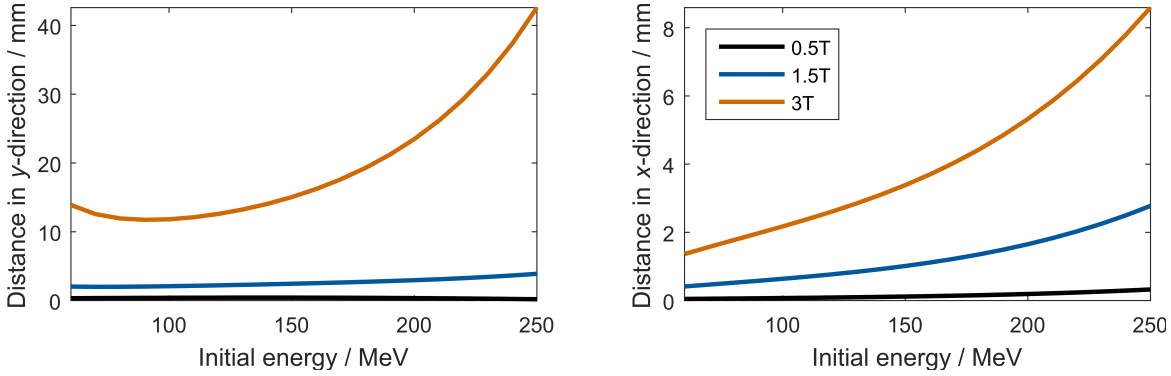

Figure 3.9: Remaining distance, DTA, between intended and achieved Bragg peak positions when the correction of the TG model is applied. Trajectories were calculated with the new model for a water phantom behind an airgap of $d_{\mathrm{air}} = 25\,\mathrm{cm}$. With the new correction method, DTA is less than 0.1 mm for all studied E_0 and B_0 configurations. Figure reprinted from Schellhammer and Hoffmann (2017).

studied E_0 and B_0 configurations.

In addition to these differences, it is debatable whether the beam angle correction can be implemented by a gantry rotation, as stated by Hartman et al. (2015). To see this, assume for example the intended Bragg peak position (indicated by "T" in Figure 3.1a) to coincide with the isocenter of rotation of the gantry. A gantry rotation will then result in a concentric displacement of the actual Bragg peak position U around T, but it will not compensate for the deflection, i.e. render U = T. Transferring this consideration to arbitrary positions of T, it follows that a gantry rotation alone around a fixed isocenter cannot compensate for the proton Bragg peak deflection. Hence it is concluded that a full compensation can only be realised by a pencil beam scanning system, which adjusts the entrance angle of the beam.

3.1.4 Discussion

Bragg peak deflection and retraction

The differences found between the calculated beam deflection Δy and retraction Δx at the Bragg peak can be attributed to the principles of the models as described in sections 3.1.1 and 3.1.2.

Wolf and Bortfeld (2012) applied a small angle approximation to quantify Δy and Δx in their AI model (see chapter 3.1.1). This approximation becomes inaccurate for large pathlengths. For example, the deflection angle at the phantom entrance position behind the air gap ($d_{\mathrm{air}} = 25\,\mathrm{cm}$) is for 200 MeV and 3 T already as high as 41° (see eq. 3.17). Thus, the assumptions of $\frac{\mathrm{d}y}{\mathrm{d}s} = \sin\phi(s) \approx \phi(s)$ and $\frac{\mathrm{d}x}{\mathrm{d}s} = \cos\phi(s) \approx 1 - \frac{\phi(s)^2}{2}$ constitute a systematic overestimation of the lateral deflection $\Delta y = y(R_0)$ and an underestimation of the longitudinal retraction $\Delta x = R_0 - x(s)$. The deflection angle in water increases with increasing beam energy and magnetic flux density, giving rise to increasing discrepancies relative to the reference data. In addition, the neglection of relativistic effects for the calculation of Δx contributes to an increasing uncertainty with increasing energy. These trends can be clearly observed in Figures 3.4a and 3.5a. In air, the effect of a decreasing gyroradius with decreasing energy dominates, therefore the travelled pathlength and deflection angle increase with decreasing energy. As the accuracy of the model decreases with increasing deflection angle, this leads to an opposite trend as compared to the lateral deflection, as is appreciated from Figures 3.4b and 3.5a.

Similarly, one can observe how the approximations brought forward by Hartman et al. (2015) affect the accuracy of the predictions of the TG model. The model neglects retraction, the changing gyroradius due to energy loss and relativistic effects. The accuracy of these approximations decreases with increasing magnetic flux density and proton energy, as is depicted in Figure 3.4. Note that differences in Figure 3.4b are solely due to the neglection of relativistic effects, which leads to an underestimation of the gyroradius. The trend to underestimate the deflection in water, as depicted in Figure 3.5a, can be ascribed to the overestimation of the gyroradius by assuming $r(s) = r_0$. In addition, it was shown that the assumption of a negligible longitudinal Bragg peak retraction exceeds an accuracy of 2 mm already at intermediate energies (see Figure 3.5a). Both methods are therefore mainly applicable for low to intermediate uniform magnetic flux densities and proton energies.

The RAMDIM model presented in the current work does not rely on these assumptions and shows an equally good or better agreement to Monte Carlo results over the whole energy range from 60 MeV to 250 MeV. The remaining differences can be attributed to the approximations of the model, i.e. neglecting scattering, energy-loss fluctuations, range straggling, generation of secondary particles, and energy loss in air. Those simplifications were applied to reduce calculation time, but can in principle be included due to the structure of the model being a simplified particle tracking method. The tendency of overestimating lateral deflection and underestimating longitudinal retraction might result from the spectral dispersion of the proton beam due to the magnetic field (Moser, 2015), which is not included in the model. Another factor of uncertainty is the proton range R_0, which has been approximated by equation 3.4 and used as an estimate for the position of the Bragg peak. R_0 deviates from measured Bragg peak positions (Paul, 2013; Schardt et al., 2008) by less than 0.4 mm up to proton energies of 200 MeV.

On the other hand, results obtained by Monte Carlo particle tracking were used in this publication as reference data. However, this approach is theoretical in nature and its accuracy strongly depends on the choice of input parameters and physics models. Consequently, dosimetric measurements have to be carried out for a reliable evaluation of the different models. While this study primarily aimed to introduce the new method, this will be subject to future studies.

A pencil beam algorithm has recently been introduced for dose calculation in magnetic fields (Padilla-Cabal et al., 2018), which is based on an algorithm similar to RAMDIM (Fuchs et al., 2017). Here, a Runge-Kutta method is used for each particle step instead of the analytical solution as implemented in RAMDIM. As the proton velocity is considered to be constant in each calculation step, the analytical solution applies not only in vacuum but also in media. The Runge-Kutta method is therefore expected to yield equivalent results while being slightly more time-consuming.

Beam correction

The proposed strategy for a compensation of the Bragg peak deflection includes an adjustment of the initial proton beam energy and entrance angle. It was shown that this method effectively repositions the Bragg peak to the intended spot for all studied beam energies and magnetic flux densities. The range difference corresponding to ΔE_0 ranges

between 0.01 cm (0.3 %) for 60 MeV and 0.5 T and 1.27 cm (3.3 %) for 250 MeV and 3 T (see Table 3.2 and equation 3.4). The main factor of uncertainty for the proton range in a well-defined geometry is statistical pathlength straggling, and the standard deviation of the range due to this effect ranges between 1.2 % for 60 MeV and 1.1 % for 250 MeV (Janni, 1982; Gottschalk, 2011). Being comparably high, the energy correction should therefore not be neglected in MRiPT, especially for higher proton energies and magnetic flux densities.

The reason for the remaining discrepancy of the Bragg peak position corrected by the TG model is seen in the approximations mentioned above. The neglection of retraction constitutes an overestimation of the total path length, and the neglection of relativistic effects leads to an underestimation of the gyroradius and thus an overestimation of the beam deflection. Both approximations result in an overcompensation of the beam deflection.

The calculation time of RAMDIM is strongly decreased as compared to Monte Carlo models. It can be further reduced by using a higher-performing computer and by reducing the required accuracy, which was chosen conservatively in this study. It is expected to be possible to renounce the beam correction if the influence of the magnetic field will be directly implemented in an MRiPT treatment planning system.

It should be noted that the Bragg peak deflection and correction parameters given in this work are merely exemplary and will most likely be different in a realised MRiPT setup. It is expected that the distance to the scanning magnets will be larger to make room for the MR scanner, and that the non-uniform magnetic fringe field of the MR scanner will have to be taken into account. RAMDIM was presented here in a simplistic form for a first approach to the problem of magnetic deflection of the proton beam. However, the structure of the model allows for an easy extension to more realistic cases, especially including inhomogeneous magnetic fields and material compositions and range straggling. Magnetic flux density vectors of arbitrary distribution and phantom/patient geometries can be included due to the full reconstruction of the trajectory, which provides knowledge of the proton position at every iteration step. In addition to its reduced amount of approximations, the presented model thus offers a critically enhanced applicability compared to existing analytical models.

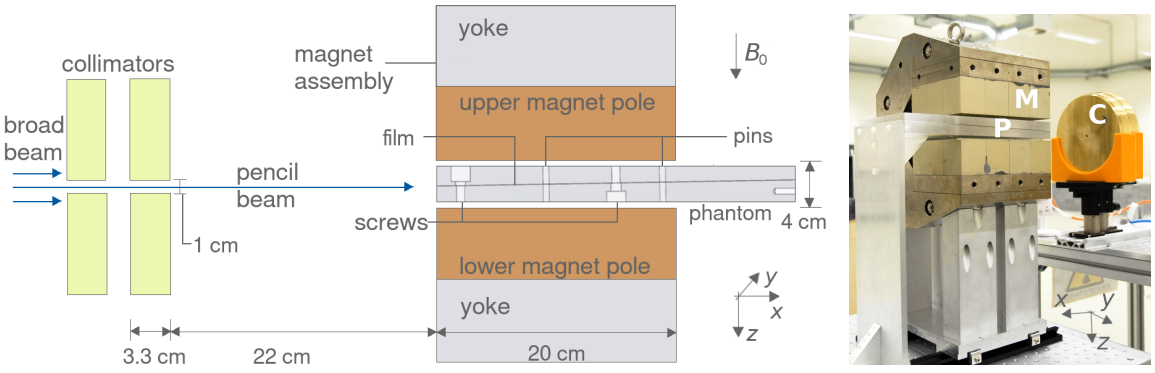

Figure 3.10: Schematic sagittal view (a) and photograph (b) of the experimental setup. The proton beam passed through collimators (C) and a slab phantom (P) placed inside the field of a permanent magnet (M). The dose in the phantom was measured using a Gafchromic film detector. A left-handed coordinate system is used. Photo edited for clarity. Figure adapted from Schellhammer et al. (2018b).

3.2 Monte Carlo Simulation and Experimental Verification

As shown in section 3.1, considerable distortions of the dose distribution of a proton beam in a magnetic field have been predicted. Particularly, the Bragg peak is expected to be laterally displaced by a few millimeters up to several centimeters, depending on the beam energy and magnetic flux density distribution. However, there is no clear consensus in literature on the exact amount of magnetic field-induced Bragg peak displacement to be expected (see section 3.1.3), and experimental benchmark data does not exist. Therefore, a first measurement thereof and a comparison against Monte Carlo-based predictions is presented in the following.

3.2.1 Verification Setup

The experimental setup developed for the validation measurement is depicted in Figure 3.10. It consists of a collimated proton beam, a slab phantom containing a horizontally placed film dosimeter, and a permanent magnet assembly.

The proton beam was generated by an isochronous cyclotron (C230, IBA, Louvain-La-Neuve, Belgium) at University Proton Therapy Dresden (UPTD). The horizontal static beam line was used and defined the x-axis of the setup. The beam was collimated to a cylindrical pencil beam of 10 mm diameter in order to prevent the magnet from being damaged by

direct radiation exposure. The collimated beam diameter at the phantom entrance was smaller than 1.5 cm (full width tenth maximum) thus sparing the magnet assembly. The two magnet poles had a size of $x_{\mathrm{pole}} \times y_{\mathrm{pole}} \times z_{\mathrm{pole}} = 20 \times 15 \times 5.9$ cm^3 each.

The slab phantom was produced from polymethyl methacrylate (PMMA) and mounted horizontally in the 4 cm wide air gap between the poles of a C-shaped permanent magnet assembly. It consisted of two slabs, such that a film dosimeter was placed horizontally in the central plane parallel to the beam, allowing to measure the full deflected beam trajectory. The contact area of the slabs was bevelled by $\alpha = 1°$ around the y-axis to reduce the dependence of the dose distribution on the film material and on possible air gaps between the phantom and the film (Zhao and Das, 2010). Two vertically oriented pins in the phantom and corresponding holes in the films ensured a reproducible alignment of the film relative to the phantom.

A self-developing Gafchromic EBT3 film detector of 280 µm thickness (Ashland, Covington, USA) was used to measure the planar dose distributions in the central plane of the proton beam. This dosimeter type was chosen over alternatives such as ionisation chambers, scintillators, thermoluminescent (TLD), optically stimulated luminescent (OSL) and gel dosimeters, because it provides a continuous two-dimensional measurement with submillimeter spatial resolution, that is well-established, easy to handle and readily available. As shown in a precedent study, Gafchromic films are largely unaffected by magnetic fields (Lühr et al., 2018).

The phantom incorporating the film detector was placed inside a transversal magnetic field (see Appendix, Figure B.4) produced by a magnet assembly comprising two $\mathrm{Nd_2Fe_{14}B}$ permanent magnet poles and a yoke. The maximum magnetic flux density of $B_0 = 0.95$ T was comparable to that of existing MR-integrated photon therapy systems with flux densities between 0.35 T and 1.5 T (Mutic and Dempsey, 2014; Fallone, 2014; Lagendijk et al., 2014b; Keall et al., 2014). The main field component defined the z-axis of the setup (pointing downwards), and caused a deflection of the proton beam in the positive y-direction. In order to measure the whole trajectory of the protons slowing down inside the main magnetic field, the beam energy was limited to 180 MeV. The experiment was performed with and without the magnet present.

Two-dimensional dose distributions $D(x, y)$ were obtained on the film plane. From these, the beam trajectory and Bragg peak displacement were extracted as follows. For each depth x, a univariate Gaussian function was fitted to the lateral beam profile and the max-

imum position $y_{\mathrm{T}}(x)$ was extracted. This yielded the beam trajectory $y_{\mathrm{T}}(x)$. To mimic a depth-dose curve measured by an ionisation chamber of 8 cm diameter, for each depth the predicted dose was integrated radially around $y_{\mathrm{T}}(x)$ with an integration radius of $r = 4$ cm. This resulted in the integral depth-dose curve,

$$IDD(x) = \int_0^{2\pi} \int_0^r D(x, \rho, \phi) \rho d\rho d\phi = \pi \int_{-r}^{r} D(x, y) |y - y_{\mathrm{T}}(x)| dy \,, \tag{3.22}$$

where ρ and ϕ are the polar coordinates (radius and polar angle, respectively). Both $y_{\mathrm{T}}(x)$ and $IDD(x)$ were smoothed to reduce statistical noise using a univariate spline fit. The mean of the first proximal 10 values of $y_T(x)$ were subtracted from $y_T(x)$ to achieve $y_T(0) \approx 0$. The range R_{80} was calculated from $IDD(x)$ as the depth of the beam at the 80 % distal end of the IDD maximum. The longitudinal Bragg peak retraction was defined as the difference between R_{80} with and without magnetic field. The lateral Bragg peak deflection was determined from the beam trajectory obtained with magnetic field as $y_{\mathrm{T}}(R_{80})$.

Details on the experimental setup, film handling, and an uncertainty estimation are given in Appendix A.

3.2.2 Monte Carlo Simulation

The measured data allowed for a verification of Monte Carlo based particle tracking simulations, being considered as the gold standard for dose calculation in radiation therapy planning (Paganetti, 2012). The measurement setup was simulated using the Geant4 toolkit version 10.2.p02 (Agostinelli et al., 2003; Allison et al., 2006).

Beam model definition

As the experimental proton beams were not monoenergetic, beam energy distributions corresponding to the nominal beam energies E_{nom} of the facility needed to be determined. For this purpose, in-water depth-dose curves were measured for 24 energies between 100 MeV and 215 MeV using a multi-layer ionisation chamber with 6 cm radius and an effective depth resolution of 1 mm (Giraffe, IBA Dosimetry, Schwarzenbruck, Germany) (Wohlfahrt et al., 2018). An analytical approximation of the Bragg curve (Bortfeld, 1997) was fitted to the measured data, yielding the proton range R_{80} and its energy spread σ_E. Ranges R_{80} were converted to mean initial proton energies E_0 using tabulated stopping power data (Berger

Table 3.3: Extract of the beam energies E_0 and energy spreads σ_E obtained from fit to depth-dose measurements for the nominal energies E_{nom}.

E_{nom} / MeV	E_0 / MeV	σ_E / MeV
100	101.8	0.8
120	121.9	1.0
140	141.8	1.2
160	161.9	1.2
180	181.8	1.3

et al., 2005). E_0 and σ_E are given in Table 3.3 for all studied energies.

The obtained energies E_0 exceeded the nominal energies E_{nom} by 1–2 MeV, as the nominal energies serve only as labels in the facility. The measured energy spread σ_E ranged between 0.8 MeV and 1.3 MeV. For 80 MeV, this data was extrapolated yielding $E_0(80\,\mathrm{MeV}) = 81.9\,\mathrm{MeV}$ and $\sigma_E(80\,\mathrm{MeV}) = 1.2\,\mathrm{MeV}$. E_0 and σ_E were used to define the beam for the Monte Carlo simulations.

If not stated differently, energies mentioned throughout this work refer to the nominal energies.

To acquire a realistic model of the beam, 2D beam profiles were measured close to the beam exit window (in a distance of 8 cm) using a pixelated scintillation detector with a resolution of 0.5 mm (Lynx, IBA Dosimetry, Schwarzenbruck, Germany) for seven energies between 100 MeV and 215 MeV. A fit of a two-dimensional Gaussian function to the data yielded a mean lateral spread of ${\sigma_0}^{(yz)} = (4.7 \pm 0.7)$ mm with a small trend of decreasing ${\sigma_0}^{(yz)}$ with increasing energy and a slightly higher spread in vertical (z) direction than in horizontal (y) direction.

Due to the collimators and the long air gap between the beam exit and the phantom, varying the initial beam spot size ${\sigma_0}^{(yz)}$ in the simulation between 0 and 8 mm showed no influence on the beam spot size at the phantom entrance larger than 0.1 mm. For simplicity, the initial beam profile was therefore modelled as an energy-independent Gaussian with a fixed unilateral spread of ${\sigma_0}^{(yz)} = 4.7\,\mathrm{mm}$.

A number of different recommendations for physics lists for proton therapy have been made in previous studies and by the Geant4, TOPAS and GATE collaborations:
`QGSP_BIC_HP_EMY` (Almhagen, 2015), `QGSP_BIC_HP_EMZ`, `QGSP_BERT_HP_EMY` and

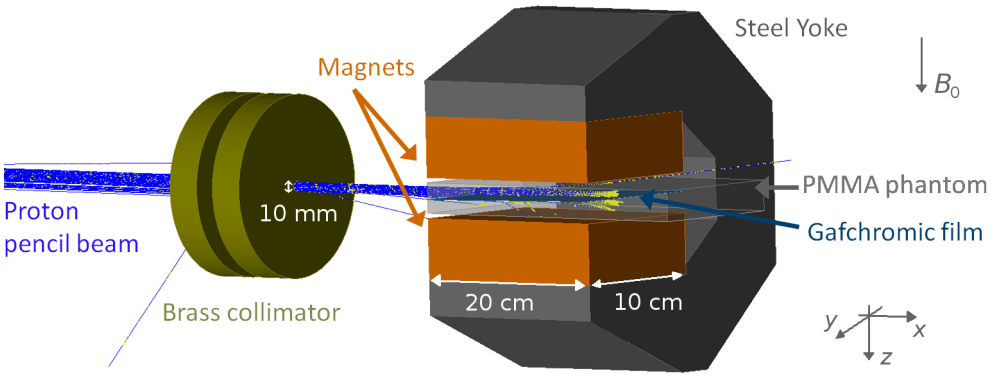

Figure 3.11: 3D representation of the deflection experiment as simulated by Geant4 Monte Carlo simulations.

QGSP_BERT_HP_EMZ, (Geant4 collaboration, 2013), HADRONTHERAPY_1 (Geant4 collaboration, 2014; J. Perl et al., 2016) and HADRONTHERAPY_2 (Geant4 collaboration, 2014), and QBBC_EMY and QBBC_EMZ (Grevillot et al., 2010; GATE collaboration, 2017). Since there is no clear consensus within these recommendations for a single superior physics list, all mentioned physics lists were included and tested in this study.

The mean excitation energy of water was set to 78 eV, which is the default value for Geant4 version 10 and higher, and is consistent with the revised ICRU report 73 (ICRU, 2009). Note that this value differs from the one used in tabulated stopping-power data (Berger et al., 2005) by 3 eV. Parameters defining the resolution of the simulation, i.e. secondary particle production threshold, maximum step length and dose scorer resolution, were defined by a convergence study: the parameter values were reduced until no change in the observables was found within a required precision. Observables were the proton range and energy spread with a required precision of 0.1 mm and 0.1 MeV, respectively. For increased simulation efficiency, the secondary particle production threshold was determined independently inside and outside of the phantom (the latter being referred to as *world*).

The RANMAR random number generator was chosen, as it provides $9 \cdot 10^8$ disjoint sequences with a length of 10^{30} numbers (James, 1990). The magnetic field was implemented using a corrected version (Schellhammer et al., 2017) of the Geant4 class HadrontherapyMagneticField3D given in the HADRONTHERAPY application example of Geant4.

Table 3.4: Geant4 simulation parameters.

Geant4 version	10.2.p02
Physics list	`QGSP_BERT_HP_EMZ`
Production threshold in *world*	5 mm
Production threshold in phantom	0.1 mm
Step limiter	0.1 mm
Scorer resolution	0.1 mm
Water mean excitation energy	78 eV
Random number generator	`RANMAR`

Beam model verification

As a verification for the thus defined beam model, depth-dose curves were scored in a water phantom (size $x_{\mathrm{wp}} \times y_{\mathrm{wp}} \times z_{\mathrm{wp}} = 35 \times 12 \times 12$ cm^3). For 24 energies, the range R_0 and energy spread σ_E were obtained by fitting the analytical Bragg curve (Bortfeld, 1997) to these depth-dose curves (as in section 3.2.2). These were then compared to those obtained from the experimental data.

Furthermore, two-dimensional beam profiles were measured at the phantom entrance position behind the collimators using the pixelated scintillation detector. Profiles were scored in the simulation at the same position. Spatial spreads at the phantom entrance position ${\sigma_{\mathrm{ph}}}^{(yz)}$ were extracted by fitting a bivariate Gaussian function to the obtained experimental and simulated planar dose profiles.

The physics model `QGSP_BERT_HP_EMZ` showed the smallest deviation to the experimental data and was thus chosen for the simulation, although differences between all studied models in range and energy spread were smaller than 0.2 mm and 0.05 MeV, respectively. The minimum required production threshold for the *world* was found to be 5 mm and the minimum required production threshold for the phantom, step limiter and scorer resolution were found to be 0.1 mm. This corresponds well with values found in previous studies (Grevillot et al., 2010; Kurosu et al., 2014).

Mean differences between the model and reference measurements were 0.2 mm in range (max. 0.5 mm), 0.23 MeV in energy spread (max. 0.35 MeV) and 0.1 mm in spatial spread (max. 0.2 mm). The beam model was thus accepted for the simulations. Relevant simulation parameters are summarised in Table 3.4.

Main simulation

For the deflection study (see Figure 3.11), the convergence study for the simulation resolution parameters was repeated with the range and the Bragg peak deflection as observables and a required accuracy of 0.1 mm. The same parameters were found as in the model building phase (5 mm for the *world* production threshold, and 0.1 mm for the phantom production threshold, step limiter and scorer resolution).

Dose was scored in the PMMA phantom at the position of the film detector, on a 20×15 cm^2 plane with a thickness of 30 µm corresponding to that of the active layer of an EBT3 film dosimeter. Beam trajectories and Bragg peak displacement were extracted from the dose distribution as described in section 3.2.1. The film dosimeter was not explicitly simulated to avoid boundary artefacts. PMMA was defined in the simulation by its measured density and its atomic composition, enabling Geant4 to calculate the mean excitation potential using tabulated data. The magnet assembly was included into the simulation to account for possible generation of secondary particles.

The magnetic field map for the simulation was generated using finite-element modelling (COMSOL Multiphysics, COMSOL AB, Stockholm, Sweden) and validated in all three magnetic field components by measurements at 5 mm resolution using an automated magnetometry setup (Gantz, 2017). Details on the magnetic model and an uncertainty estimation are given in Appendix B.

3.2.3 Experimental Verification

Measured beam deflection and Bragg peak dislocation

The influence of the magnetic field on the proton dose distribution could be observed on the film dosimeter signal, as depicted in Figure 3.12. The characteristic shape of the proton dose distribution was visible both with and without magnetic field. However, with magnetic field the beam followed a deflected trajectory resulting in a laterally shifted Bragg peak position.

The measured lateral deflection of the Bragg peak ranged from 1 mm for 80 MeV up to 10 mm for 180 MeV. Bragg peak retraction was within measurement uncertainty and ≤ 0.5 mm for all studied energies. As expected, the deflected beam trajectories (see Figure 3.13a) did not coincide for different energies, but fanned out energy-dependently, as the

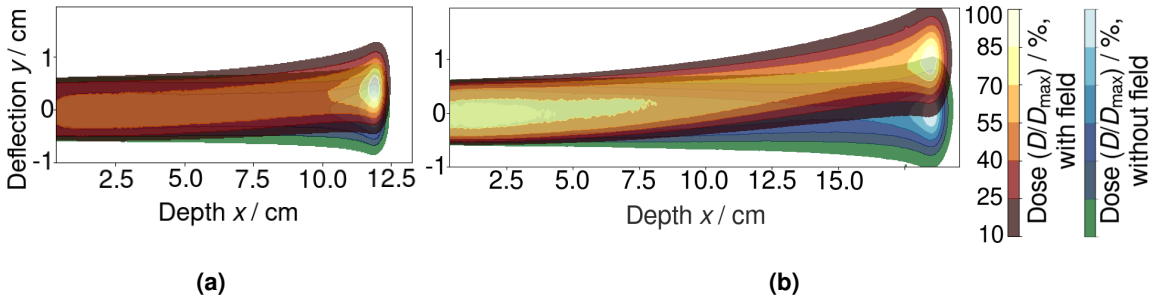

(a) (b)

Figure 3.12: Dose distribution relative to the maximum $D_{\max}$ of a 140 MeV (a) and a 180 MeV (b) proton beam in PMMA measured with the film dosimeter, without (bluescale) and with (redscale) magnetic field. Figure adapted from Schellhammer et al. (2018b).

radius of beam path increases with increasing proton energy (Wolf and Bortfeld, 2012). No magnetic-field induced change in the absolute measured dose was observed.

Comparison of simulation and experiment

The predicted and measured deflected central beam trajectories agreed within 0.8 mm for all studied beam energies (see Figure 3.13a). To quantify the accuracy of the calculated Bragg peak positions, their retraction and deflection were compared (see Figure 3.13b). The uncertainties of the measured and simulated Bragg peak displacement were within 0.5 mm and 0.3 mm, respectively (see Appendix A.3 and B.2). Predicted and measured Bragg peak retraction and deflection agreed within these uncertainties for all studied energies. There was no systematic difference in both quantities between the simulation and measurement data.

3.2.4 Discussion

The obtained range in Bragg peak displacement of 1 mm to 10 mm corresponds well with previous theoretical studies in a homogeneous magnetic field in water (Fuchs et al., 2017; Schellhammer and Hoffmann, 2017). Due to the LET-dependent dose saturation of EBT3 films, no direct dose comparison was made between measurements and Monte Carlo simulations. While this study aimed to quantify the accuracy of the predicted beam deflection and Bragg peak displacement (which was found to be affected by this saturation by 0.2 mm or less, see Appendix B.2), commissioning procedures of future MRiPT systems will need

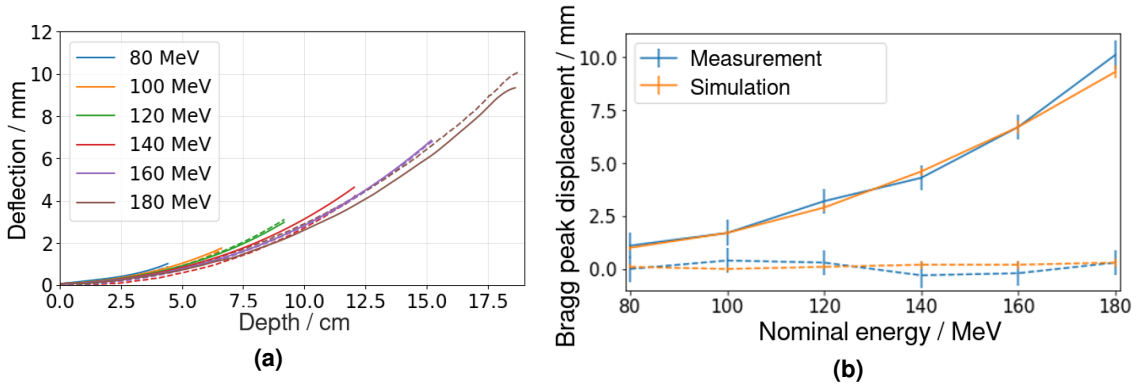

Figure 3.13: (a): Monte Carlo calculated (solid lines) and measured (dashed) deflected central beam trajectories. (b): Calculated and measured magnetic field-induced Bragg peak displacement in lateral (deflection, solid) and longitudinal (retraction, dashed) direction. Error bars refer to systematic and statistical uncertainties given in Tables A.1 and B.1. Individual data points are interconnected for visualisation only. Figure adapted from Schellhammer et al. (2018b)

to include extensive three-dimensional dose measurements corrected for such effects.

This study has been confined to a homogeneous medium. For inhomogeneous media, a magnetic field induced dose enhancement at medium-air material boundaries in the order of 2 % has been predicted for 250 MeV and 3 T caused by electrons returning to the material boundary after being deflected by Lorentz force in air (Fuchs et al., 2017; Lühr et al., 2018). For media other than PMMA, changes in stopping power affect the range and the local beam curvature and thus the displacement of the Bragg peak (Schellhammer and Hoffmann, 2017). Therefore, future measurements in inhomogeneous media are desirable. However, the conclusions drawn in this study are expected to be transferable to other tissue-like media, as the underlying particle interactions do not differ substantially.

Another limitation of this study is its confinement to beam energies up to 180 MeV and a magnetic flux density of 1 T. Follow-up studies may include a magnet assembly with a larger main field extension to allow for higher beam energies, or an electromagnet with adjustable flux density. This would enable the experimental verification of proton beam deflection for all therapeutically relevant energies and magnetic flux densities.

3.3 Summary

Although previous work has indicated that there is general consensus that the trajectory of a slowing down proton beam in a water phantom inside a transverse magnetic field is predictable, the quantitative comparison of the different methods presented in this chapter has shown that predictions of different models only agree for certain proton beam energies and magnetic flux densities. Therefore, shortcomings of previously published analytical methods have been analysed and quantified. The inclusion of critical assumptions and the lack of applicability to realistic, i.e. inhomogeneous, magnetic flux densities and patient anatomies have been identified as main problems. To overcome these deficiencies, a new model called RAMDIM has been developed and shown to be both less assumptive and applicable to more realistic setups than existing analytical approaches, and faster than Monte Carlo models.

Thus, RAMDIM is useful to get a fast and accurate estimate for the beam deflection and retraction that is to be expected in MRiPT, and for the correction parameters needed for a compensation thereof. It can help in the planning of experimental setups for dosimetric studies in MRiPT, and its simple structure helps to understand the underlying physical mechanisms. Furthermore, it can be used as reference solution when setting up a Monte Carlo model or an experimental study. As pointed out by Hartman et al. (2015), intensity-modulated MRiPT planning can be realised by two Monte Carlo calculation steps - one for selection of beamlets whose deflected Bragg peaks lie inside the target, and one for dose calculation. Thus, another possible application of RAMDIM is to replace the first Monte Carlo step in order to reduce the overall calculation time.

In a second step, the proton beam deflection has been measured for the first time in a tissue-mimicking medium by film dosimetry and compared against Monte Carlo simulations. It was experimentally shown in a transverse magnetic field of 0.95 T that the lateral Bragg peak displacement ranges between 1 mm and 10 mm for proton energies between 80 and 180 MeV in PMMA. Range retraction was found to be within 0.5 mm. The measured Bragg peak displacement was shown to agree within 0.8 mm with Monte Carlo based particle tracking simulations.

This work has shown that and how the magnetic field induced proton beam deflection and Bragg peak displacement are both measurable and accurately predictable in a tissue-like beam stopping medium. Within the given uncertainties and over the studied range of proton

energy and magnetic flux density, the presented verification of Monte Carlo based trajectory prediction justifies its use as a gold standard for treatment planning and to compare analytical and numerical models. As RAMDIM has been shown to cause the smallest deviations to Monte Carlo simulations, this underlines its applicability for the above mentioned purposes.

4 Integrated In-Beam MR System: Proof of Concept

MRiPT requires the operation of both a proton therapy system and an MR scanner in the presence of an electromagnetically contaminated environment produced by their respective electromagnetic fields. To date the integration of a proton therapy and an MR system has not been realised. Simulation studies exist, but do not cover the effect of simultaneous irradiation and MR imaging on the beam and MR image quality. Since the different electromagnetic fields of the proton facility and the MR scanner can be expected to interfere, an identification and quantification of these effects is required.

The aim of this work is to build the first integrated in-beam MR setup, to test the feasibility of simultaneous proton beam irradiation and MR imaging, and to assess the mutual effects on the beam and the MR images. For this purpose, an open MR scanner was placed in the isocentre of a horizontal fixed proton research beam line while accounting for radio-frequency (RF) interference and beam deflection (section 4.1). On this basis, the influence of the static and dynamic magnetic fields of the MR scanner on the beam profile as well as that of the magnetic fields of the proton facility on the B_0 homogeneity and MR image quality are quantified (section 4.2). Lastly, the possibility of MR-based range verification is tested in a simple setup (section 4.3). Sections 4.1.1 to 4.2.1 and 4.2.3 have been published in similar form by Schellhammer et al. (2018a).

4.1 Integration of a Low-Field MR Scanner and a Static Research Beamline

Both the MR and the proton therapy system generate static and dynamic magnetic fields as well as RF waves. Their characteristics are identified and discussed in the following.

4.1.1 Proton Therapy System

The proton beam was generated at the University Proton Therapy Dresden (UPTD) facility (Figure 4.1a) by an isochronous cyclotron (C230, Ion Beam Applications SA, Louvain-la-Neuve, Belgium). The cyclotron had a mass of 210 t and produced two main electromagnetic fields: (1) the static magnetic field ($B_{\mathrm{cyclo}} \leq 3.09\,\mathrm{T}$) keeping the protons in a spiral trajectory while being accelerated and (2) the RF wave of the acceleration voltage ($f_{\mathrm{cyclo}} = 106\,\mathrm{MHz}$). According to the vendor's specifications, the cyclotron had a resistive electromagnet with passive magnetic shielding that produced a magnetic fringe field of 75 µT at a distance of 8 m, i.e. at the isocentre of the experimental room (see below).

The beam travelled to the experimental room through a beam line, comprising a horizontal vacuum pipe, a series of magnets that can both deflect (dipole magnets, $B_{\mathrm{dipol}} \approx 2\,\mathrm{T}$) and shape (quadrupole magnets, $B_{\mathrm{quad}} \approx 0.5\,\mathrm{T}$) the beam, an energy selection system to modulate the beam energy between 70 and 230 MeV, and a beam exit window at the end of the horizontal beam line in the experimental room.The distance between the beam exit window and the closest upstream quadrupole magnets was 2.7 m, while the closest dipole magnet was at 6 m. The beam isocentre was 1.1 m downstream of the beam exit, 2.8 m downstream of the last beam line magnet, 8.2 m away from the cyclotron, and 18.6 m away from the gantry in the neighbouring treatment room (see Figure 4.1a).

After passing through the beam exit window, the beam was collimated by two cylindrical brass collimators of 3.3 cm thickness each having a circular shaped aperture of 10 mm diameter to reduce primary radiation exposure of the in-beam MR scanner (see section 4.1.2). In the neighbouring treatment room, a beam line mounted on a 360 degree rotatable isocentric gantry with a ferromagnetic mass of about 110 t and multiple dipole and quadrupole magnets was present. The magnetic field of the beam line is dynamic, as the beam line magnets are only energised when the beam is transported into one of the two rooms, and depends on the beam energy. The earth magnetic field at the facility was about 50 µT(National Centers for Environmental Information, 2018).

4.1.2 MR Scanner

An open low-field MR scanner was chosen for this study because, as compared to high-field MR scanners, it provides larger flexibility to transport the beam to the field-of-view (FOV) and position study objects and dosimetry equipment in the FOV, smaller suscep-

tibility artifacts, a lower specific absorption rate (SAR) allowing for real-time imaging and tumour tracking without flip angle restrictions, and lower costs (Hayashi et al., 2004; Simonetti and Ahmed, 2017). Although the signal-to-noise ratio of low-field scanners is lower than in high-field scanners, it is expected to be sufficient for anatomical imaging and organ motion tracking in radiation therapy (Fallone et al., 2009). Furthermore, on-board low-field MR imaging has been shown to outperform on-board computed tomography imaging in MRiXT regarding organ visibility (Noel et al., 2015).

The MR scanner comprised a C-shaped permanent magnet (MrJ2200, Paramed Medical Systems, Genova, Italy). It generated three different types of electromagnetic fields: a vertically upwards oriented static magnetic field ($B_0 = 0.22\,\mathrm{T}$), three pulse sequence-dependent, dynamic gradient fields for spatial encoding (typical gradient amplitude 0.5 mT/m $\leq G_{x,y,z} \leq$ 20 mT/m) and a pulsed RF wave for proton spin excitation at the Larmor resonance frequency ($B_1 \leq 30\,\mu\mathrm{T}$ and $f_{\mathrm{NMR}} = 9.49\,\mathrm{MHz}$) (Paramed S.r.l, 2010). The scanner was equipped with a set of six receive coils dedicated to different body regions (hand, knee, shoulder, hip, upper and lower spine). The scanner was designed for musculoskeletal imaging and was not capable of real-time imaging.

4.1.3 Potential Sources of Interference

Effects of the MR Scanner on the Proton Beam

Since the proton beam was directed perpendicularly to the magnetic field of the MR scanner, it was expected to experience the Lorentz force and thereby be deflected (see chapter 3). Since the main magnetic field B_0 was permanent (i.e. always on), it needed to be taken into account for positioning the scanner. On the other hand, both the pulsed RF wave and the dynamic gradient fields were small (up to 30 µT and 20 mT/m, respectively) in comparison and only present during MR image acquisition. Their influence on the beam was assessed by beam profile measurements.

Effects of the Proton Therapy System on the MR Image

An alteration in B_0 results in a Larmor frequency shift that can translate into an off-resonance voxel shift in the frequency and slice encoding directions of the MR image (see equations 2.8 to 2.10). For the used scanner, a difference in the B_0 field of $0.5\,\mu\mathrm{T} \leq \Delta B_0 \leq 20\,\mu\mathrm{T}$

can induce a voxel displacement of 1 mm, depending on the pulse sequence-dependent amplitude $G_{x,y,z}$ of the dynamic gradient fields (see equation 2.8). A spatially uniform perturbation of B_0 can cause a global uniform image shift, whereas a non-uniform perturbation can lead to local image deformations, which are harder to correct for than a global image shift. Magnetic fields that change during image acquisition can lead to non-linear image artefacts such as ghosting.

A change in B_0 can be induced in the proton therapy facility by changes in the status and current settings of the beam line magnets and in the position of the gantry in the neighbouring treatment room. Since the beam line magnets to the treatment room are always switched off during irradiation in the experimental room, these cannot interfere with in-beam MR imaging. However, perturbations in the environmental magnetic field due to rotation of the ferromagnetic gantry in the adjacent treatment room cannot be excluded a priori. Furthermore, energising the beam line magnets to the experimental room for irradiation can be expected to cause an alteration of B_0 due to the magnetic fringe field of the beam line. These effects were studied by characterising the B_0 magnetic field homogeneity and the MR image quality at different gantry angle positions, and with and without energised beam line magnets, respectively.

In addition to this, RF signals produced in the facility with a frequency interfering with f_{NMR} can appear as line or zipper artefact on the MR images. The conventional way to mitigate this, i.e. placing the MR scanner in a copper-shielded room, is not applicable here due to the size of the experimental room and the variety of technical equipment therein. A compact Faraday cage surrounding the MR scanner had therefore to be fabricated.

4.1.4 Integration of Both Systems

Beam Deflection: Alignment of MR Scanner and Beam Isocentre

The MR scanner was elevated to the level of the beam line (127 cm above floor level) using a trolley and initially placed such that its magnetic isocentre coincided with the beam isocentre.

To determine the lateral position of the scanner relative to the central beam axis, beam deflection in the horizontal plane needed to be taken into account. For this purpose, the central plane of its B_0 field was mapped with a high-linearity Hall probe (HHP-VU, Arepoc s.r.o., Bratislava, Slovak Republic) from the isocentre of the magnet up to a distance of

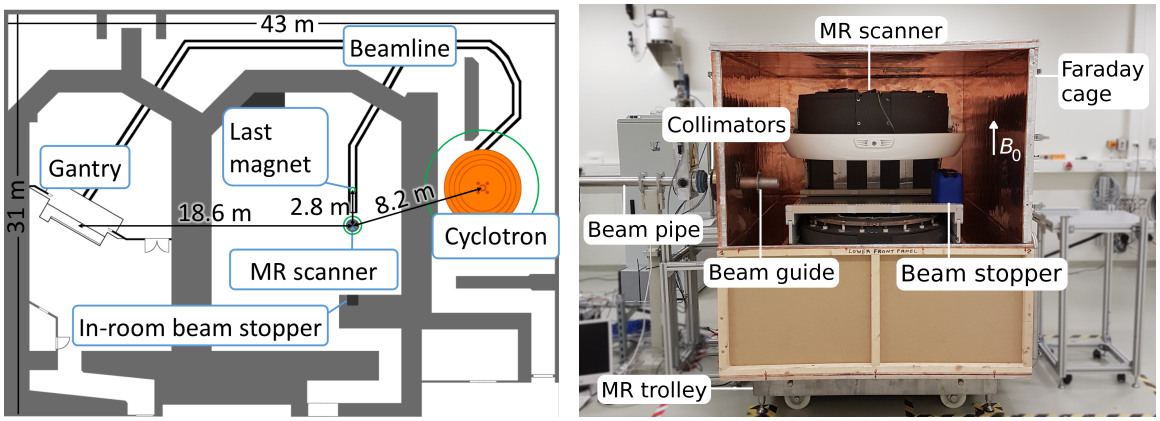

Figure 4.1: (a) Schematic floor plan of the UPTD proton therapy facility comprising a therapy room with rotating gantry (left) and an experimental room with a horizontal static research beam line (middle). The 5 G (0.5 mT) lines of the cyclotron, MR scanner and the last beam line magnet are indicated by green circles. (b) Experimental setup with horizontal static beam line and in-beam MR scanner (upper front panel of Faraday cage removed). Figure adapted from Schellhammer et al. (2018a).

±140 cm in steps of 5 cm (see Figure C.1 in Supporting Information). This field map was then used as input for Monte Carlo simulations (Geant4 toolkit version 10.2.p02, Agostinelli et al. (2003) and Allison et al. (2006)) to calculate the lateral beam deflection at the beam isocentre for beam energies between 70 and 230 MeV. A mean lateral beam deflection of 2 cm relative to the central beam axis was found at the isocentre, ranging between 2.4 cm and 1.3 cm for 70 MeV and 230 MeV, respectively. Thus, the MR scanner was moved by 2 cm from the central beam line axis in the direction of the beam deflection.

To verify that the beam was well within the FOV of the MR scanner, a water-filled cylindrical phantom of 10 cm length and 10 cm diameter (ACR Small MRI Phantom, Newmatic Medical, Grand Rapids, USA) was placed centrally in the FOV. A radiochromic film (Gafchromic EBT3, Ashland, USA) was affixed vertically to the front face of the phantom prior to irradiating it with a 125 MeV proton beam that was fully stopped inside the phantom. The dose distribution deposited on the film confirmed that the beam was centrally incident on the phantom, with a vertical and horizontal deviation from the phantom centre of 0.01 cm and 1.00 cm, respectively, and a spot size (1 sigma) of 5 mm.

RF Interference: Faraday Cage

The scanner was shielded from the RF sources of the facility, mainly the cyclotron accelerating high voltage, by a compact Faraday cage made of wood and 0.12 mm copper sheets (Ion Beam Applications SA, Louvain-la-Neuve, Belgium). The low-power RF attenuation of the cage was 75 dB at 9.5 MHz, as measured by Holland Shielding Systems BV (Dordrecht, The Netherlands). With the cage closed, external RF interference was therefore not expected to degrade the performance of the MR scanner or the proton therapy system.

To transport the beam to the FOV of the MR scanner, a cylindrical aluminium beam guide (20 cm length, 8 cm diameter) was installed into the wall of the cage at the point where the beam was incident on the wall. The beam guide protruded to both sides of the wall by 10 cm. No magnetic shielding was applied.

After installation, the magnet was mechanically shimmed to generate a homogeneous B_0 field by Paramed Medical Systems (Genova, Italy).

4.2 Beam and Image Quality in the Integrated Setup

The beam and MR image quality in the in-beam MR scanner are assessed in the following. For this purpose, firstly the beam deflection due to the static and gradient magnetic field of the MR scanner is quantified by beam profile measurements. Secondly, the magnetic field homogeneity of the scanner placed in the proton therapy facility is determined, and its dependence on the angular rotation of the gantry in the neighbouring treatment room is quantified. Thirdly, the image quality of MR images acquired of a healthy volunteer, a sarcoma patient, and a tissue phantom is assessed qualitatively. Lastly, MR image quality is quantified by a standardised imaging phantom with and without simultaneous proton beam irradiation.

4.2.1 Beam Profile

While the proton range is not expected to be affected by a 0.22 T magnetic field (see section 3), the Lorentz force can affect the lateral beam profile. Therefore, beam profiles were acquired behind the MR scanner to test whether the the in-room beam stopper at the wall opposite to the beam line was sufficient to absorb the deflected beam, and whether the magnetic gradient fields of the MR scanner affected the beam quality.

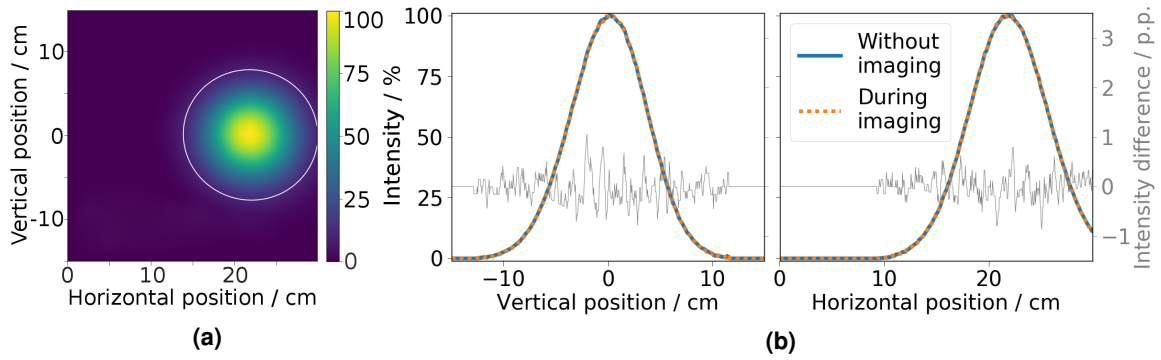

Figure 4.2: Transverse beam profile of a 72 MeV proton beam measured behind the MR scanner, normalised to the maximum intensity. (a): Two-dimensional profile. The 10 % isoline is marked in white as a point of orientation. (b) Vertical and horizontal central line profiles measured during acquisition of a coronal spin echo image (orange) and without simultaneous imaging (blue, left ordinate). The difference between the profile with and without simultaneous imaging is displayed in percentage points (grey, right ordinate). Figure adapted from Schellhammer et al. (2018a).

Material and Methods

Transverse beam profiles were acquired (with the top of the Faraday cage removed) with and without MR scanner in place for proton beams of three different energies (E_0 =72 MeV, 125 MeV and 219 MeV) using a pixelated scintillation detector (Lynx, IBA Dosimetry, Schwarzenbruck, Germany) positioned 110 cm downstream of the isocentre (i.e. at 220 cm downstream of the beam exit window). Bivariate Gaussian functions were fitted to the beam profiles to determine the beam centre and width (i.e. standard deviation) in both horizontal (i.e. parallel to the floor level) and vertical (i.e. parallel to gravity) direction.

To assess the effect of the dynamic gradient fields on the beam quality, the beam profile measurements were repeated for the most magnetic field-sensitive beam energy (i.e. 72 MeV) during acquisition of three sequences varying in pulse sequence technique and gradient orientation: a vertical (transverse) and a horizontal (coronal) spin echo image and a vertical gradient echo image (gradient amplitude 0.7 mT/m $\leq G_{x,y,z} \leq$ 6.1 mT/m). Difference images were acquired between beam profiles measured with and without simultaneous imaging (i.e. gradient fields) for all three sequences, and between three repeated beam profile measurements acquired without simultaneous MR imaging. Beam rotation was not assessed as this was only expected to occur in configurations where the B_0 field is oriented parallel to the beam (Oborn et al., 2015).

Results and Discussion

With the MR scanner in place, the beam showed a horizontal deflection of 22, 16 and 11 cm for 72, 125 and 219 MeV, respectively, and a vertical deflection below 0.6 mm relative to the central beam axis at 220 cm downstream of the beam exit. Therefore, the beam was expected to miss the in-room beam stopper in the opposite wall, which was another 6 m downstream of the measurement point. As a consequence, a water tank was installed as a mobile beam stopper at the distal end of the scanner.

No relevant difference was observed between the beam profiles acquired with and without image acquisition for all tested sequences (Figure 4.2). The beam centres and widths agreed within 0.02 mm for all image acquisitions relative to those acquired without simultaneous imaging. This suggests that the beam quality can be expected not to be deteriorated during MR image acquisition, and that treatment planning can be performed without taking into account the dynamic MR fields. However, positive and negative components of the G_x gradient of the MR scanner may have evened out along the beam path, such that future dose measurements in the FOV of the MR scanner are required to fully confirm this.

4.2.2 MR Magnetic Field Homogeneity

The static magnetic field of the proton therapy facility, which is governed by the fringe field of the cyclotron, may limit the achievable spatial homogeneity of the B_0 field of the MR scanner. Furthermore, the rotating ferromagnetic mass of the gantry in the neighbouring treatment room may affect both the spatial homogeneity and the absolute value of B_0, which can lead to image deformations and shifts, respectively. The homogeneity and absolute value of B_0 were therefore quantified at different gantry angles and during gantry rotation, and compared to the vendor's specifications.

Material and Methods

The magnetic field on a 22 cm diameter spherical volume (DSV) was mapped three times by a vertically rotatable magnetic field camera placed in the centre of the FOV (MFC3045/3048, Metrolab, Geneva, Switzerland). The camera comprised 16 individual NMR probes arranged in a semicircle at an angle θ (see Figure 4.3). The magnetic field at the position of a probe was measured by irradiating a range of radio-frequencies to the probe and de-

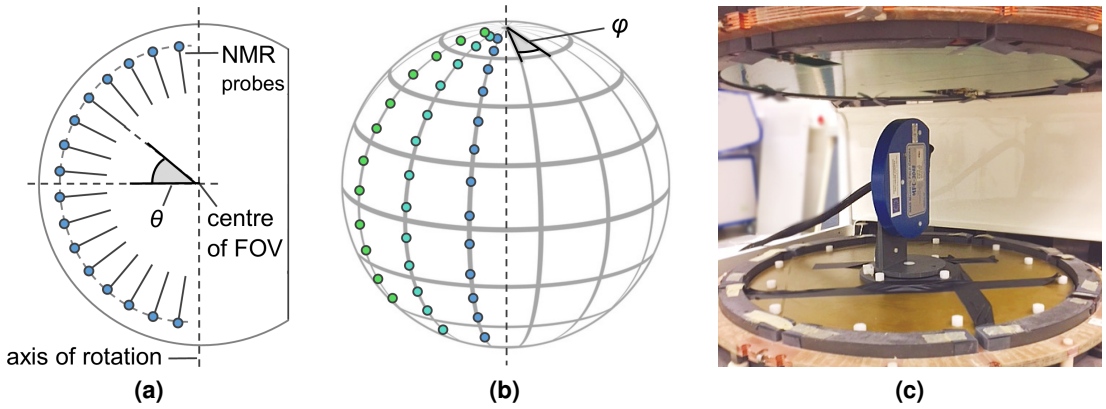

Figure 4.3: Magnetic field camera. (a) Schematic representation of the half-moon shaped camera with 16 individual NMR probes. (b) A 3D field map on a spherical surface is acquired by rotation of the camera. (c) Setup of the camera inside the FOV of the MR scanner.

tecting its Larmor frequency by resonance (METROLAB Instruments SA, 2004). By rotating the camera to 12 angular positions φ, a three-dimensional map of the magnetic field on a spherical surface of 22 cm diameter was acquired (see Figure 4.3b). The mean Larmor frequency and the peak-to-peak homogeneity, i.e the difference between the lowest and highest Larmor frequency on the sphere, were extracted. The gantry in the neighbouring room was at 0° during these measurements.

To quantify the influence of the gantry angle, this measurement was repeated three times each with three further static gantry positions (90°, 180°, 270°) and once during a full gantry rotation at low speed (1° per second) and high speed (6° per second) in clockwise and counter-clockwise direction, respectively (see Figure 4.4a). The measured frequencies were corrected for their temperature-dependent temporal drift with a linear function (Riemann, 2018).

Results and Discussion

The reference magnetic field homogeneity was 88 ppm relative to the mean Larmor frequency $\bar{f}_{\mathrm{NMR}} = 9.496\,19$ MHz (see Figure 4.4b). This homogeneity was within the vendor's specifications and therefore accepted. Differences between the three repeated measurement of $\bar{f}_{\mathrm{NMR}}$ and the homogeneity were smaller than 1 Hz and 1 ppm, respectively, indicating a high measurement reproducibility (see Figure 4.4a).

All differences in $\bar{f}_{\mathrm{NMR}}$ and the homogeneity for the different gantry angles and during

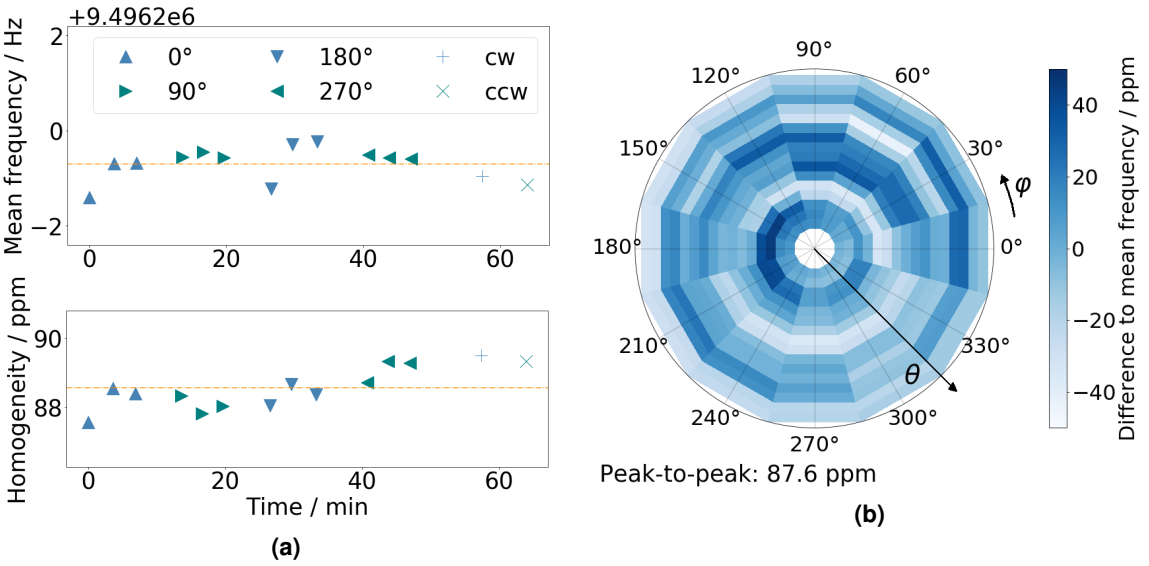

Figure 4.4: NMR frequencies measured by the magnetic field camera in a 22 cm diameter spherical volume in the FOV of the MR scanner. (a) Central frequency (top) and peak-to-peak magnetic field homogeneity (bottom) for different gantry angles and during clockwise (cw) and counter-clockwise (ccw) rotation. The average of the central frequency and homogeneity is depicted as orange dashed line. (b) Polar representation of the magnetic field map as measured at 16 probe angles θ and 12 rotation angles φ at a static gantry angle of 0°.

the gantry rotation were within 2 Hz and 2 ppm, respectively. With the gradient amplitudes of the MR scanner (0.5 mT/m $\leq G_{x,y,z} \leq$ 20 mT/m), the differences in $\bar{f}_{\mathrm{NMR}}$ and the homogeneity translate into pixel shifts below 0.1 mm and 1 µm, respectively (see equation 2.8), which is negligible for radiotherapy applications. This implies that MR imaging at the beamline in the experimental room is not affected by a rotation of the gantry in the neighbouring treatment room. Therefore, in-beam MR images can be acquired with the in-beam MR scanner regardless of the patient treatment-dependent gantry position. However, it is noted that irradiation in the experimental room is technically not possible when the beam line magnets to the treatment room are energised, such that activities in the treatment room cannot fully be neglected during experiments being performed with the in-beam MR scanner in the experimental room.

4.2.3 MR Image Quality - Qualitative In Vivo and Ex Vivo Test

As a first test of the MR image quality of the in-beam MR system, images were acquired of a healthy volunteer, a sarcoma patient and a sausage phantom, and evaluated qualitatively.

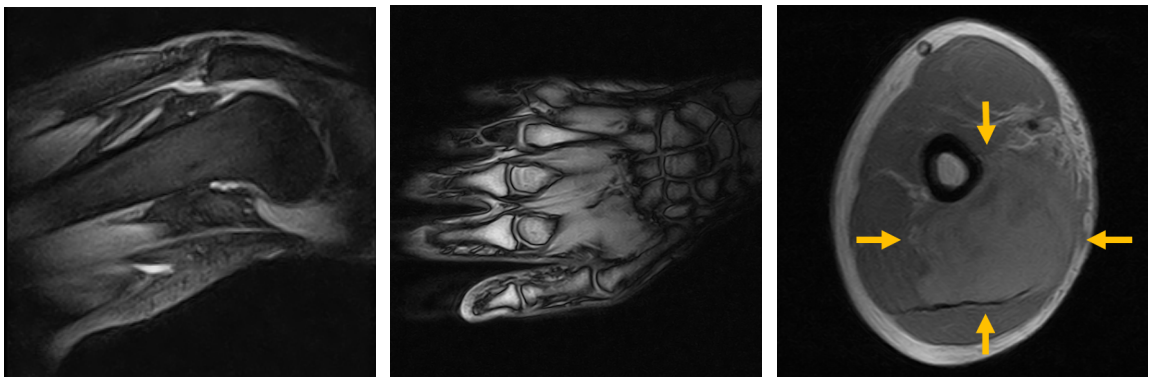

(a) (b) (c)

Figure 4.5: MR images acquired with the beam line to the MR system switched off. (a) STIR gradient echo image of a knee, (b) T_1-weighted gradient echo image of a hand palm, and (c) T_1-weighted spin echo image of an upper arm, with a soft-tissue sarcoma marked by arrows. Figure adapted from Schellhammer et al. (2018a).

Material and Methods

Since the MR scanner was mainly designed for musculoskeletal images of the extremities, the initial test consisted of images of the knee and hand palm of a healthy volunteer and of a soft-tissue sarcoma of the right upper arm of a patient. Common pulse sequences for extremities were used: a short inversion-time inversion recovery (STIR) gradient echo image of the knee, a T_1-weighted gradient echo image of the hand palm, and a T_1-weighted spin echo image of the sarcoma (see Table C.2 for sequence parameters). For these three scans, the knee, hand and knee coil were used, respectively. The observed image quality was rated qualitatively by a radiation oncologist with expertise in treating extremity soft tissue sarcoma. For safety reasons, these scans were performed while the beam line in the experimental room was switched off.

To assess the effect of the beam line magnets and the proton beam on the MR images, a mixed sausage phantom was placed in the knee coil of the MR scanner. MR images were acquired under three scenarios: (a) without beam, (b) with energised beam line magnets and (c) during irradiation at a high proton current and energy (5 nA and 215 MeV, respectively). A T_1-weighted spin echo sequence was used as it represents a commonly used pulse sequence. To ensure that MR imaging in (b) was started after the current energising the beam line magnets had reached a stable level, the environmental magnetic field in the experimental room was monitored using a fluxgate magnetometer (TFM1186, Metrolab,

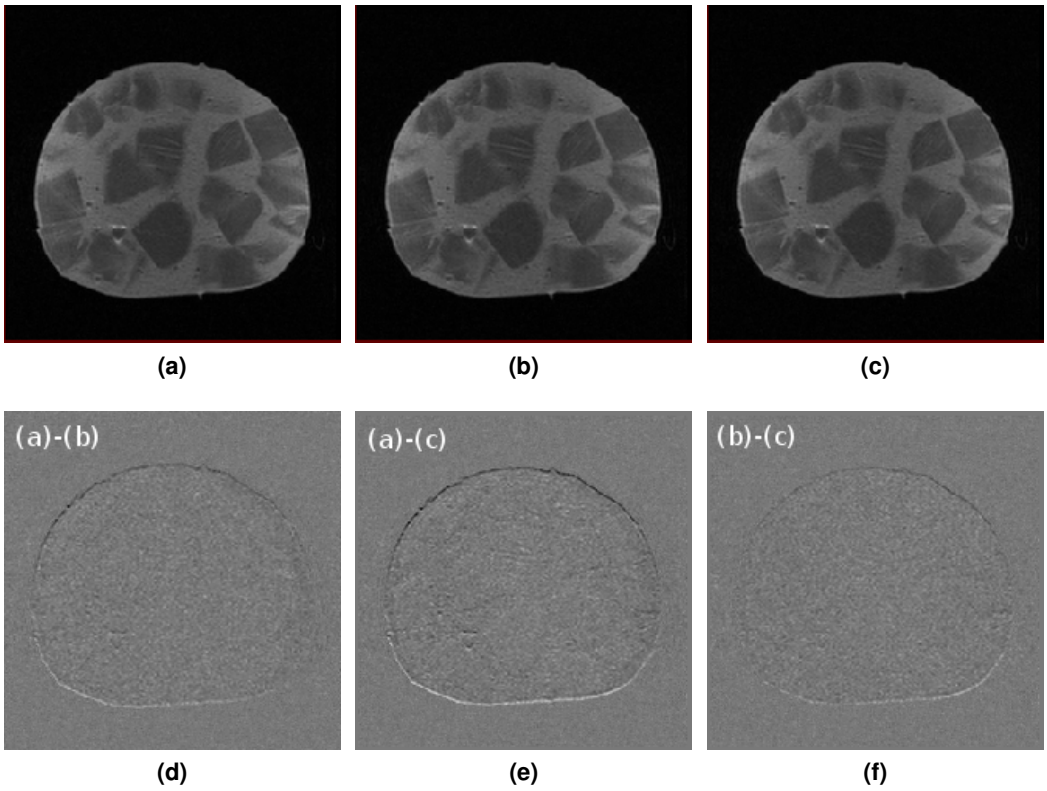

Figure 4.6: T_1-weighted spin echo image of a mixed sausage without beam (a), with energised beam line magnets (b) and during proton irradiation at 215 MeV and 5 nA (c). Difference images (d-f) show a submillimetre uniform shift in (vertical) frequency-encoding direction. Figure adapted from Schellhammer et al. (2018a).

Geneva, Switzerland). The measured time delay between switching on the magnets and the magnetic field change was less than ten seconds.

Results and Discussion

The anatomical images showed the expected image quality for a 0.22 T musculoskeletal MR scanner and enabled the discrimination of relevant anatomical structures, i.e., muscles, tendons, vessels, fat, bone, and tumour (Figure 4.5). The observed image quality was rated to be sufficient for target volume definition and positioning by the radiation oncologist. The acquisition times ranged between 4 and 5.5 minutes.

In the images of the sausage phantom (see Figures 4.6a-c), no visible beam influence or image deformation was detected. However, a submillimetre, spatially uniform shift of

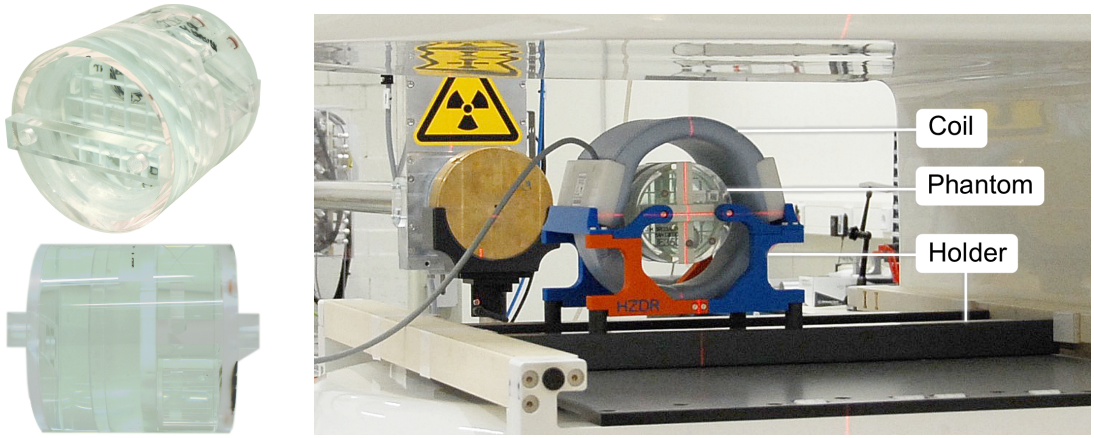

(a) (b)

Figure 4.7: ACR Small Phantom. (a) Front and side view. (b) The phantom placed inside the knee coil, the holder and the MR scanner in front of the beam exit.

the phantom in frequency-encoding direction was observed in the difference images (see Figures 4.6d-f).

These results show that simultaneous imaging and irradiation with a static beam is possible with the in-beam MR scanner without major image distortion. The image shift can most likely either be explained by statistical fluctuations in the pre-scan frequency calibration of the MR scanner, or by alterations in the Larmor frequency due to the fringe field of the beam line magnets. Therefore, a systematic analysis of the MR image quality, especially of image shifts, is required.

4.2.4 MR Image Quality - Quantitative Phantom Tests

To analyse the image quality of the in-beam MR scanner and its behaviour under simultaneous irradiation with energised beam line magnets, a multi-parameter study was performed by adapting a standardised MR quality assurance protocol.

Material and Methods

Phantom

The American College of Radiology (ACR, Reston, USA) has established phantoms and guidelines for standardised MR image quality assurance (American College of Radiology,

Table 4.1: MR sequence parameters for the image quality tests. Parameters marked with a cross ($^+$) deviate from the ACR protocol due to limitations of the MR scanner. The GE sequences were added to the ACR protocol for this study.

Sequence	Locator	T_1 SE	T_2 DE SE	T_1 GE	T_2^* GE
FOV diameter / cm	12	12	12	12	12
Number of slices	1	7	7	7	7
Interslice space / mm	-	3	3	3	3
Slice thickness / mm	10^+	5	5	5	5
Matrix size	(192,152)	(192,152)	(192,152)	(192,152)	(192,152)
Number of excitations	1	1	1	1	1
Echo time / ms	20	20	28^+,93^+	8	30
Repetition time / ms	200	500	2000	30	80
Flip angle / °	90	90	90	20	20
Acquisition time (min:s)	0:35	1:21	3:01	1:10	1:52

2017). The image quality of the in-beam MR scanner was studied following these guidelines, and using the ACR Small Phantom (see Figure 4.7a). This phantom is a hollow cylinder of PMMA equipped with a number of contrast structures enabling the quantitative analysis of different image quality parameters. It consists of acrylic plastic and is filled with a water-based solution containing 10 mM nickel chloride and 0.45 mass percent aqueous sodium chloride to mimic tissue-like magnetic susceptibility, electrical conductivity and relaxation times. The inner length and diameter are 100 mm.

The phantom was used in combination with the knee coil of the MR scanner (see Figure 4.7b). Both were placed in an in-house designed, dedicated holder ensuring a reproducible positioning in the centre of the FOV of the scanner. PMMA plates were affixed to the upper and lower front of the phantom to generate a flat entrance surface for the proton beam.

MR sequences

Following the ACR Small Phantom protocol (American College of Radiology, 2017), a sagittal locator scan and a set of seven axial T_1- and T_2-weighted spin echo (SE) images were acquired for each measurement (see Table 4.1). Since gradient echo (GE) sequences are commonly used for real-time imaging and more sensitive to magnetic field inhomogeneities than SE sequences, two GE sequences were added to the protocol, with seven axial slices each: first, a fast T_1-weighted GE sequence using the shortest possible repetition time of the MR scanner, and second, a magnetic field-sensitive T_2^*-weighted GE sequence using the highest possible echo time. A subsequent acquisition of the locator

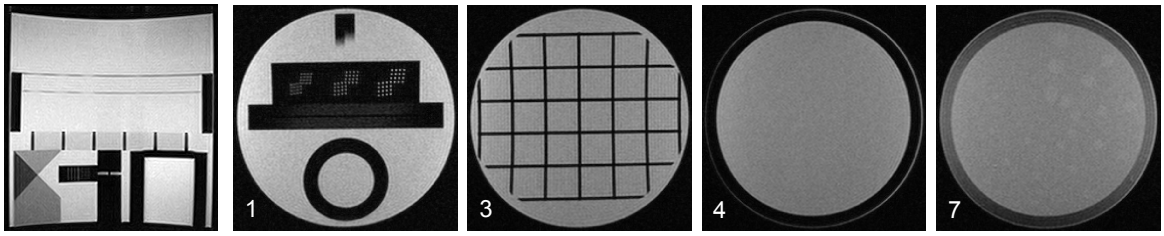

Figure 4.8: MR images of the ACR Small Phantom used for image quality analysis. (a): Sagittal locator. (b)-(e): Axial slices, with slice number in the bottom left. The shown examples are T_1-weighted.

and the four SE and GE sequences is called 'imaging set' in the following.

Imaging and irradiation

To separate statistical fluctuations from systematic differences in the image quality, 24 imaging sets were acquired each with (a) the beam line magnets switched off and (b) during simultaneous proton beam irradiation. Image sets with and without irradiation were acquired alternately to minimise the influence of possible temporal dependencies which could be caused for example by the temperature-dependence of the permanent magnet material.

The proton beam energy (125 MeV) was chosen such that the beam traversed all axial imaging planes and stopped at the distal region of the phantom behind the last imaging plane. This energy was calculated by a simple Geant4 Monte Carlo simulation of monoenergetic, parallel proton pencil beams of different energies through a simplified phantom without inner structure. The beam current was set to the maximum (5.4 nA at the beam exit) to obtain a worst-case estimate of any beam-related effects. Since the gantry position did not affect the magnetic field inside the FOV of the MR scanner (see section 4.2.2), it was not taken into account during this experiment. All images were acquired with the beam line to the treatment room switched off.

Before each imaging set, a calibration of the transmission RF frequency f_0 was performed by determining f_0 from the maximum of the frequency distribution as measured from an FID signal, and a scout scan, i.e. a set of three orthogonal SE localiser images, was acquired with the beam line switched off. On the scout scan, the position of the imaging slices in the phantom was visually verified according to the ACR protocol.

Image analysis

Image parameters were evaluated semi-automatically using the in-house developed and internally validated AMRIQA software tool (Czernohorsky, 2016). A detailed description of the image parameter acquisition from the image slices 1-7 (see Figure 4.8) can be found in literature (Davids et al., 2014; Czernohorsky, 2016; Dünger, 2017) and in the ACR Small Phantom protocol (American College of Radiology, 2017). A summary is given below.

The geometric accuracy of the images was tested by comparing the phantom diameter in image slices 1 and 3 and the phantom length in the localiser image to their known value. The horizontal and vertical spatial resolution were determined by the size of the smallest of three array structures that could be distinguished in slice 1. The ghosting ratio was deduced from the difference between the signal of elliptical regions next to the phantom in phase and frequency encoding direction on slice 4. The image uniformity was defined as the percentual difference between the brightest and darkest 1 cm^2 region in the fluid in slice 4. The slice position was determined from the length difference of two crossing wedges in slice 1. The low contrast object detectability was determined as the combined number of detectable low-contrast spokes in slices 6 and 7, and the slice thickness was determined from the length of two horizontal bars in slice 1 produced by crossing tilted capillaries.

In addition to these ACR criteria, the signal-to-noise ratio (SNR) was deduced from the mean phantom fluid signal and the standard deviation of the signal in a region outside of the phantom (Dünger, 2017).

Since a uniform phantom shift was detected in the preceding study (see section 4.2.3), the position of the centre of the phantom in both frequency and phase encoding direction was analysed as additional parameter. These parameters were added to the software for this study by implementing a circular Hough transform (Duda and Hart, 1972) in slice 4. This transform replaced the originally implemented fit procedure of two half circles to the phantom outline, which was shown to be less effective (see Figure 4.9a).

The automated analysis was supervised visually to detect any implausible results. Two parameters, the slice thickness and the low-contrast detectability, were found to be not reliably quantified by the software due to the low SNR of the MR images. These were therefore evaluated manually according to the ACR Small Phantom protocol (American College of Radiology, 2017).

The median and interquartile range of all 13 image quality parameters and 5 sequences were calculated for the images acquired with and without simultaneous irradiation. As a first

external reference, these results were compared to the ACR criteria. It should be noted, however, that these criteria were designed for diagnostic applications, which typically use high-field ($\geq$ 1.5 T) scanners with a strongly increased SNR in comparison to a 0.22 T scanner. No dedicated criteria exist for low-field musculoskeletal scanners and radiotherapy applications.

To compare the images acquired with and without simultaneous irradiation, the medians and interquartile ranges of all image quality parameters were calculated for both scenarios. To test the hypothesis that the image quality with and without simultaneous irradiation was equivalent, an equivalence test (Walker and Nowacki, 2011) was applied for all image quality parameters and sequences. Since no criteria have been established so far, the equivalence margins were based on the phantom- and image-specific discretisation: one pixel width for the geometrical parameters (i.e. 0.47 mm along phase and frequency encoding direction and 5 mm along slice encoding direction), one spoke for the low-contrast object detectability, 0.1 mm for the resolution, and 10 % of the median for the SNR, image uniformity, and ghosting ratio. As the statistical analysis of this amount of parameters ($12 \times 4 + 1 = 49$) would yield an unacceptable amount of random false-positives, a Bonferroni-Holm correction (Holm, 1979) was applied to achieve a family-wise false positive error rate of $\alpha = 5\,\%$. An image quality parameter was considered equivalent if the corresponding equivalence test was significant. Otherwise, the statistical difference in the parameter was tested by an inferiority t-test with a significance level of $\alpha = 5\,\%$. Since the parameter distributions were monomodal and fairly symmetric, a normal distribution was assumed for the statistical tests.

Results and Discussion

All measured image quality parameters are given in Tables C.3 to C.7 in the Supplementary Information section and will be summarised in the following.

ACR image quality with the beam line switched off

The geometrical image quality parameters showed very good agreement with the ACR criteria. The geometric accuracy, spatial resolution, slice position, and spatial resolution tests were passed by all four axial sequences, and the sagittal geometric accuracy test was passed by the sagittal locator sequence.

As common for low-field MR scanners, the median SNR of the MR images was low,

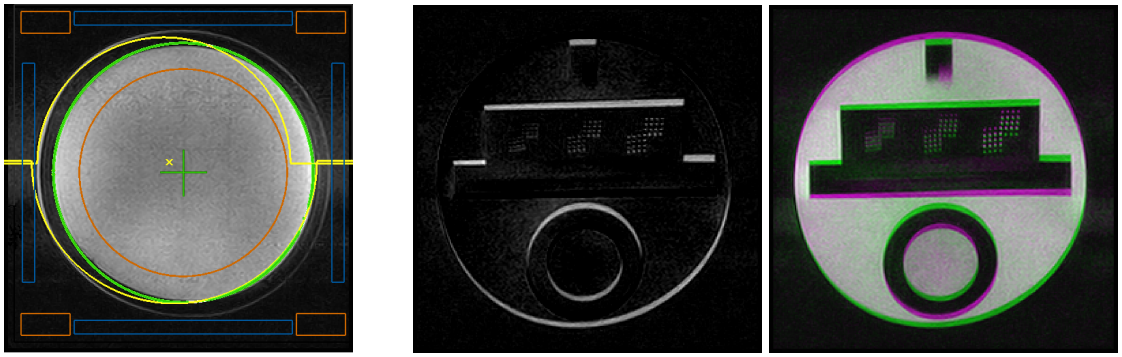

(a) (b) (c)

Figure 4.9: (a) Image analysis on slice 4. Regions used for the SNR test (orange), the ghosting test (blue), and the phantom centre determination (crosses) using the originally implemented fitting procedure (yellow) and the newly added Hough transform (green) to detect the phantom contour. (b-c) Example for the observed image shift along the vertical (frequency-encoding) direction between two subsequently acquired T_2^*-weighted GE images in slice 1. (b) is a difference image between the two images and (c) is a composite image showing the two images overlaid in complementary color bands (green and magenta).

especially for the T_1-weighted GE sequence (46, 48, 14 and 52 for the T_1- and T_2-weighted SE and the T_1- and T_2^*-weighted GE sequences, respectively). This resulted in a low image uniformity, a high ghosting ratio, and a small low-contrast object detectability in comparison to the ACR test criteria. Consequently, the image uniformity test was failed by all sequences. The ghosting test was failed by all sequences except for the T_1-weighted GE sequence. The low-contrast detectability test was failed by the GE sequences and only partly passed by the SE sequences. As signal noise obscured the slice thickness test bars, the test was failed by the T_1 SE and T_2^* GE sequences and was not performable for the T_1- weighted GE sequence. This test was only passed by the T_2-weighted SE sequence.

Phantom position with the beam line switched off

The median position of the phantom centre agreed between the four SE and GE sequences within 0.3 mm. However, the variability of the phantom centre showed a sequence-dependence in vertical (frequency-encoding) direction, with an interquartile range increasing from 0.5 to 1.5 mm, and a maximum deviation increasing from 1.0 to 3.5 mm (see Figure 4.10 and 4.9). The spread increased with increasing gradient amplitude G_x of the sequences, which was 2.6 mT/m, 1.5 mT/m, 5.7 mT/m and 0.7 mT/m for the T_1- and T_2-weighted SE and the T_1- and T_2^*-weighted GE sequences, respectively, according to the

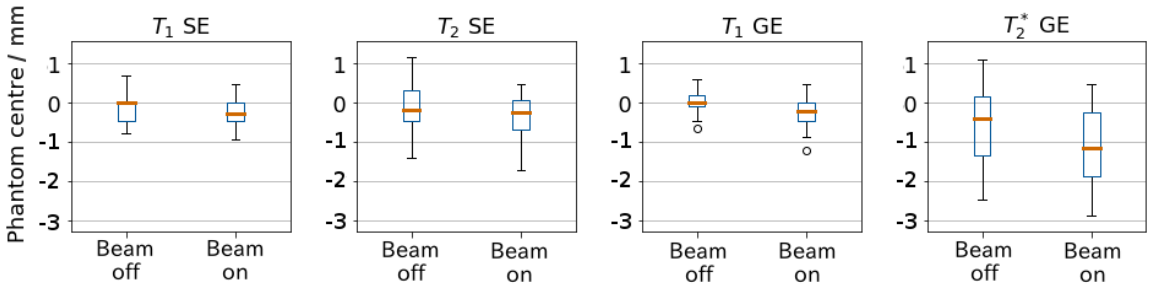

Figure 4.10: Measured positions of the phantom centre relative to the centre of the FOV in the (vertical) frequency-encoding direction in MR images for different sequences, acquired with and without simultaneous irradiation.

manufacturer.

This effect can be understood by fluctuations in the pre-scan frequency calibration, which are in the order of 50 Hz, according to the manufacturer. An error in the resonance frequency Δf results in a spatial off-resonance misencoding of (see equation 2.8)

$$\Delta x = \frac{2\pi\Delta f}{\gamma G_x} \tag{4.1}$$

in the frequency-encoding direction. Thus, a frequency fluctuation in the order of 50 Hz leads to image shifts in the order of 1.7 mm for $G_x = 0.7$ mT/m. This has to be taken into account for image-guided proton therapy, since an alignment of the isocentres of the proton beam and the MR scanner has to be ensured.

The phase-encoding direction of an MR image is not affected by uniform frequency shifts (see equation 2.9). Accordingly, the variability was smaller in the horizontal direction and no sequence-dependence was observed (see Figure 4.11). The interquartile range was between 0.4 and 0.5 mm (i.e. one pixel) for all sequences.

Image quality during irradiation

For most image quality parameters, the results were statistically equivalent with and without simultaneous irradiation, and no relevant median differences were observed (see Tables C.3 to C.6). Four exceptions were not statistically equivalent for all sequences and are discussed in the following.

The vertical position of the phantom centre showed a sequence-dependent median shift Δx into the negative direction of up to 0.7 mm for the T_2^*-weighted GE sequence (see Table C.6 and Figure 4.9). The same trend was observed for all sequences. The inferiority

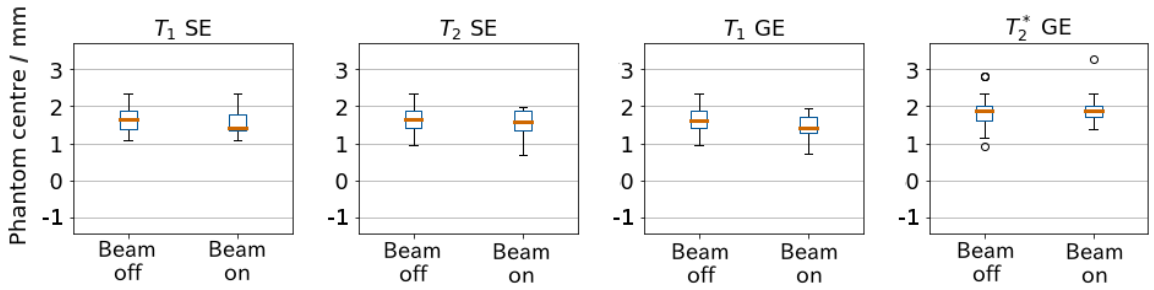

Figure 4.11: Measured positions of the phantom centre relative to the centre of the FOV in the (horizontal) phase-encoding direction in MR images for different sequences, acquired with and without simultaneous irradiation.

test showed that the reduction of the vertical phantom position with and without simultaneous irradiation was significant for the T_1-weighted SE and the T_1- and T_2^*-weighted GE sequences (with $p = 0.04$, $p = 0.01$ and $p = 0.04$, respectively).

This indicates that a frequency shift in the order of 20 Hz was induced by the beam line magnets, corresponding to a change of the magnetic field of about 0.5 µT (see equation 4.1). This effect has recently been confirmed in magnetometry measurements (Riemann, 2018) and may possibly be counterbalanced by performing the pre-scan frequency calibration while the beam line magnets are already energised.

Since the slice encoding gradient amplitude G_z was higher than G_x of the T_2^*-weighted GE sequence ($\geq$ 4.2 mT/m for all sequences), this direction, represented by the slice position parameter, was less sensitive to magnetic field changes and showed no relevant difference in images acquired with and without simultaneous irradiation (median differences were $\leq$ 0.2 mm). The phase-encoding direction is not affected by uniform magnetic field changes (see equation 2.9) and therefore showed no relevant changes ($\leq$ 0.2 mm). Its median position showed a systematic deviation of 1.5 mm from the centre of the FOV, which can be attributed to imperfections in the phantom holder design.

The SNR was the second parameter which was not statistically equivalent for all sequences, with a median difference of up to 1.5 for the T_2^*-weighted GE sequence (see Table C.6). A decrease of SNR was observed for all sequences during proton irradiation. This decrease was statistically significant for the T_1- and T_2-weighted SE and the T_2^*-weighted GE sequences (with $p = 0.01$, $p = 0.01$ and $p = 0.02$, respectively). This effect is consistent with a beam line-induced resonance frequency gradient, which leads to an imperfect slice excitation and therefore a reduced RF signal picked up by the receiver coils, and is

therefore expected to also be compensable by performing the pre-scan frequency calibration with energised beam line magnets. Another possible cause may be electronical noise induced in the receiver coils by the beam.

Furthermore, the phantom diameter in slice 1 of the T_2^*-weighted GE sequence showed no statistical equivalence. Here, no consistent trend was observed between the sequences. A high fluctuation was observed as compared to the other sequences, and consequently the inferiority test was not significant. This can be understood from geometrical distortions due to magnetic field inhomogeneities, which deformed the phantom from its circular shape inducing uncertainties to the Hough transform (see Figure 4.9). Since this effect was specific to the T_2^*-weighted GE sequence, which applied the lowest gradient amplitude, this indicates that the range of applicable MR sequences is limited in the context of the environmental magnetic field of the proton facility.

The ghosting ratio showed no statistical equivalence for three of the four sequences. No consistent trend was observed between the sequences, but a high fluctuation as compared to the median. The inferiority test was not significant. This indicates that the fluctuations in the ghosting ratio were higher than the statistical analysis allowed. Future studies are necessary to understand this effect in detail.

The gradient amplitudes applied by the used MR scanner were small compared to those used in most common MR scanners. It is expected that sequences with larger gradient amplitudes, and correspondingly high receiver bandwidths, will be more robust against magnetic field perturbations induced by the proton therapy facility, as voxel displacement is inversely proportional to gradient amplitude (see equation 2.8).

This setup did not comprise a beam line with a nozzle for pencil beam scanning, and the influence of the scanning magnets therein is expected to be larger than that of the beam line magnets, since the former are closer to the beam isocentre and have less steeply decreasing fringe fields. It is therefore mandatory to address this influence in future studies. Initial work on this issue has been commenced by Riemann (2018).

4.3 Feasibility of MRI-based Range Verification

The combination of anatomical imaging and proton range verification based on the same device appears desirable, and the developed in-beam MR setup allowed for a first exploratory feasibility test. This study therefore aimed to provide a qualitative proof of concept for MR-based range verification in a setup of low complexity.

4.3.1 MR Sequences

Material and Methods

A cylindrical plastic bottle filled with deionised water was used as a phantom. The bottle had a diameter of 9.4 cm and a length of 15 cm. A high proton energy was selected to allow for a high proton current ($E_{\mathrm{nom}} = 200$ MeV, corresponding to an energy at the beam exit of $E_0 = 201.9$ MeV, see section 3.2). The beam collimator was removed and a proton current of 9 nA was applied, which approximately corresponded to twice the maximum current used for clinical pencil beam scanning (Farr et al., 2008). A PMMA slab of 17.1 cm thickness was placed at about 40 cm in front of the phantom to stop the beam inside the phantom at a residual range of approximately 6.4 cm. This range was estimated by (Zhang and Newhauser, 2009)

$$R_{\mathrm{res,H_2O}} = R_{\mathrm{H_2O}}(E_0) - \frac{(S/\rho)_{\mathrm{air}} \cdot \rho_{\mathrm{air}}}{(S/\rho)_{\mathrm{H_2O}} \cdot \rho_{\mathrm{H_2O}}} \cdot d_{\mathrm{air}} - \frac{(S/\rho)_{\mathrm{PMMA}} \cdot \rho_{\mathrm{PMMA}}}{(S/\rho)_{\mathrm{H_2O}} \cdot \rho_{\mathrm{H_2O}}} \cdot d_{\mathrm{PMMA}} \,. \tag{4.2}$$

Tabulated stopping-power data (Berger et al., 2005) was used for the initial proton range in water $R_{\mathrm{H_2O}}$ and the material-specific mass stopping-powers $(S/\rho)_{\mathrm{material}}$. The thickness of the wall of the bottle was 0.1 cm, yielding an overall PMMA thickness of $d_{\mathrm{PMMA}} =$ 17.2 cm. The combined thickness of the air between the beam exit window, the PMMA slab and the phantom was $d_{\mathrm{air}} = 83.8$ cm. The densities of PMMA, air and water were estimated as $\rho_{\mathrm{PMMA}} = 1.19$ g cm^{-3}, $\rho_{\mathrm{air}} = 0.001$ g /cm^{-3} and $\rho_{\mathrm{H_2O}} = 1.00$ g /cm^{-3}, respectively. The overall uncertainty of the residual range in the phantom due to these approximations and setup uncertainties was estimated to be about 3 mm.

Six different basic MR sequences were used, which differed in image contrast and acquisition technique: two SE sequences (one T_1-weighted and one T_2-weighted), two GE

sequences (proton density (PD) and T_2^*-weighted), and two inversion recovery (IR) sequences (IRSE and IRGE). The sequence parameters are given in Table 4.2.

All image acquisitions, including the pre-scan frequency calibration and scout acquisition, were performed with energised beam line magnets in order to take into account their fringe field-induced perturbation in B_0. For each sequence, a reference image was first acquired without beam. For the second image, proton beam irradiation and MR imaging were started at the same time, and irradiation was stopped immediately after the end of image acquisition. The two images were compared visually to detect any beam-induced effects. Three further images were acquired immediately after irradiation was stopped to detect residual effects after irradiation.

The sequences were set up to acquire a single horizontal slice (i.e. parallel to the floor level) in the central plane of the beam. The position of this plane in the coordinate system of the MR scanner was determined as follows. A transversal EBT3 film was attached to the front face of the phantom placed in the MR scanner, and the phantom and film were irradiated by the proton beam (at 200 MeV and 0.136 nA for 60 s). The central plane of the beam, as visible on the film, was marked by attaching two spherical MR-markers of 6 mm diameter (PinPoint, Beekley Medical, Bristol, USA) to both sides of the beam spot. A T_1-weighted SE sequence was acquired comprising five horizontal slices of 5 mm thickness with an interslice spacing of 1 mm. The two markers were only visible in one of these slices. This slice position was therefore saved and chosen for all subsequent sequences. The overall uncertainty of the slice position was estimated to about 4 mm.

The mean dose measured on the film dosimeter in a circular region of 1 cm diameter around the beam centre was 4 Gy. Assuming that the dose rate scales linearly with the proton beam current, the dose rate in the plateau region was about 30 Gy/min per nA for the setup, i.e. 270 Gy/min for 9 nA. The spot size (full-width half maximum) was determined by fitting a two-dimensional Gaussian distribution to the film optical density and was 2.7 cm in both directions.

Results

A beam-induced effect was clearly visible in the GE and IRGE sequences (see Figure 4.12). Without simultaneous irradiation, the GE sequences showed a hyperintense central vertical line. During irradiation, this straight line developed a lightning-shaped curvature

Table 4.2: MR sequence parameters for the range verification tests. The cumulative dose applied during the sequences was calculated as the product of the acquisition time and the proton beam dose rate at a proton beam current of 1 nA.

Sequence	T_1 SE	T_2 DE SE	PDGE	T_2^* GE	IRGE	IR SE
FOV diameter / cm	18	18	18	18	18	18
Number of slices	1	1	1	1	1	1
Slice thickness / mm	5	5	5	5	5	5
Matrix size	(192,152)	(192,152)	(192,152)	(192,152)	(192,152)	(192,152)
Number of excitations	1	1	1	1	1	1
Echo time / ms	20	28, 93	8	30	8	20
Repetition time / ms	500	2000	200	80	200	500
Inversion time / ms	-	-	-	-	150	75
Flip angle / º	90	90	90	90	90	90
Acquisition time (min:s)	1:21	2:53	0:36	0:18	0:35	1:21
Cumulative dose / Gy	41	87	18	9	18	41

with a maximum amplitude at the expected proton range, especially in the PD-weighted GE sequence (see Figure 4.12c). In the IRGE image acquired during irradiation, a hypointense region in the shape of a proton beam dose distribution was clearly visible (see Figure 4.12e). The SE sequences showed small to no beam-induced signal alterations. As the PD-weighted GE and the IRGE sequence showed the strongest beam-induced effect, these were studied in more detail in the following.

In the three images acquired directly after irradiation, a decreasing beam-induced signal was observed. The third image acquired after irradiation was visually indistinguishable from the image acquired before irradiation. Hence, the beam-induced effect was reversible and faded with a time constant in the order of tens of seconds after irradiation.

4.3.2 Proton Beam Parameters

Material and Methods

To test whether the beam-induced signal depended on the proton current, the above experiment was repeated for the PD-weighted GE and the IRGE sequence at five different beam currents. The currents were 1 nA, 3 nA, 9 nA, 27 nA, and the maximum current (43 nA).

To study the range-dependence of the effect, the proton range in the phantom was varied in a second step by changing the proton energy (at a fixed proton current of 9 nA). The proton energies E_{nom} were 190 MeV, 200 MeV, 210 MeV and 225 MeV. The residual proton

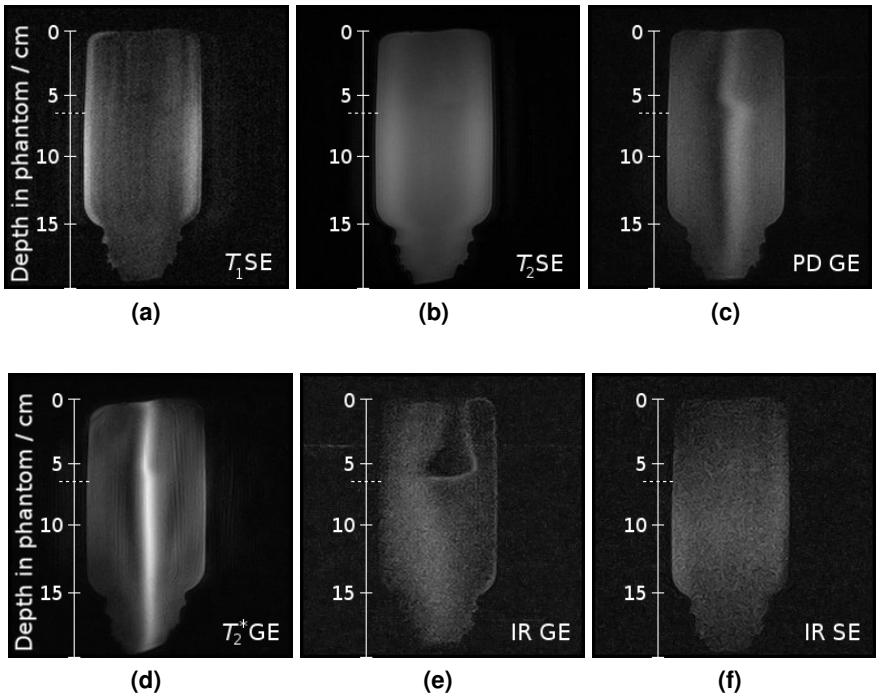

Figure 4.12: MR images for different sequences acquired during proton beam irradiation (200 MeV, 9 nA). (a) T_1-weighted SE, (b) T_2-weighted SE, (c) proton density-weighted GE, (d) T_2^*-weighted GE, (e) IR SE, and (f) IR GE sequence. The expected range in the phantom (6.4 cm) is marked by a horizontal dotted line at the y-axis. Reference images acquired without irradiation can be found in the Appendix (Figure C.2).

range in water as calculated from equation 4.2 was 4.2 cm (190 MeV), 6.4 cm (200 MeV), 8.6 cm (210 MeV), and 12.2 cm (225 MeV). The resulting range differences relative to the reference energy of 200 MeV are given in Table 4.3.

To compare the expected proton range to the range on the MR images, the range was measured on the images as follows (cf. Figure 4.12). For the GE sequence, the measured range was defined as the depth of the maximum amplitude of the inflected central curve. For the IRGE sequence, it was defined as the depth of the white line distal to the beam-shaped hypointense region. These definitions were chosen not for physical reasons but to reduce observer-dependence and increase the reproducibility of the measurement.

Results

As depicted in Figure 4.13, a current-dependence of the beam-induced signal was observed. The signal decreased with decreasing beam current for both the GE and the IRGE

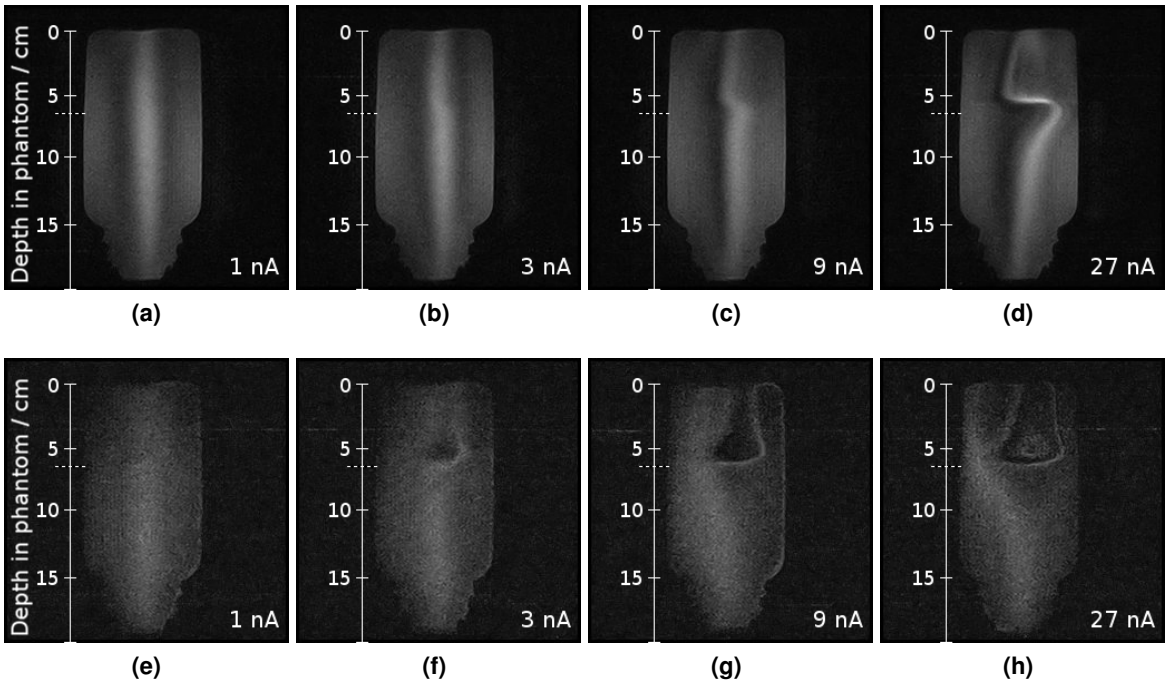

Figure 4.13: GE (top row) IRGE (bottom row) images acquired during irradiation with proton beam currents of 1 nA, 3 nA, 9 nA and 27 nA (from left to right) at 200 MeV. The expected range in the phantom (6.4 cm) is marked by a horizontal dotted line at the y-axis.

sequence. The influence of the beam was hardly visible at 1 nA for both sequences, but clearly visible for 3 nA and higher. The amplitude of the lightning-shaped inflected curve increased with increasing proton current in the GE sequence. In the IRGE sequence, a hyperintense region was visible in the Bragg peak region for the highest currents (27 nA and 43 nA).

The range-dependence of the beam-induced signal was visible in the GE and the IRGE sequence (see Figure 4.14). The measured ranges are given in Table 4.3. For both sequences, both absolute ranges and range differences agreed with the calculated values within 2 mm, except for 200 MeV in the IRGE sequence (3 mm). Measured ranges for both sequences tended to be smaller than the calculated ranges.

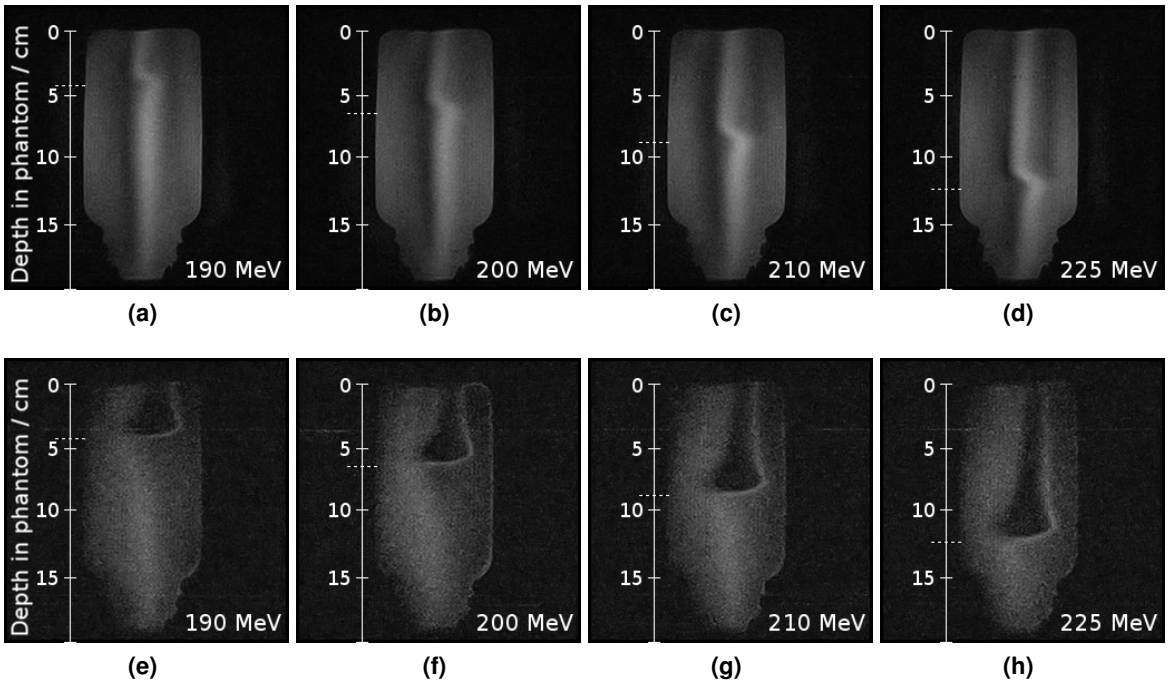

Figure 4.14: GE (top row) and IRGE (bottom row) images acquired under simultaneous irradiation with an expected proton range (marked by horizontal dotted line) of 4.2 cm, 6.4 cm, 8.6 cm and 12.2 cm (from left to right) at 9 nA.

4.3.3 Target Material Dependence

Material and Methods

To test the dependence of the effect on the target material, further images were acquired during irradiation of six other target materials, which varied in composition and viscosity: ethanol, petroleum, sugar syrup, mayonnaise, gelatine, and smoked pork chop. All materials except for the pork chop were filled in identical cylindrical bottles as described above. The pork chop had a dimension of approximately ($10 \times 14 \times 6$) cm^3. The beam energy and

Energy / MeV	190 (a)	200 (b)	210 (c)	225 (d)	(a) - (b)	(c) - (b)	(d) - (b)
Calculated	4.2	6.4	8.6	12.2	- 2.2	+ 2.2	5.8
GE	4.0	6.3	8.7	12.2	- 2.3	+ 2.4	5.9
IRGE	4.0	6.1	8.4	12.0	- 2.1	+ 2.3	5.8

Table 4.3: Proton ranges in cm calculated from equation 2 and measured on the GE and IRGE MR sequences for different proton energies, and corresponding range differences relative to the reference energy (200 MeV).

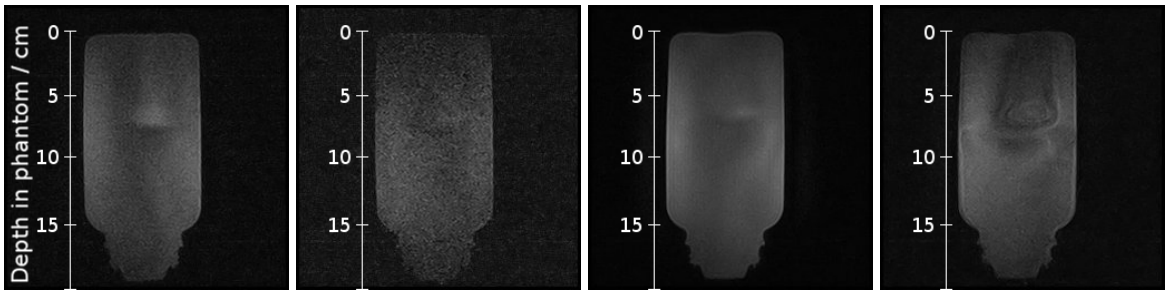

Figure 4.15: GE (a,c) and IRGE (b,d) images acquired under simultaneous irradiation at the maximum current (43 nA) of materials with visible beam-induced signal: ethanol (a,b) and petroleum (c,d).

current were set back to 200 MeV and 9 nA, respectively. An additional image was acquired at the maximum current (43 nA).

Results

Both effects were observed for both 9 nA and the maximum current in deionised water, ethanol and petroleum (see Figure 4.15). In mayonnaise, sugar syrup, gelatine, and pork chop, which are more viscose than the former three materials, no beam-induced effect was observed for both 9 nA and the maximum current (43 nA) in both sequences (see Figure 4.16).

4.3.4 Discussion

The experiments have shown that an influence of the beam on the MR image is measurable in a GE and a IRGE sequence. The influence was shown to be beam current- and range-dependent, with an agreement of expected and measured range differences of 2 mm. Deviations can most likely be attributed to setup uncertainties, uncertainties in range prediction, and uncertainties in the range measurement on the MR images.

A hyperintense vertical line was visible in the GE sequences without irradiation, which is a known effect for gradient-spoiled GE sequences (Epstein et al., 1996). Here, an additional phase encoding gradient field is used as a spoiler gradient to eliminate echoes arising from the remaining transverse magnetization of preceding repetition cycles by spin dephasing (see section 2.2.2). Since the magnetic field of the gradient is zero in the centre, the trans-

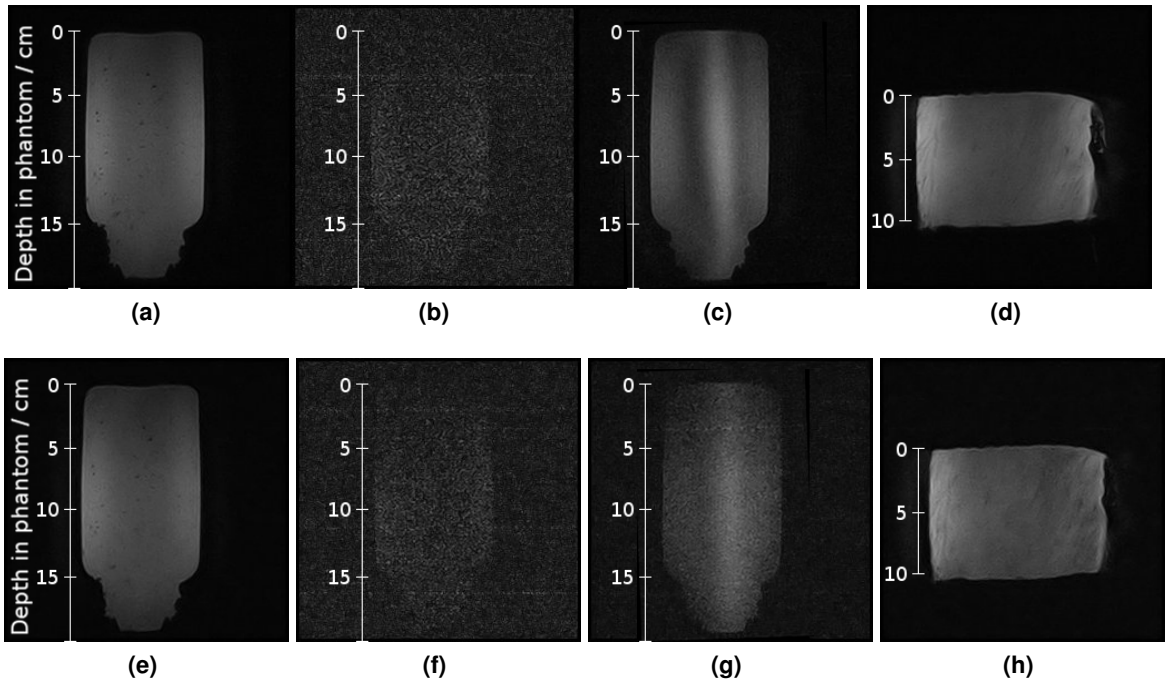

Figure 4.16: GE (top row) IRGE (bottom row) images acquired under simultaneous irradiation at the maximum current (43 nA) of materials without visible beam-induced signal: mayonnaise, sugar syrup, gelatine, and pork chop (from left to right).

verse magnetisation is not spoiled at this position and builds up with each excitation. This is visible as a line in the centre of the image, which is perpendicular to the phase encoding direction.

In deionised water, the proton beam induced a deformation of this line at the end of the beam range, and a beam-shaped signal in the IRGE sequence. Both effects did not disappear immediately after irradiation, but faded with a time constant in the order of tens of seconds after irradiation. Furthermore, they were observed in three liquids of different chemical composition, but not in four materials of higher viscosity. Therefore, a beam-induced local magnetic field change as well as chemical reactions depending on a specific ion or molecule, as is the case in Fricke and polymer gel dosimeters (Fricke and Morse, 1927; Lepage et al., 2001), appear to be improbable causes for the effect. A local increase in proton density can also be excluded as a possible cause, since this effect is expected to induce a signal increase, as opposed to the observed effect. Furthermore, the number of extra protons introduced by the beam is small relative to the number of protons in the target

material (see section 2.2.1 in Background chapter).

One possible explanation for the observed phenomenon is that the proton beam induced a local temperature increase in the target, which lead to heat convection inside the target. To estimate this effect, the temperature increase induced by a proton beam per Gray is approximated from the heat capacity of water $c_{\mathrm{w}} \approx 4.2\,\mathrm{kJ}/(\mathrm{kg\,K})$ as $\Delta T = \frac{\Delta E}{m c_{\mathrm{w}}} = \frac{D}{c_{\mathrm{w}}} \approx 0.000\,24\,\mathrm{K/Gy}$. For this experiment, i.e. at 18 Gy (corresponding to 9 nA during 35 seconds of image acquisition) in water at room temperature $T_0 = 20\,^{\circ}\mathrm{C}$, this translates into a temperature after irradiation of $T_1 = 20.004\,32\,^{\circ}\mathrm{C}$, which leads to a density decrease of $\Delta\rho = \rho(T_0) - \rho(T_1) \approx \rho(T_0)(1 - e^{-\Gamma(T_1 - T_0)}) \approx 10^{-3}\,\mathrm{kg/m^3}$, with the expansion coefficient $\Gamma \approx 0.2 \cdot 10^{-3}\,\mathrm{K^{-1}}$ (Demtröder, 2006). This density difference results in a buoyancy. When approximated as a sphere of $r \approx 1.5\,\mathrm{cm}$, the heated volume moves upwards with a speed of $v \approx \frac{2gr^2}{9\eta}\Delta\rho \approx 0.5\,\mathrm{mm/s}$, with $\eta \approx 1\,\mathrm{mPa\,s}$ the viscosity of water and $g \approx 10\,\mathrm{m/s^2}$ the gravitational acceleration (Stokes, 1951). This speed is fast enough for a considerable signal loss during image acquisition, as visible in the IRGE sequence. Since the protons move in the magnetic field gradient G_z, their phase may be altered relative to that expected for in-plane protons, which may lead to a local shift in phase-encoding direction, as visible in the GE sequence. Convection is impeded in viscose materials, which is consistent with the observation of no beam-induced effect in these materials.

To test the above hypothesis, further studies are necessary involving a phantom with either mechanically inhibited or controlled convection behaviour. This way, convection can be excluded or verified as a source of signal displacement. Furthermore, a comprehensive and systematic analysis of the influence of the different sequence parameters, especially for the materials which showed no beam-induced effects in this study, is expected to facilitate a better understanding of the phenomenon. Other influencing factors such as the timing of irradiation relative to the different MR imaging phases, the direction of the phase and frequency encoding gradients, the slice position and orientation, and the use of GE sequences with different spoiling techniques could be investigated.

k-space data is currently not accessible through the software of the used MR scanner but appears desirable since the contained phase data could be more informative and more sensitive to detect beam-induced changes. Spatial saturation pulses could allow to reduce the phantom signal in order to increase the relative beam signal. Moreover, an algorithm that automatically extracts the proton range from the MR images is expected to be able to reduce observer-dependent uncertainties.

Another possibility to detect the proton range via MRI may be dynamic nuclei polarisation (DNP). Here, the high polarisation of the target electrons is transferred to the protons via the introduction of radicals, which act as paramagnetic centres, and subsequent irradiation of a microwave pulse. This way, the proton polarisation is increased by a factor of approximately 100 (Gerfen et al., 1995). Since most radicals are produced in the Bragg peak, this could enable MR-based range verification. However, DNP is usually performed at low temperatures, and with a microwave pulse of high magnetic flux density. The technical feasibility in an MRiPT setup has not been investigated yet.

Once these issues have been addressed, this could allow for a further reduction of the proton current necessary to detect the proton range. If the effect will be transferable to viscose materials as present in the human body, it could possibly be used for in-vivo range verification. Otherwise, consistency tests of the proton range during machine-specific quality assurance could be an area of application. As this study showed that MR-based range verification is feasible in liquids, further research towards this aim is justified.

4.4 Summary

For the first time, an MR scanner has been integrated with a proton beam line. For this purpose, an open low-field MR scanner has been placed at the static proton research beam line of a proton therapy facility. The beam deflection induced by the static magnetic field of the scanner was taken into account for alignment of the beam and the FOV of the scanner. The pulse sequence-dependent dynamic gradient fields did not measurably affect the beam profile behind the MR scanner. The MR magnetic field homogeneity was within the vendor's specifications and not influenced by the rotation of the proton gantry in the neighbouring treatment room. No magnetic field compensation system was required for simultaneous operation of the MR scanner and the proton therapy system.

MR image quality was shown to be acceptable for the in-beam MR scanner both with and without simultaneous proton beam irradiation with energised beam line magnets. All geometrical parameters agreed with the mechanical dimensions of the used phantom within one pixel width, and most image quality parameters of the ACR were shown to be equivalent with and without simultaneous irradiation. However, as common for low-field MR scanners, the SNR of the MR images was low, which resulted in a low image uniformity and a high ghosting ratio in comparison to the ACR test criteria. A strong fluctuation of the vertical phantom position due to uncertainties in the pre-scan frequency calibration was observed, with an interquartile range of up to 1.5 mm. T_2^*-weighted GE images showed relevant nonuniform deformations due to magnetic field inhomogeneities. A significant influence of simultaneous irradiation was observed as a shift of the vertical phantom position and a decrease in the SNR, both of which can be explained by a change in the B_0 field induced by components of the fringe field of the beam line magnets directed parallel to B_0. While the decrease in SNR is not expected to be relevant (median differences were within 1.5), the sequence-dependent phantom shift (median differences of up to 0.7 mm) must be corrected for.

These results indicate that simultaneous MR imaging and proton beam irradiation is feasible without severe compromises to image or beam quality, but MR sequences need to be chosen with care in MRiPT. Sequences with strong gradients (i.e. high receiver bandwidths) are to be preferred due to a decreased risk of off-resonance voxel dislocation. Alternatively, since phase encoding is unaffected by changes in B_0, this method could be used in two instead of one of the image directions. These two approaches could, however, compromise

image quality due to increased spin dephasing (i.e. decreased SNR) and acquisition time, respectively. Another possibility would be a fixed MR-visible frame or markers surrounding the imaging object, which could be detected automatically on the image to define an image translation vector. The systematic beam line-induced image shifts can possibly be mitigated by performing the MR pre-scan calibration with energised beam line magnets. T_2^*-weighted sequences should only be applied with care due to the observed risk of geometrical distortions. Furthermore, future studies should include the effect of switching on the beam line magnets during MR image acquisition, which could deteriorate the acquired image in a non-trivial way, for example as ghosts in the frequency encoding direction.

Lastly, a current- and range-dependent influence of the beam on the MR image was shown to be measurable in fluids for two MR sequences. The effect was not observed in solid and viscose materials and presumably induced by convection. This method could be used for consistency tests of the proton range during machine-specific quality assurance in MRiPT. Further methods to be investigated in future studies, which could allow for in vivo MR-based range verification, include spatial saturation pulses, the definition of a beam-induced signature in k-space, and dynamic nuclei polarisation.

Overall, this proof of concept shows the feasibility and potential of in-beam MR imaging and justifies further research towards the development of a first prototype for MRiPT.

5 Discussion and Future Perspectives

The main findings of this thesis in the general context of MR-integrated proton therapy and their implications for future work are discussed in the following.

Magnetic-field induced beam deflection

The deflection of a proton beam slowing down in a medium inside a magnetic field is a problem unique to MRiPT. Consequently, this basic physics issue has only been picked up in the last years, with the aim to quantify the dosimetric consequences of magnetic field-induced beam deflection on the dose distribution in a patient. Monte Carlo particle tracking simulations are considered the gold standard for dose calculation in radiotherapy (Paganetti, 2012). However, prior to this work, Monte Carlo-based dose simulations inside magnetic fields had not been benchmarked with experimental data, which limited the validity of MRiPT treatment planning studies such as those performed by Hartman et al. (2015) and Moteabbed et al. (2014).

This work has confirmed experimentally that the deflected beam trajectory and Bragg peak position can be accurately predicted by Monte Carlo simulations within the measurement uncertainties (0.8 mm) for proton beam energies up to 180 MeV at 1 T. In comparison to the proton range uncertainties in the patient, which amount to about 8 mm at a proton range of 15 cm (Paganetti, 2012), the quoted measurement uncertainty appears acceptable.

These results suggest that proton beam deflection in a static transverse magnetic field is accurately predictable in a homogeneous medium for intermediate proton energies and magnetic flux densities, and therefore not impeding the feasibility of MRiPT. The deflection is a source of uncertainty which adds to the existent uncertainty sources of proton therapy, but may be further reduced in future studies. Furthermore, the deflection-induced uncertainty is expected to be more than compensated for by the potential of MRiPT to reduce motion-induced uncertainties.

At the same time, a future full commissioning of an MRiPT system must include absolute dose, beam profile and depth-dose measurements for the whole proton energy range, which were beyond the scope of this work, as well as measurements in heterogeneous media. Regarding the dosimetry devices to be used for this purpose, it is expected that correction procedures accounting for the magnetic field will be largely transferable from MRiXT, and probably even less complex due to the range of secondary electrons of proton beams being several orders of magnitude lower than for photon beams. First studies have recently shown a limited and dose-proportional effect of a magnetic field on film dosimeters (Lühr et al., 2018).

Even though this work has shown that Monte Carlo simulations can be used to accurately estimate beam deflection, this is still a time-consuming approach. High-performance computers are becoming more widely used and fast Monte Carlo dose calculations are under development (Giantsoudi et al., 2015; Tseung et al., 2015). Fast solutions are however required for real-time image-guided beam tracking as well as for simple estimates of beam deflection, e.g. to position dosimetry equipment such that the beam traverses it in spite of the deflection. Furthermore, as suggested by Hartman et al. (2015), it would be favourable for treatment planning in a magnetic field to perform the first steps of treatment plan optimisation with an analytical model and use Monte Carlo simulations only to finalise the dose calculation, in order to reduce the overall calculation time. For these purposes, analytical models had been proposed, which rely on approximations in order to reduce calculation time.

However, prior to this work, these methods had not been evaluated, compared against each other or benchmarked with Monte Carlo-based data, which rendered their applicability questionable. The analysis presented in this work has revealed that these models are indeed inaccurate for intermediate to high proton energies and magnetic flux densities, and not applicable to non-uniform, i.e. realistic patient anatomies or magnetic field distributions. The model that has been developed in this work, RAMDIM, overcomes these limitations and is therefore expected to be useful for fast and accurate MRiPT deflection estimation, treatment plan optimisation and beam tracking.

Notably, the RAMDIM algorithm is not capable of direct dose prediction but can only predict the central beam trajectory. A pencil beam dose calculation method has been recently introduced based on a similar algorithm and was shown to yield acceptable agreement to Monte Carlo simulations both in homogeneous and in slab geometries (Padilla-Cabal et al.,

2018; Fuchs et al., 2017). Further testing in patient geometries and realistic (non-uniform) magnetic fields against Monte Carlo simulations or experimental measurements appears to be the next step to verify this promising approach.

System design

Prior to this work, MRiPT has only been studied as a theoretical modality, without experimental evidence of its technical feasibility. The first in-beam MR system has been presented in this thesis, consisting of a low-field open MR scanner and a static research proton beam line. It has been shown that the magnetic field homogeneity and image quality of the in-beam MR scanner are sufficient for target volume identification in spite of the electromagnetically contaminated environment of the proton facility.

Two main reasons for this finding can be identified. Firstly, the magnetic field of the system, which is governed by the cyclotron and the beam line magnets, did not relevantly change during image acquisition, as discussed below. Secondly, the distance to the cyclotron (8 m) resulted in a small remaining magnetic field gradient at the position of the MR scanner, which could be compensated for by shimming. This distance was mainly determined by the diameter of the cyclotron, the thickness of the radiation shielding wall between the cyclotron vault and the experimental room where the MR scanner was positioned, and the space required to access the cyclotron and the MR scanner. If these dimensions are not strongly reduced in future MRiPT systems, this observation is expected not to be limited to the presented setup but transferable to such systems.

In line with previously published suggestions made by Schippers (2009) and Raaymakers et al. (2008), a low-field, open MR scanner was selected for the reasons of lower costs and a better accessibility of objects to be placed in the field-of-view. Furthermore, the deflection of the proton beam in the magnetic field of the scanner was limited and more easily predictable than for high-field scanners. Since image quality for the purpose of patient position verification and tumour tracking is not inherently better for high-field systems (see section 2.2.3), there is currently no clear indication that low-field systems should not be preferred for future MRiPT systems. The rise time and spatial linearity of the gradient fields, which are required for real-time and distortion-free imaging, respectively, are expected to be more important than the nominal magnetic flux density.

Another aspect of the system design is the choice of beam delivery, i.e. passive scatter-

ing versus active scanning (see section 2.1.2). While it has been shown in this work that an ex post correction of the proton beam deflection after treatment planning can only be implemented by the use of scanning beam magnets, the implementation of beam deflection into a treatment planning system may render such a correction unnecessary and thus allow for both modalities. Treatment planning studies are necessary to determine whether distortion-free dose distributions can be generated by adjusting the compensator and collimator used in the passive scattering technique. An important potential difference between the two modalities, which is specific to MRiPT, is the interference of the scanning magnets in an active scanning setup with MR image acquisition, as discussed below.

Magnetic field effects on MR image quality

In addition to the case of a static proton therapy facility, it was shown in this work that the magnetic field of the MR scanner was not relevantly affected by rotations of the beam line gantry in the neighbouring treatment room. This indicates that future studies using the presented in-beam system do not need to monitor the gantry angle, which frequently changes during a day of patient treatment. On the other hand, it is expected that activities in the treatment room may not fully be neglected, since the repeated switching of the beam line on and off for patient treatment may induce image artefacts. In this work, the status of the beam line magnets to the treatment room was not altered during image acquisition. The effects of switching the beam line magnets during MR image acquisition are to be included in future studies in order to assess the necessity of synchronised beam line magnet switching and MR image acquisition.

It has furthermore been shown in this work that simultaneous MR imaging and static proton beam irradiation is feasible without severe compromises to image or beam quality, which can be considered an important milestone for MRiPT. However, it was also found that three effects must be handled with care for in-beam image acquisition. Firstly, T_2^*-weighted sequences with a small gradient amplitude showed relevant image deformations due to inhomogeneities in the B_0 field. It is expected that this problem can be handled in MRiPT by applying this type of sequence only if high spatial accuracy is not required, or by fully avoiding it. Secondly, a small but significant reduction of the signal-to-noise ratio was observed during proton irradiation, most probably since the beam-line magnets slightly shifted the Larmor frequency distribution, which resulted in less proton spins being excited

by the RF pulse. Future studies will be necessary to evaluate how this decrease (of up to 3 %) translates into contrast-to-noise ratio and whether it is relevant for automated tumour tracking.

Thirdly, the accurate representation of the position of a static phantom on the MR image was identified as a problem in the in-beam MR system. Both a statistically fluctuating offset and a systematic shift during simultaneous irradiation were observed. The former can most likely be attributed to uncertainties in the pre-scan RF calibration procedure and should in the future be mitigated by optimising this calibration regarding robustness. This can be done by reducing the excited volume for acquisition of the FID signal and using a Gaussian fit to the resulting frequency distribution in order to determine the mean resonance frequency, instead of simply using the frequency with the maximum intensity, as currently implemented at the used MR scanner.

The systematic image shift during irradiation of up to 0.7 mm, on the other hand, can most likely be attributed to the magnetic fringe field of the beam line magnets altering the Larmor frequencies. This finding suggests that the pre-scan frequency calibration shall be performed in MRiPT only when the beam line magnets are already energised. Future studies are required to confirm this hypothesis, and, since the magnetic field of the beam line magnets is energy-dependent, to quantify the dependence of this method on the employed proton beam energy. Both the statistical and systematic object offset can furthermore be reduced by sequence design, i.e. by choosing strong gradients, high receiver bandwidths, or two-dimensional phase encoding, or by an MR-visible reference construction, such as a frame or markers, defining an image translation vector by rigid image registration. The geometrical accuracy may be investigated in more detail in future studies using larger distortion phantoms with three-dimensional grid structures.

These results, as established for four different sequences, are expected to be transferable to real-time MR sequences, which are however currently not available on the used scanner. Future studies may confirm this as a next step towards real-time MR-based image guidance.

An important limitation of this work is that the setup did not include a nozzle for pencil beam scanning, nor a close-by bending magnet as present in a gantry. Both are closer to the beam isocentre, and therefore the FOV of the MR scanner, and have less steeply decreasing fringe fields than the beam line magnets studied in this thesis. Furthermore, the magnetic field induced by the scanning magnets is not static, but changes dynamically

during irradiation with time constants in the same order as the MR image acquisition process (see section 2.1.2). Therefore, significant image distortions can be expected, and it is mandatory to address this influence in detail in future studies. Possible mitigation strategies include a well-conceived MR and beam pulse design with alternating irradiation and imaging phases. In an in-beam MRI system that is integrated into a proton gantry, the influence of the magnets mounted on the gantry is expected to make the B_0 field dependent on the gantry angle. As a result, active shimming coils may be necessary to adjust B_0 after each gantry rotation. A static but more cost-intensive alternative to reduce the effects of the scanning and gantry magnets on the MR scanner is building a magnetic shielding cage, which is made of ferromagnetic material such as carbon steel, silicon steel or Mu-metal (Turner, 2007).

MR-based range verification

MR-based range verification had been limited so far to retrospective methods, which were dependent on specific material compositions (Yuan et al., 2013; Bäck et al., 1999), and therefore could not be applied for on-line applications. This work has shown for the first time that fast MR-based range verification is feasible in various liquids, such as water, with standard MR sequences. The presented method can potentially be used in MRiPT for consistency tests of the proton range during machine-specific quality assurance. The question whether in vivo MR-based range verification will be feasible remains to be answered in future studies. This work has outlined possible strategies which can be pursued for this purpose, such as spatial saturation pulses, k-space signatures, and dynamic nuclei polarisation. The next steps towards this aim involve analytical and simulation-based predictions on the feasibility of these methods and an experimental verification thereof.

Conclusion

Overall, the work described in this thesis has improved and quantified the accuracy of beam deflection predictions and has shown the feasibility and potential of in-beam MR imaging. Further research towards the development of a first clinical prototype for MR-integrated proton therapy is clearly justified in order to optimise targeting accuracy in radiotherapy.

6 Summary/Zusammenfassung

6.1 Summary

The integration of magnetic resonance imaging (MRI) into proton therapy is expected to strongly increase the targeting accuracy in radiation therapy for cancerous diseases (Oborn et al., 2017). Especially for tumours situated in mobile organs in the thorax and abdomen, MR-integrated proton therapy (MRiPT) could enable the synchronisation of irradiation to the tumour position, resulting in less dose to normal tissue and reduced side effects. However, such an integration has been hindered so far by a lack of scientific studies on the potential mutual interference between the two components (Schippers and Lomax, 2011). This thesis was dedicated to two of these sources of interference, namely the deflection of the proton beam by the magnetic field of the MR scanner and, vice versa, alterations of the MR image induced by the electromagnetic fields of the proton therapy facility and by the beam itself.

Although previous work has indicated that there is general consensus that the trajectory of a slowing down proton beam in a homogeneous phantom inside a transverse magnetic field is predictable, a quantitative comparison of the published methods, as presented in the first part of this thesis, has shown that predictions of different models only agree for certain proton beam energies and magnetic flux densities. Therefore, shortcomings of previously published analytical methods have been analysed and quantified. The inclusion of critical assumptions and the lack of applicability to realistic, i.e. non-uniform, magnetic flux densities and patient anatomies have been identified as main problems. To overcome these deficiencies, a new semi-analytical model called RAMDIM has been developed. It was shown that this model is both applicable to more realistic setups and less assumptive than existing analytical approaches, and faster than Monte Carlo based particle tracking simulations. This model is expected to be useful in MRiPT for fast and accurate deflection estimations, treatment plan optimisation, and MR-guided beam tracking.

In a second step, the magnetic field-induced proton beam deflection has been measured for the first time in a tissue-mimicking medium by film dosimetry and has been compared

against Monte Carlo simulations. In a transverse magnetic field of 0.95 T, it was experimentally shown that the lateral Bragg peak displacement ranges between 1 mm and 10 mm for proton energies between 80 and 180 MeV in PMMA. Range retraction was found to be $\leq$ 0.5 mm. The measured Bragg peak displacement was shown to agree within 0.8 mm with Monte Carlo simulations. These results indicate that proton beam deflection in a homogeneous medium is accurately predictable for intermediate proton beam energies and magnetic flux densities by Monte Carlo simulations and therefore not impeding the feasibility of MRiPT.

In the second part of this thesis, an MR scanner has been integrated into a proton beam line for the first time. For this purpose, an open low-field MR scanner has been placed at the end of a fixed horizontal proton research beam line in a proton therapy facility. The beam deflection induced by the static magnetic field of the scanner was taken into account for alignment of the beam and the FOV of the scanner. The pulse sequence-dependent dynamic gradient fields did not measurably affect the transverse beam profile behind the MR scanner. The MR magnetic field homogeneity was within the vendor's specifications and not relevantly influenced by the rotation of the proton gantry in the neighbouring treatment room. No magnetic field compensation system was required for simultaneous operation of the MR scanner and the proton therapy system. These results proof that simultaneous irradiation and imaging is feasible in an in-beam MR setup.

The MR image quality of the in-beam MR scanner was then quantified by an adapted standard protocol comprising spin and gradient echo imaging and shown to be acceptable both with and without simultaneous proton beam irradiation. All geometrical parameters agreed with the mechanical dimensions of the used phantom within one pixel width. As common for low-field MR scanners, the signal-to-noise ratio (SNR) of the MR images was low, which resulted in a low image uniformity and a high ghosting ratio in comparison to the standardised test criteria. Furthermore, a strong fluctuation of the vertical phantom position due to uncertainties in the pre-scan frequency calibration was observed, with an interquartile range of up to 1.5 mm. T_2^*-weighted gradient echo images showed relevant nonuniform deformations due to magnetic field inhomogeneities.

Most image quality parameters were shown to be equivalent with and without simultaneous proton beam irradiation. However, a significant influence of simultaneous irradiation was observed as a shift of the vertical phantom position and a decrease in the SNR, both of which can be explained by a change in the $\vec{B}_0$ field of the MR scanner induced by compo-

nents of the fringe field of the beam line magnets directed parallel to $\vec{B}_0$. While the decrease in SNR is not expected to be relevant (median differences were within 1.5), the sequence-dependent phantom shift (median differences of up to 0.7 mm) can become non-negligible. These results show that the MR images are not severely distorted by simultaneous irradiation, but a dedicated optimisation of the pre-scan RF calibration and the MR sequences is required for MRiPT.

Lastly, a current-dependent influence of the proton beam on the MR image was shown to be measurable in water in two different MR sequences, which allowed for range verification measurements. The effect was observed in different liquids but not in highly viscose and solid materials, and most probably induced by heat convection. This method is expected to be useful in MRiPT for consistency tests of the proton range during machine-specific quality assurance.

In conclusion, this work has improved and quantified the accuracy of beam deflection predictions and shown the feasibility and potential of in-beam MR imaging, justifying further research towards a first MRiPT prototype.

6.2 Zusammenfassung

Es wird erwartet, dass die Integration der Magnetresonanztomografie (MRT) in die Protonentherapie die Treffgenauigkeit bei der Strahlentherapie für Krebserkrankungen deutlich verbessern wird (Oborn et al., 2017). Besonders für Tumoren in beweglichen Organen des Thorax oder des Abdomens könnte die MRT-integrierte Protonentherapie (MRiPT) eine Synchronisierung der Bestrahlung mit der Tumorposition ermöglichen, was zu einer verminderten Normalgewebsdosis und weniger Nebenwirkungen führen könnte. Bis heute ist solch eine Integration jedoch aufgrund fehlender Studien zu potenziellen gegenseitigen Störeinflüssen dieser beiden Systeme nicht vollzogen worden (Schippers and Lomax, 2011). Diese Arbeit widmete sich zwei solcher Störeinflüsse, und zwar der Ablenkung des Protonenstrahls im Magnetfeld des MRT- Scanners, und umgekehrt, dem Einfluss der elekromagnetischen Felder der Protonentherapieanlage und des Protonenstrahls selbst auf die MRT-Bilder.

Obwohl vorangegangene Studien den derzeitigen Konsens aufgezeigt haben, dass die Trajektorie eines abgebremsten Protonenstrahls im homogenen Phantom in einem transversalen Magnetfeld vorhersagbar ist, zeigte sich im quantitativen Vergleich der publizierten Modelle, der im ersten Teil dieser Arbeit vorgestellt wurde, dass die Vorhersagen dieser Modelle nur für eine begrenzte Anzahl von Kombinationen aus Magnetfeldstärke und Protonenenergie übereinstimmen. Die Schwächen bestehender analytischer Modelle wurden deshalb analysiert und quantifiziert. Kritische Annahmen und die mangelnde Anwendbarkeit auf realistische, d.h. inhomogene Magnetfeldstärken und Patientengeometrien wurden als Hauptprobleme identifiziert. Um diese zu überwinden, wurde ein neues semianalytisches Modell namens RAMDIM entwickelt. Es wurde gezeigt, dass dieses auf realistischere Fälle anwendbar und genauer ist als existierende analytische Modelle und dabei schneller als Monte-Carlo-basierte Teilchenspursimulationen. Es wird erwartet, dass dieses Modell in der MRiPT Anwendung findet zur schnellen und genauen Ablenkungsberechnung, zur Betrahlungsplanoptimierung und bei der MRT-geführten Strahlnachführung.

In einem zweiten Schritt wurde die magnetfeldinduzierte Protonenstrahlablenkung in einem gewebeähnlichen Material durch Filmdosimetrie erstmalig gemessen und mit Monte-Carlo-Simulationen verglichen. In einem transversalen Magnetfeld einer Flussdichte von 0,95 T wurde experimentell gezeigt, dass die laterale Versetzung des Bragg-Peaks für Protonenenergien zwischen 80 und 180 MeV in PMMA zwischen 1 und 10 mm liegt. Die

Retraktion des Bragg-Peaks war $\leq$ 0,5 mm. Es wurde gezeigt, dass die gemessene Versetzung des Bragg-Peaks innerhalb von 0,8 mm mit Monte-Carlo-basierten Vorhersagen übereinstimmt. Diese Ergebnisse weisen darauf hin, dass die Protonenstrahlablenkung durch Monte-Carlo-Simulationen genau vorhersagbar ist und damit der Realisierbarkeit der MRiPT nicht im Wege steht.

Im zweiten Teil dieser Arbeit wurde erstmalig ein MRT-Scanner in eine Protonenstrahlführung integriert. Hierfür wurde ein offener Niederfeld-MRT-Scanner am Ende einer statischen Forschungsstrahlführung einer Protonentherapieanlage platziert. Die durch das statische Magnetfeld des MRT-Scanners hervorgerufene Strahlablenkung wurde bei der Ausrichtung des MRT-Scanners berücksichtigt. Die sequenzabhängigen, veränderlichen Gradientenfelder hatten keinen messbaren Einfluss auf das transversale Strahlprofil hinter dem MRT-Scanner. Die Magnetfeldhomogenität des Scanners lag innerhalb der Herstellervorgaben und zeigte keinen relevanten Einfluss von Rotationen der Protonengantry im benachbarten Bestrahlungsraum. Eine magnetische Abschirmung war zum gleichzeitigen Betrieb des MRT-Scanners und der Protonentherapieanlage nicht notwendig. Dies beweist die Machbarkeit gleichzeitiger Bestrahlung und Bildgebung in einem ersten MRiPT Aufbau.

Die MRT-Bildqualität des Aufbaus wurde darauffolgend anhand eines angepassten Standardprotokolls aus Spin-Echo- und Gradienten-Echo-Sequenzen quantifiziert und es wurde gezeigt, dass die Bildqualität sowohl ohne als auch mit gleichzeitiger Bestrahlung hinreichend ist. Alle bestimmten geometrischen Parameter stimmten mit den physikalischen Abmessungen des verwendeten Phantoms innerhalb eines Bildpixels überein. Wie es für Niederfeld-MRT-Scanner üblich ist, war das Signal-Rausch-Verhältnis (SNR) der MRT-Bilder gering, was im Vergleich zu den Standardkriterien zu einer geringen Bildhomogenität und zu einem hohen Geisterbildanteil im Bild führte. Außerdem wurde aufgrund von Unsicherheiten in der Hochfrequenzkalibrierung des MRT-Scanners eine starke Schwankung der vertikalen Phantomposition mit einem Interquartilabstand von bis zu 1,5 mm beobachtet. T_2^*-gewichtete Gradientenechosequenzen zeigten zudem aufgrund von Magnetfeldinhomogenitäten relevante ortsabhängige Bildverzerrungen.

Es wurde gezeigt, dass die meisten Bildqualitätsparameter mit und ohne gleichzeitige Betrahlung äquivalent sind. Es wurde jedoch ein signifikanter Betrahlungseinfluss in Form von einer vertikalen Bildverschiebung und einer Verminderung des SNR beobachtet, die durch eine Änderung im Magnetfeld des MRT-Scanners erklärt werden können, welche durch zu diesem Feld parallel ausgerichtete Komponenten im Fernfeld der Strahlführungs-

magneten hervorgerufen wird. Während das verminderte SNR vermutlich irrelevant ist (Differenz im Median $\leq$ 1,5), ist die sequenzabhängige Bildverschiebung (Differenz im Median bis zu 0,7 mm) nicht immer vernachlässigbar. Diese Ergebisse zeigen, dass die MRT-Bilder durch gleichzeitige Bildgebung nicht schwerwiegend verfälscht werden, dass aber eine dedizierte Optimierung der Hochfrequenzkalibrierung und der MRT-Bildsequenzen notwendig ist.

Im letzten Teil der Arbeit wurde gezeigt, dass ein stromabhängiger Einfluss des Protonenstrahls auf MRT-Bilder eines Wasserphantoms durch zwei verschiedene MRT-Sequenzen messbar gemacht und zur Reichweiteverifikation genutzt werden kann. Der Effekt war in verschiedenen Flüssigkeiten, jedoch nicht in viskosen und festen Materialen, nachweisbar und wurde auf Hitzekonvektion zurückgeführt. Es wird erwartet, dass diese Methode in der MRiPT für Konstanztests der Protonenreichweite bei der Maschinenqualitätssicherung nützlich sein wird.

Zusammenfassend hat diese Arbeit die Genauigkeit der Vorhersage der Strahlablenkung quantifiziert und verbessert, sowie Potenzial und Realisierbarkeit einer gleichzeitigen MRT-Bildgebung und Protonenbestrahlung gezeigt. Die weitere Entwicklung eines ersten MRiPT-Prototyps ist demnach gerechtfertigt.

Bibliography

Agostinelli S, Allison J, Amako K, Apostolakis J, Araujo H, Arce P, Asai M, Axen D, Banerjee S, Barrand G, Behner F, Bellagamba L, Boudreau J, Broglia L, Brunengo A, Burkhardt H, Chauvie S, Chuma J, Chytracek R, Cooperman G, Cosmo G, Degtyarenko P, Dell'Acqua A, Depaola G, Dietrich D, Enami R, Feliciello A, Ferguson C, Fesefeldt H, Folger G, Foppiano F, Forti A, Garelli S, Giani S, Giannitrapani R, Gibin D, Cadenas JG, González I, Abril GG, Greeniaus G, Greiner W, Grichine V, Grossheim A, Guatelli S, Gumplinger P, Hamatsu R, Hashimoto K, Hasui H, Heikkinen A, Howard A, Ivanchenko V, Johnson A, Jones F, Kallenbach J, Kanaya N, Kawabata M, Kawabata Y, Kawaguti M, Kelner S, Kent P, Kimura A, Kodama T, Kokoulin R, Kossov M, Kurashige H, Lamanna E, Lampén T, Lara V, Lefebure V, Lei F, Liendl M, Lockman W, Longo F, Magni S, Maire M, Medernach E, Minamimoto K, de Freitas PM, Morita Y, Murakami K, Nagamatu M, Nartallo R, Nieminen P, Nishimura T, Ohtsubo K, Okamura M, O'Neale S, Oohata Y, Paech K, Perl J, Pfeiffer A, Pia M, Ranjard F, Rybin A, Sadilov S, Salvo ED, Santin G, Sasaki T, Savvas N, Sawada Y, et al. (2003). Geant4 - a simulation toolkit. Nucl Instr Meth Phys Res A 506:250–303.

Allison J, Amako K, Apostolakis J, Araujo H, Dubois PA, Asai M, Barrand G, Capra R, Chauvie S, Chytracek R, Cirrone GAP, Cooperman G, Cosmo G, Cuttone G, Daquino GG, Donszelmann M, Dressel M, Folger G, Foppiano F, Generowicz J, Grichine V, Guatelli S, Gumplinger P, Heikkinen A, Hrivnacova I, Howard A, Incerti S, Ivanchenko V, Johnson T, Jones F, Koi T, Kokoulin R, Kossov M, Kurashige H, Lara V, Larsson S, Lei F, Link O, Longo F, Maire M, Mantero A, Mascialino B, McLaren I, Lorenzo PM, Minamimoto K, Murakami K, Nieminen P, Pandola L, Parlati S, Peralta L, Perl J, Pfeiffer A, Pia MG, Ribon A, Rodrigues P, Russo G, Sadilov S, Santin G, Sasaki T, Smith D, Starkov N, Tanaka S, Tcherniaev E, Tome B, Trindade A, Truscott P, Urban L, Verderi M, Walkden A, Wellisch JP, Williams DC, Wright D, and Yoshida H (2006). Geant4 developments and applications. IEEE Trans Nucl Sci 53:270–278.

Almhagen E. 2015. Development and validation of a scanned proton beam model for dose distribution verification using Monte Carlo. Stockholm University, MA thesis.

American Cancer Society (2017). Cancer facts and figures. Retrieved Nov 25, 2018. URL: https://www.cancer.org/content/dam/cancer-org/research/cancer-facts-and-statistics/annual-cancer-facts-and-figures/2017/cancer-facts-and-figures-2017.pdf.

American College of Radiology (2017). Phantom test guidance of use of the small MRI phantom for the MRI accreditation program. Retrieved Mar 9, 2018. URL: https://www.acraccreditation.org/-/media/ACRAccreditation/Documents/MRI/SmallPhantomGuidance.pdf.

Ansorge R and Graves M (2016). The Physics and Mathematics of MRI. IOP Concise Physics.

Bäck SA, Medin J, Magnusson P, Olsson P, Grusell E, and Olsson LE (1999). Ferrous sulphate gel dosimetry and MRI for proton beam dose measurements. Phys Med Biol 44:1983–1996.

Baskar R, Lee KA, Yeo R, and Yeoh KW (2012). Cancer and radiation therapy: current advances and future directions. Int J Med Sci 9:193–199.

Baumann M, Krause M, Overgaard J, Debus J, Bentzen SM, Daartz J, Richter C, Zips D, and Bortfeld T (2016). Radiation oncology in the era of precision medicine. Nat Rev Cancer 16:234–249.

Bengua G, Ishikawa M, Sutherland K, Horita K, Yamazaki R, Fujita K, Onimaru R, Katoh N, Inoue T, Onodera S, and Shirato H (2010). Evaluation of the effectiveness of the stereotactic body frame in reducing respiratory intrafractional organ motion using the real-time tumor-tracking radiotherapy system. Int J Radiat Oncol Biol Phys 77:630–636.

Berger MJ, Coursey JS, Zucker MA, and Chang J (2005). ESTAR, PSTAR, and ASTAR: Computer programs for calculating stopping-power and range tables for electrons, protons, and Helium ions. Version 1.2.3, Retrieved Apr 27, 2015. National Institute of Standards and Technology. Gaithersburg, MD.

Bert C, Saito N, Schmidt A, Chaudhri N, Schardt D, and Rietzel E (2007). Target motion tracking with a scanned particle beam. Med Phys 34:4768–4771.

Bethe H (1930). Zur Theorie des Durchgangs schneller Korpuskularstrahlen durch Materie. Ann Phys 397:325–400.

Bielajew AF (1993). The effect of strong longitudinal magnetic fields on dose deposition from electron and photon beams. Med Phys 20:1171–1179.

Bieri O and Scheffler K (2013). Fundamentals of balanced steady state free precession MRI. J Magn Reson Imaging 38:2–11.

Blackmore EW (1985). Radiation effects of protons on Samarium-Cobalt permanent magnets. IEEE Trans Nucl Sci 32:3669–3671.

Bloch F (1933). Zur Bremsung rasch bewegter Teilchen beim Durchgang durch Materie. Ann Phys 408:285–320.

Bloch F (1946). Nuclear induction. Phys Rev 70:460–474.

Bloch F, Hansen WW, and Packard M (1946). Nuclear induction. Phys Rev 69:127.

Boda-Heggemann J, Knopf A, Simeonova-Chergou A, Wertz H, Stieler F, Jahnke A, Jahnke L, Fleckenstein J, Vogel L, Arns A, Blessing M, Wenz F, and Lohr F (2016). Deep inspiration breath hold-based radiation therapy: a clinical review. Int J Radiat Oncol Biol Phys 94:478–492.

Bohoudi O, Bruynzeel A, Senan S, Cuijpers J, Slotman B, Lagerwaard F, and Palacios M (2017). Fast and robust online adaptive planning in stereotactic MR-guided adaptive radiation therapy (SMART) for pancreatic cancer. Radiother Oncol 125:439–444.

Bolsi A, Peroni M, Amelio D, Dasu A, Stock M, Toma-Dasu I, Witt-Nyström P, and Hoffmann AL (2018). Practice patterns of image guided particle therapy in Europe: A 2016 survey of the European Particle Therapy Network (EPTN). Radiother Oncol 128:4–8.

Bortfeld T (1997). An analytical approximation of the Bragg curve for therapeutic proton beams. Med Phys 24:2024–2033.

Bray F, Ferlay J, Soerjomataram I, Siegel RL, Torre LA, and Jemal A (2018). Global cancer statistics 2018: GLOBOCAN estimates of incidence and mortality worldwide for 36 cancers in 185 countries. CA Cancer J Clin 68:394–424.

Brix G, Kolem H, Nitz WR, Bock M, Huppertz A, Zech CJ, and Dietrich O (2008). Basics of magnetic resonance imaging and magnetic resonance spectroscopy. In: Reiser M, W WS, and Hricak H, (eds). *Magnetic Resonance Tomography*. Springer, Berlin, Heidelberg, Germany. Chap. 2, pp. 3–167.

Brock KK, Mutic S, McNutt TR, Li H, and Kessler ML (2017). Use of image registration and fusion algorithms and techniques in radiotherapy: Report of the AAPM Radiation Therapy Committee Task Group No. 132. Med Phys 44:e43–e76.

Brown IG (2004). The physics and technology of ion sources. Wiley-VHC, Freiburg, Germany.

Burigo LN (2018). IMPT plan delivery adaption for in-line magnetic field in MR-guided proton therapy. Abstract at 3rd Geant4 International User Conference.

Burke B, Wachowicz K, Fallone BG, and Rathee S (2012). Effect of radiation induced current on the quality of MR images in an integrated linac-MR system. Phys Med Biol 39:6139–6147.

Cai J, Read PW, Altes TA, Molloy JA, Brookeman JR, and Sheng K (2006). Evaluation of the reproducibility of lung motion probability distribution function (PDF) using dynamic MRI. Phys Med Biol 52:365.

Camps SM, Fontanarosa D, de With PHN, Verhaegen F, and Vannest BGL (2018). The use of ultrasound imaging in the external beam radiotherapy workflow of prostate cancer patients. Biomed Res Int 2018:7569590.

Carr HY and Purcell EM (1954). Effects of diffusion on free precession in nuclear magnetic resonance experiments. Phys Rev 94:630–638.

Chandarana H, Wang H, Tijssen RHN, and Das I (2018). Emerging role of MRI in radiation therapy. J Magn Reson Imaging 48:1468–1478.

Cheng CW, Ferguson SG, Jordan D, Jesseph F, Johnson M, Bouchet L, Mansur D, and Wessels B (2016). Impact of the high magnetic field and RF power in a superconducting cyclotron on the operation of a nearby MRI facility. J Proton Ther 2:1–10.

Cheung JP, Park PC, Court LE, Zhu XR, Kudchadker RJ, Frank SJ, and Dong L (2013). A novel dose-based positioning method for CT image-guided proton therapy. Med Phys 40:051714.

Czernohorsky V. 2016. Automatisierte Qualitätssicherung anatomischer MRT-Bildgebung für die bildgestützte Strahlentherapie. Technische Universität Dresden, MA thesis.

Danly CR, Merrill FE, Barlow D, and Mariam FG (2014). Nonuniform radiation damage in permanent magnet quadrupoles. Rev Sci Instrum 85:83305.

Davids M, Zöllner FG, Ruttorf M, Nees F, Flor H, Schumann G, and Schad LR (2014). Fully-automated quality assurance in multi-center studies using MRI phantom measurements. Magn Reson Imaging 32:771–780.

De Ruysscher D, Sterpin E, Haustermans K, and Depuydt T (2015). Tumour movement in proton therapy: solutions and remaining questions: a review. Cancers 7:1143–1153.

Demtröder W (2006). Experimentalphysik 1: Mechanik und Wärme. Springer-Verlag, Heidelberg Berlin, Germany.

Dolde K, Naumann P, David C, Gnirs R, Kachelriess M, Lomax AJ, Saito N, Weber DC, Pfaffenberger A, and Zhang Y (2018). 4D dose calculation for pencil beam scanning proton therapy of pancreatic cancer using repeated 4DMRI datasets. Phys Med Biol 63:165005.

Dong B, Graves YJ, Jia X, and Jiang SB (2012). Optimal surface marker locations for tumor motion estimation in lung cancer radiotherapy. Phys Med Biol 57:8201–8215.

Dowdell S, Grassberger C, Sharp GC, and Paganetti H (2013). Interplay effects in proton scanning for lung: a 4D Monte Carlo study assessing the impact of tumor and beam delivery parameters. Phys Med Biol 58:4137–4156.

Doyle FH, Pennock JM, Orr JS, Gore JC, Bydder GM, Steiner RE, Young IR, Clow H, Gilderdale DRBMBDJ, and Walters PE (1981). Imaging of the brain by nuclear magnetic Resonance. The Lancet 318:53–57.

Duda RO and Hart PE (1972). Use of the Hough transformation to detect lines and curves in pictures. Comm ACM 15:11–15.

Dünger L (2017). Entwicklung und Etablierung der automatisierten Qualitätssicherung für Magnetresonanztomographie in der bildgestützten Strahlentherapie. Technische Universität Ilmenau, BA thesis.

Edelstein WA, Hutchison JMS, Johnson G, and Redpath T (1980). Spin warp NMR imaging and applications to human whole-body imaging. Phys Med Biol 25:751–756.

Edmund JM, Kjer HM, van Lemput K, Hansen RH, Andersen JA, and Andreasen D (2013). A voxel-based investigation for MRI-only radiotherapy of the brain using ultra short echo times. Radiat Oncol 8:7501–7519.

Engelsman M and Kooy HM (2005). Target volume dose considerations in proton beam treatment planning for lung tumors. Med Phys 32:3549–3557.

Engelsman M, Lu HM, Herrup D, Bussiere M, and Kooy HM (2009). Commissioning a passive-scattering proton therapy nozzle for accurate SOBP delivery. Med Phys 36:2172–2180.

Engelsman M, Schwarz M, and Dong L (2013). Physics controversies in proton therapy. Semin Radiat Oncol 23:88–96.

Epstein FH, Mugler JP, and Brookeman JR (1996). Spoiling of transverse magnetization in gradient-Echo (GRE) imaging during the approach to steady state. Magn Reson Med 35:237–245.

Estermann I, Frisch OR, and Stern O (1933). Magnetic moment of the proton. Nature 132:169–170.

Fallone BG, Murray B, Rathee S, Stanescu T, Steciw S, Vidakovic S, Blosser E, and Tymofichuk D (2009). First MR images obtained during megavoltage photon irradiation from a prototype integrated linac-MR system. Med Phys 36:2084.

Fallone BG (2014). The rotating biplanar linac-magnetic resonance imaging system. Semin Radiat Oncol 24:200–202.

Farr JB, Mascia AE, Hsi WC, Allgower CE, Jesseph F, Schreuder AN, Wolanski M, Nichiporov DF, and Anferov V (2008). Clinical characterization of a proton beam continuous uniform scanning system with dose layer stacking. Med Phys 35:4945–4954.

Faßbender M, Shubin YN, Lunev VP, and Qaim SM (1997). Experimental studies and nuclear model calculations on the formation of radioactive products in interactions of medium energy protons with copper, zinc and brass: Estimation of collimator activation in proton therapy facilities. Appl Radiat Isot 9:1221–1230.

Feng M, an D Normolle JMB, Adusumilli S, Cao Y, Chenevert TL, and Ben-Josef E (2009). Characterization of pancreatic tumor motion using cine MRI: surrogates for tumor position should be used with caution. Int J Radiat Oncol Biol Phys 74:884–891.

Field L and Bryning M (Oct. 2013). 15/024,888: Visualization of beam trajectories in radiation therapy. US Patent Application.

Flanz J (2011). Particle beam scanning. In: Paganetti H, (ed). *Proton therapy physics*. CRC Press, Taylor & Francis Group.

Fricke H and Morse S (1927). The chemical action of Roentgen rays on dilute ferrosulphate solutions as a measure of dose. Am J Roentgenol Radium Ther 18:430–432.

Fuchs H, Moser P, Gröschl M, and Georg D (2017). Magnetic field effects on particle beams and their implications for dose calculation in MR guided particle therapy. Med Phys 44:1149–1156.

Gantz S. 2017. Characterization of the magnetic field of a 0.95 T permanent dipole magnet and experimental validation of proton beam deflection in a magnetic field within tissue-equivalent material. TU Dresden, MA thesis.

GATE collaboration (2017). Documentation and recommendations for users. retrieved Aug 18, 2016. URL: http://www.opengatecollaboration.org/UsersGuide.

Geant4 collaboration (2013). Reference Physics Lists. retrieved Aug 18, 2016. URL: http://geant4.cern.ch/support/proc%5C_mod%5C_catalog/physics%5C_lists/referencePL.shtml.

Geant4 collaboration (2014). Geant4 10.1 Release Notes. retrieved Aug 18, 2016. URL: http://geant4.cern.ch/support/ReleaseNotes4.10.1.html.

Gerfen GJ, Becerra LR, Hall DA, Griffin RG, Temkin RJ, and Singel DJ (1995). High frequency (140 GHz) dynamic nuclear polarization: Polarization transfer to a solute in frozen aqueous solution. J Chem Phys 102:9494.

Giantsoudi D, Schuemann J, Jia X, Dowdell S, Jiang S, and Paganetti H (2015). Validation of a GPU-based Monte Carlo code (gPMC) for proton radiation therapy: clinical cases study. Phys Med Biol 60:2257–2269.

Gierga DP, Brewer J, Sharp GC, Betke M, Willett CG, and Chen GTY (2005). The correlation between internal and external markers for abdominal tumors: implications for respiratory gating. Int J Radiat Oncol Biol Phys 61:1551–1558.

Gilles M, Fayad H, Miglierini P, Clément JF, Scheib S, Cozzi L, Bert J, Boussion N, Schick U, Pradier O, and Visvikis D (2016). Patient positioning in radiotherapy based on surface imaging using time of flight cameras. Med Phys 43:4833–4841.

Gottschalk B (2011). Physics of proton interactions with matter. In: Paganetti H, (ed). *Proton Therapy Physics*. CRC Press, Taylor & Francis Group.

Grassberger C, Dowdell S, Sharp G, and Paganetti H (2015). Motion mitigation for lung cancer patients treated with active scanning proton therapy. Med Phys 42:2462–2469.

Grevillot L, Frisson T, Zahra N, Bertrand D, Stichelbaut F, Freud N, and Sarrut D (2010). Optimization of GEANT4 settings for proton pencil beam scanning simulations using GATE. Nucl Instr Meth Phys Res B 268:3295–3305.

Grozinger SO, Rietzel E, Li Q, Bert C, Haberer T, and Kraft G (2006). Simulations to design an online motion compensation system for scanned particle beams. Phys Med Biol 51:3517–3531.

Gultekin DH and Gore JC (2005). Temperature dependence of nuclear magnetization and relaxation. J Magn Reson 172:133–141.

Hahn E (1980). Spin echoes. Phys Rev 80:580–594.

Hanley J, Debois MM, Mah D, Mageras GS, Raben A, Rosenzweig K, Mychalczak B, Schwartz LH, Gloeggler PJ, Lutz W, Ling CC, Leibel SA, Fuks Z, and Kutcher GJ (1999). Deep inspiration breath-hold technique for lung tumors: the potential value of target immobilization and reduced lung density in dose escalation. Int J Radiat Oncol Biol Phys 45:603–611.

Hartman J, Kontaxis C, Bol GH, Frank SJ, Lagendijk JJW, van Vulpen M, and Raaymakers BW (2015). Dosimetric feasibility of intensity modulated proton therapy in a transverse magnetic field of 1.5 T. Phys Med Biol 60:5955–5969.

Hayashi N, Watanabe Y, Masumoto T, Mori H, Aoki S, Ohtomo K, Okitsu O, and Takahashi T (2004). Utilization of low-field MR scanners. Magn Reson Med Sci 3:7–38.

Heerkens H, Reerink O, Intvena PW, Hiensch R, van den Berg CAT, Crijns SPM, van Vulpen M, and Meijera GJ (2017). Pancreatic tumor motion reduction by use of a custom abdominal corset. Phys Imag Radiat Oncol 2:7–10.

Henke L, Kashani R, Robinson C, Curcuru A, DeWees T, Bradley J, Green O, Michalski J, Mutic S, and Parikh P (2018). Phase I trial of stereotactic MR-guided online adaptive radiation therapy (SMART) for the treatment of oligometastatic or unresectable primary malignancies of the abdomen. Radiother Oncol 126:519–526.

Hoffmann A and Speck O (Jan. 2016). DE 10 2016 100 638.6: Verfahren und Vorrichtung. German Patent Application.

Hofman MBM, Kuijer JPA, de Ridder JW, Perk LR, and Verdaasdonk RM (2013). Building a combined cyclotron and MRI facility: Implications for interference. Med Phys 40:012303.

Holm S (1979). A simple sequentially rejective multiple test procedure. Scand J Stat 6:65–70.

Holthusen H (1936). Erfahrungen über die Verträglichkeitsgrenze für Röntgenstrahlen und deren Nutzanwendung zur Verhütung von Schäden. Strahlentherapie 57:254–269.

Hoogcarspel SJ, Zijlema SE, Tijssen RHN, Kerkmeijer LGW, Jürgenliemk-Schulz IM, Lagendijk JJW, and Raaymakers BW (2018). Characterization of the first RF coil dedicated to 1.5 T MR guided radiotherapy. Phys Med Biol 63:025014 1-10.

ICRU (1993). Stopping powers and ranges for protons and alpha particles. ICRU Report 49.

ICRU (2009). Stopping of ions heavier than Helium. ICRU Report 73.

Inoue T, Widder J, van Dijk LV, Takegawa H, Koizumi M, Takashina M, Usui K, Kurokawa C, Sugimoto S, Saito AI, Sasai K, Van't Veld AA, Langendijk JA, and Korevaar EW (2016). Limited impact of setup and range uncertainties, breathing motion, and interplay effects in robustly optimized intensity modulated proton therapy for stage III non-small cell lung cancer. Int J Radiat Oncol Biol Phys 96:661–9.

Ito Y, Yasuda K, Ishigami R, Hatori S, Okada O, Ohashi K, and Tanaka S (2001). Magnetic flux loss in rare-earth magnets irradiated with 200 MeV protons. Nucl Instr Meth Phys Res B 183:323–328.

J. Perl et al. (2016). TOPAS documentation: default parameters. retrieved Dec 27, 2017. URL: http://topas.readthedocs.io/en/latest/parameters/defaults.html.

Jaffray DA, Siewerdsen JH, Wong JW, and Martinez AA (2002). Flat-panel cone-beam computed tomography for image-guided radiation therapy. Int J Radiat Oncol Biol Phys 53:1337–1349.

Jäkel O (2009). Medical physics aspects of particle therapy. Radiat Prot Dosimetry 137:56–166.

Jakobi A, Perrin R, Knopf A, and Richter C (2018). Feasibility of proton pencil beam scanning treatment of free-breathing lung cancer patients. Acta Oncol 57:203–210.

James F (1990). A review of pseudorandom number generators. Comput Phys Commun 60:329–344.

Janni JF (1982). Proton range-energy tables, 1 keV - 10 GeV. Atomic Data and Nuclear Tables 27:147–339.

Jursinic PA and Mackie TR (1996). Characteristics of secondary electrons produced by 6, 10 and 24 MV x-ray beams. Phys Med Biol 41:1499–1509.

Kanai T, Kawachi K, Kumamoto Y, Ogawa H, Yamada T, Matsuzawa H, and Inada T (1980). Spot scanning system for proton radiotherapy. Med Phys 7:365–369.

Kang Y, Zhang X, Chang JY, Wang H, Wei X, Liao Z, Komaki R, Cox JD, Balter PA, Liu H, Zhu XR, Mohan R, and Dong L (2007). 4D proton treatment planning strategy for mobile lung tumors. Int J Radiat Oncol Biol Phys 67:906–914.

Keall PJ, Barton M, and Crozier S (2014). The Australian magnetic resonance imaging-linac program. Semin Radiat Oncol 24:203–206.

Knopf AC, Hong TS, and Lomax A (2011). Scanned proton radiotherapy for mobile targets-the effectiveness of re-scanning in the context of different treatment planning approaches and for different motion characteristics. Phys Med Biol 56:7257–7271.

Koivula L, Wee L, and Korhonen J (2016). Feasibility of MRI-only treatment planning for proton therapy in brain and prostate cancers: Dose calculation accuracy in substitute CT images. Med Phys 43:4634–4642.

Kontaxis C, Bol G, Lagendijk J, and Raaymakers B (2015). A new methodology for inter- and intrafraction plan adaptation for the MR-linac. Phys Med Biol 60:7485–7497.

Korreman SS, Juhler-Nottrup T, and Boyer AL (2008). Respiratory gated beam delivery cannot facilitate margin reduction, unless combined with respiratory correlated image guidance. Radiother Oncol 86:61–68.

Kry SF, Johnson JL, White RA, Howell RM, Kudchadker RJ, and Gillin MT (2011). Neutron-induced electronic failures around a high-energy linear accelerator. Med Phys 38:34–39.

Kuhn M and Overweg J (Dec. 2009). EP 2 379 172 B1: Therapeutic apparatus. Issued Mar 2013. European Patent Application.

Kurosu K, Takashina M, Koizumi M, Das IJ, and Moskvin V (2014). Optimization of GATE and PHITS Monte Carlo code parameters for uniform scanning proton beam based on simulation with FLUKA general-purpose code. Nucl Instr Meth Phys Res B 336:45–54.

Kurz C, Landry G, Resch AF, Dedes G, Kamp F, Ganswindt U, Belka C, Raaymakers BW, and Parodi K (2017). A Monte-Carlo study to assess the effect of 1.5 T magnetic fields on the overall robustness of pencil-beam scanning proton radiotherapy plans for prostate cancer. Phys Med Biol 62:8470–8482.

Lagarias JC, Reeds JA, Wright MH, and Wright PE (1998). Convergence properties of the Nelder-Mead simplex method in low dimensions. SIAM J Optimiz 9:112–147.

Lagendijk JJW, Raaymakers BW, van den Berg CAT, Moerland MA, Philippens ME, and van Vulpen M (2014a). MR guidance in radiotherapy. Phys Med Biol 59:R349–R369.

Lagendijk JJ, Raaymakers BW, and van Vulpen M (2014b). The magnetic resonance imaging-linac system. Semin Radiat Oncol 24:207–9.

Landau L (1944). On the energy loss of fast particles by ionization. J Phys USSR 8:201.

Landry G and Hua C (2018). Current state and future applications of radiological image guidance for particle therapy. Med Phys 45:e1066–e1095.

Lauterbur PC (1973). Image formation by induced local interactions: examples employing nuclear magnetic resonance. Nature 242:190–191.

Lepage M, Jayasekera M, Bäck S, and Baldock C (2001). Dose resolution optimization of polymer gel dosimeters using different monomers. Phys Med Biol 46:2665–80.

Li JS (2015). Investigation of MRI guided proton therapy. Med Phys 42:3311.

Li R, Jia X, Lewis JH, Gu X, Folkerts M, Men C, and Jiang SB (2010). Real-time volumetric image reconstruction and 3D tumor localization based on a single X-ray projection image for lung cancer radiotherapy. Med Phys 37:2822–2826.

Liney GP, Dong B, Begg J, Vial P, Zhang K, Lee F, Walker A, Rai R, Causer T, Alnaghy SJ, Oborn BM, Holloway L, Metcalfe P, Barton M, Crozier S, and Keall P (2016). Experimental results from a prototype high-field inline MRI-linac. Med Phys 43:5188–5194.

Liney GP, Dong B, Weber E, Rai R, Destruel A, Garcia-Alvarez R, Manton DJ, Jelen U, Zhang K, Barton M, Keall P, and Crozier S (2018a). Imaging performance of a dedicated radiation transparent RF coil on a 1.0 Tesla inline MRI-linac. Phys Med Biol 63:135005.

Liney GP, Whelan B, Oborn B, Barton M, and Keall P (2018b). MRI-linear accelerator radiotherapy systems. Clin Oncol 30:686–691.

Liu H, Koch HN, Starkschall G, Jacobson M, Forster K, Liao Z, Komaki R, and Stevens CW (2004). Evaluation of internal lung motion for respiratory-gated radiotherapy using MRI: Part II - Margin reduction of internal target volume. Int J Radiat Oncol Biol Phys 60:1473–1483.

Lomax AJ (2008). Intensity modulated proton therapy and its sensitivity to treatment uncertainties 2: the potential effects of inter-fraction and inter-field motions. Phys Med Biol 53:1043–1056.

Lomax A (2018). What will the medical physics of proton therapy look like 10 yr from now? A personal view. Med Phys 45:e984–e993.

Lühr A, Burigo LN, Gantz S, Schellhammer SM, and Hoffmann AL (2018). Proton beam electron return effect: Monte Carlo simulations and experimental verification. Phys Med Biol (accepted).

Ma CMC and Paskalev K (2006). In-room CT techniques for image-guided radiation therapy. Med Dosim 31:30–39.

Maccabee HD, Madhvanath U, and Raju MR (1969). Tissue activation studies with alpha-particle beams. Phys Med Biol 14:213–224.

Mackie TR, Kapatoes J, Ruchala K, Lu W, Wu C, Olivera G, Forrest LJ, Tome W, Welsh J, Jeraj R, Harari PJ, Reckwerdt P, Paliwal BR, Ritter M, Keller H, Fowler J, and Mehta MP

(2003). Image guidance for precise conformal radiotherapy. Int J Radiat Oncol Biol Phys 56:89–105.

Mansfield P, Maudsley AA, and Baines T (1976). Fast scan proton density imaging by NMR. J Phys E: Sci Instrum 9:271–278.

Marchant TE and Joshi KD (2016). Comprehensive Monte Carlo study of patient doses from cone-beam CT imaging in radiotherapy. J Radiol Prot 37:13–30.

Markl M and Leupold J (2012). Gradient echo imaging. J Magn Reson Imaging 35:1274–89.

Marmitt GG, van Goethem M, Meijers M, Brandenburg S, and Knopf A (2018). Experimental validation of magnetic field deflection of proton beams for online MR-guided PT. Abstract at 6th MR in RT Symposium.

Maspero M, van den Berg CAT, Landry G, Belka C, Parodi K, Seevinck PR, Raaymakers BW, and Kurz C (2017). Feasibility of MR-only proton dose calculations for prostate cancer radiotherapy using a commercial pseudo-CT generation method. Phys Med Biol 62:9159–9176.

McClelland JR, Modat M, Arridge S, Grimes H, D'Souza D, Thomas D, Connell DO, Low DA, Kaza E, Collins DJ, Leach MO, and Hawkes DJ (2017). Respiratory motion models: A review. Phys Med Biol 62:4273–4292.

McRobbie DW, Moore EA, and Graves MJ (2017). MRI from Picture to Proton. Chapter 4: Lost in the pulse sequence jungle. Cambridge University Press.

Menten MJ, Wetscherek A, and Fast MF (2017). MRI-guided lung SBRT: Present and future developments. Physica Medica 44:139–149.

Mertens CJ, Moyers MF, Walker SA, and Tweed J (2010). Proton lateral broadening distribution comparisons between GRNTRN, MCNPX, and laboratory beam measurements. Adv Space Res 45:884–891.

METROLAB Instruments SA (2004). MFC-3045 magnetic field camera - user's manual. Version 3.00. Geneva, Switzerland.

Molière G (1947). Theorie der Streuung schneller geladener Teilchen I. Einzelstreuung am abgeschirmten Coulomb-Feld. Z Naturforsch 2a:133.

Molière G (1948). Theorie der Streuung schneller geladener Teilchen II. Mehrfach- und Vielfachstreuung. Z Naturforsch 3a:78.

Mori S, Yanagi T, Hara R, SharpS GC, Asakura H, Kumagai M, Kishimoto R, Yamada S, Kato H, Kandatsu S, and Kamada T (2010). Comparison of respiratory-gated and respiratory-ungated planning in scattered carbon ion beam treatment of the pancreas using four-dimensional computed tomography. Int J Radiat Oncol Biol Phys 76:303–312.

Mori S, Knopf AC, and Umegaki K (2018). Motion management in particle therapy. Med Phys 45:e994–e1010.

Moser P. 2015. Effects on particle beams in the presence of a magnetic field during radiation therapy. Technische Universität Wien, MA thesis.

Moteabbed M, Schuemann J, and Paganetti H (2014). Dosimetric feasibility of real-time MRI-guided proton therapy. Med Phys 41:111713.1–11.

Mutic S and Dempsey J (2014). The ViewRay system: magnetic resonance-guided and controlled radiotherapy. Semin Radiat Oncol 24:196–199.

National Centers for Environmental Information (2018). Magnetic field estimated values. Retrieved May 11th, 2018. https://www.ngdc.noaa.gov/geomag-web/.

National Electrical Manufacturers Association (2014). Magnetic resonance related standards. URL: https://www.nema.org/Products/Pages/Magnetic-Resonance.aspx.

Newhauser W, Fontenot J, Koch N, Dong L, Lee A, Zheng Y, Waters L, and Mohan R (2007). Monte Carlo simulations of the dosimetric impact of radiopaque fiducial markers for proton radiotherapy of the prostate. Phys Med Biol 52:2937–2952.

Noel CE, Parikh PJ, Spencer CR, Green OL, Hu Y, Mutic S, and Olsen JR (2015). Comparison of onboard low-field magnetic resonance imaging versus onboard computed tomography for anatomy visualization in radiotherapy. Acta Oncol 54:1474–1482.

O'Shea T, Bamber J, Fontanarosa D, van der Meer S, Verhaegen F, and Harris E (2016). Review of ultrasound image guidance in external beam radiotherapy part II: intra-fraction motion management and novel applications. Phys Med Biol 61:R90–R137.

Oborn BM, Dowdell S, Metcalfe PE, Crozier S, Mohan R, and Keall PJ (2015). Proton beam deflection in MRI fields: Implications for MRI-guided proton therapy. Med Phys 42:2113–2124.

Oborn BM, Metcalfe PE, Butson MJ, and Rosenfeld AB (2010). Monte Carlo characterization of skin doses in 6 MV transverse field MRI-linac systems: Effect of field size, surface orientation, magnetic field strength, and exit bolus. Med Phys 37:5208–5217.

Oborn BM, Dowdell S, Metcalfe PE, Crozier S, Guatelli S, Rosenfeld AB, Mohan R, and Keall PJ (Feb. 2016). MRI guided proton therapy: pencil beam scanning in an MRI fringe field. ICTR-PHE. Geneva, February 15-19.

Oborn BM, Dowdell S, Metcalfe PE, Crozier S, Mohan R, and Keall PJ (2017). Future of medical physics: real-time MRI guided proton therapy. Med Phys 44:e77–e90.

Ohara K, Okumura T, Akisada M, Inada T, Mori T, Yokota, and Calaguas MJ (1989). Irradiation synchronized with respiration gate. Int J Radiat Oncol Biol Phys 17:853–857.

Overweg JA (Nov. 2009). US 2011/0230754.

Overweg J (2006). MRI main field magnets. ISMRM Annual Meeting.

P Forthmann P A Jonas JAO (Dec. 2016). WO 2017/093434: Rotatable magnet for proton therapy. WIPO Patent Application.

Paciok E and Blümich B (2015). Outlook: Quo vadis NMR? In: Johns ML, Fridjonsson EO, Vogt SJ, and Haber A, (eds). *Mobile NMR and MRI*. Royal Society of Chemistry, p. 314.

Padilla-Cabal F, Georg D, and Fuchs H (2018). A pencil beam algorithm for magnetic resonance image-guided proton therapy. Med Phys 45:2195–2204.

Paganelli C, Lee D, Greer PB, Baroni G, Riboldi M, and Keall P (2015). Quantification of lung tumor rotation with automated landmark extraction using orthogonal cine MRI images. Phys Med Biol 60:7165.

Paganelli C, Whelan B, Peroni M, Summers P, Fast M, van de Lindt T, McClelland J, Eiben B, Keall P, Lomax T, Riboldi M, and Baroni G (2018). MRI-guidance for motion management in external beam radiotherapy: current status and future challenges. Phys Med Biol 63:22TR03.

Paganetti H (2011). The physics of proton biology. In: Paganetti H, (ed). *Proton Therapy Physics*. CRC Press, Taylor & Francis Group.

Paganetti H (2012). Range uncertainties in proton therapy and the role of Monte Carlo simulations. Phys Med Biol 57:R99–R117.

Paramed S.r.l (2010). MRI diagnostic device 01-2000-01 user manual.

Particle Therapy Co-Operative Group (2018). Particle therapy facilities in operation. Retrieved Sep 26, 2018. URL: `https://www.ptcog.ch/index.php`.

Paul H (2013). On the accuracy of stopping power codes and ion ranges used for hadron therapy. In: Belkic D, (ed). *Theory of Heavy Ion Collision Physics in Hadron Therapy*. Vol. 65. Advances in Quantum Chemistry. Academic Press.

Penning FM (1927). Über Ionisation durch metastabile Atome. Die Naturwissenschaften 15:818.

Phillips MH, Pedroni E, Blattmann H, Boehringer T, Coray A, and Scheib S (1992). Effects of respiratory motion on dose uniformity with a charged particle scanning method. Phys Med Biol 37:223–234.

Pimblott SM and LaVerne JA (2007). Production of low-energy electrons by ionizing radiation. Radiat Phys Chem 76:1244–1247.

Poludniowski G, Allinson NM, and Evans PM (2015). Proton radiography and tomography with application to proton therapy. Br J Radiol 88:20150134.

Price RR, Axel L, Newman TMR, Perman W, Schneiders N, Selikson M, Wood M, and Thomas SR (1990). Quality assurance methods and phantoms for magnetic resonance imaging: Report of AAPM nuclear magnetic resonance Task Group No. 1. Med Phys 17:287–295.

Prieels D, van der Kraaij E, Henrotin S, and Brusasco C (Oct. 2017a). 15/727,292: Apparatus and method for visualizing a hadron beam path traversing a target tissue by magnetic resonance imaging. US Patent Application.

Prieels D, van der Kraaij E, Henrotin S, and Brusasco C (Oct. 2017b). 15/727,379: Apparatus and method for localizing the Bragg peak of a hadron beam traversing a target tissue by magnetic resonance imaging. US Patent Application.

Purcell EM, Torrey HC, and Pound RV (1946). Resonance absorption by nuclear magnetic moments in a solid. Phys Rev 69:37–38.

Raaijmakers AJE, Raaymakers BW, and Lagendijk JJW (2005). Integrating a MRI scanner with a 6 MV radiotherapy linear accelerator: dose increase at tissue-air interfaces in a lateral magnetic field due to returning electrons. Phys Med Biol 50:1363–1376.

Raaymakers BW, Jürgenliemk-Schulz IM, Bol GH, Glitzner M, Kotte ANTJ, van Asselen B, de Boer JCJ, Bluemink JJ, Hackett SL, Moerland MA, Woodings SJ, Wolthaus JWH, van Zijp HM, Philippens MEP, Tijssen R, Kok JGM, de Groot-van Breugel EN, Kiekebosch I, Meijers LTC, Nomden CN, Sikkes GG, Doornaert PAH, Eppinga WSC, Kasperts N, Kerkmeijer LGW, Tersteeg JHA, Brown KJ, Pais B, Woodhead P, and Lagendijk JJW (2017). First patients treated with a 1.5 T MRI-Linac: clinical proof of concept of a high-precision, high-field MRI guided radiotherapy treatment. Phys Med Biol 62:L41–50.

Raaymakers BW, Raaijmakers AJE, and Lagendijk JJW (2008). Feasibility of MRI guided proton therapy: magnetic field dose effects. Phys Med Biol 53:5615–5622.

Rank CM, Hünemohr N, Nagel AM, Röthke MC, Jäkel O, and Greilich S (2013a). MRI-based simulation of treatment plans for ion therapy in the brain region. Radiother Oncol 109:414–418.

Rank CM, Tremmel C, Hünemohr N, Nagel AM, Jäkel O, and Greilich S (2013b). MRI-based treatment plan simulation and adaption for ion therapy using a classification-based approach. Radiat Oncol 8:1–13.

Reist H, Dolling R, Graf M, Pedroni E, Breiing A, Evertz J, and Schäpper D (2001). A fast degrader to set the energies for the application of the depth dose in proton therapy. PSI Scientific and Technical Report.

Reynolds M, Fallone BG, and Rathee S (2014). Dose response of selected solid state detectors in applied homogeneous transverse and longitudinal magnetic fields. Med Phys 41:092103.

Riboldi M, Orecchia R, and Baroni G (2012). Real-time tumour tracking in particle therapy: technological developments and future perspectives. Lancet Oncol 13:e383–e391.

Riemann L. 2018. Characterization of internal and external magnetic fields for an in-beam low-field MRI scanner at a proton therapy beamline. TU Dresden, MA thesis.

Rosenblatt E and Zubizarreta E (2017). Radiotherapy in cancer care: facing the global challenge. International Atomic Energy Agency.

Rudra S, Jiang N, Rosenberg SA, Olsen JR, Parikh PJ, Bassetti MF, and Lee P (2017). High dose adaptive MRI guided radiation therapy improves overall survival of inoperable pancreatic cancer. Int J Radiat Oncol Biol Phys 99:E184.

Ruschin M, Sahgal A, Tseng CL, Sonier M, Keller B, and Lee Y (2017). Dosimetric impact of using a virtual couch shift for online correction of setup errors for brain patients on an integrated high-field magnetic resonance imaging linear accelerator. Int J Radiat Oncol Biol Phys 98:699–708.

Rutherford E (1911). The scattering of α and β particles by matter and the structure of the atom. Philos Mag 6:21.

Samin A, Kurth M, and Ca LR (2015). An analysis of radiation effects on NdFeB permanent magnets. Nucl Instr Meth Phys Res B 342:200–205.

Schardt D, Steidl P, Krämer M, Weber U, Parodi K, and Brons S (2008). Precision Bragg-curve measurements for light-ion beams in water. GSI Scientific Report 2007:373.

Schellhammer SM, Matthes A, Pipek J, and Apostolakis J (2017). Problem 1879 - Segfault at magnetic field edges. retrieved Nov 15, 2016. URL: `https://bugzilla-geant4.kek.jp/show_bug.cgi?id=1879`.

Schellhammer SM and Hoffmann AL (2017). Prediction and compensation of magnetic beam deflection in MR-integrated proton therapy: A method optimized regarding accuracy, versatility and speed. Phys Med Biol 62:1548–1564.

Schellhammer SM, Hoffmann AL, Gantz S, Smeets J, van der Kraaij E, Quets S, Pieck S, Karsch L, and Pawelke J (2018a). Integrating a low-field open MR scanner with a static proton research beam line: proof of concept. Phys Med Biol 63:23LT01.

Schellhammer SM, Oborn BM, Lühr A, Gantz S, Bussmann M, and Hoffmann AL (2018b). Experimental verification of magnetic field induced beam deflection and Bragg peak displacement for MR-integrated proton therapy. Med Phys 45:3429–3434.

Schippers JM (2009). Beam Delivery Systems for Particle Radiation Therapy: Current Status and Recent Developments. Rev Accl Sci Tech 2:179–200.

Schippers JM and Lomax AJ (2011). Emerging technologies in proton therapy. Acta Oncol 50:838–850.

Schippers M (2011). Proton accelerators. In: Paganetti H, (ed). *Proton Therapy Physics*. CRC Press, Taylor & Francis Group.

Schmidt MA and Payne GS (2015). Radiotherapy planning using MRI. Phys Med Biol 60:R323–361.

Schneider U and Pedroni E (1995). Proton radiography as a tool for quality control in proton therapy. Med Phys 22:353–363.

Schulte R, Bashkirov V, Li T, Liang Z, Mueller K, Heimann J, Johnson LR, Keeney B, Sadrozinski HFW, Seiden A, Williams DC, Zhang L, Li Z, Peggs S, Satogata T, and

Woody C (2004). Conceptual design of a proton computed tomography system for applications in proton radiation therapy. IEEE Trans Nucl Sci 51:866–872.

Seco J, Robertson D, Trofimov A, and Paganetti H (2009). Breathing interplay effects during proton beam scanning: Simulation and statistical analysis. Phys Med Biol 54:N283–N294.

Serber R (1947). Nuclear reactions at high energies. Phys Rev 72:1114–1115.

Seregni M, Paganelli C, Summers P, Bellomi M, Baroni G, and Riboldi M (2016). A hybrid image registration and matching framework for real-time motion tracking in MRI-guided radiotherapy. IEEE Trans Biomed Eng 65:131–139.

Shen J, Tryggestad E, Younkin JE, Keole SR, Furutani KM, Kang Y, Herman MG, and Bues M (2017). Using experimentally determined proton spot scanning timing parameters to accurately model beam delivery time. Med Phys 44:5081–5088.

Shirato H, Suzuki K, and Sharp GC (2006). Speed and amplitude of lung tumor motion precisely detected in four-dimensional setup and in real-time tumor-tracking radiotherapy. Int J Radiat Oncol Biol Phys 64:1229–1236.

Shirato H, Shimizu S, Shimizu T, Nishioka T, and Miyasaka K (1999). Real-time tumour-tracking radiotherapy. The Lancet 353:1331–1332.

Simonetti O and Ahmed R (2017). Low field cardiac MRI: a compelling case for CMR's future. Circ Cardiovasc Imaging 10.

Spindeldreier CK, Schrenk O, Bakenecker A, Kawrakow I, Burigo L, Karger CP, Greilich S, and Pfaffenberger A (2017). Radiation dosimetry in magnetic fields with Farmer-type ionization chambers: determination of magnetic field correction factors for different magnetic field strengths and field orientations. Phys Med Biol 62:6708–6728.

Stemkens B, Glitzner M, Kontaxis C, De Senneville BD, Prins FM, Crijns SP, Kerkmeijer LG, Lagendijk JJ, van den Berg CAT, and Tijssen RHN (2017). Effect of intra-fraction motion on the accumulated dose for free-breathing MR-guided stereotactic body radiation therapy of renal-cell carcinoma. Phys Med Biol 62:7407–7424.

Stemkens B, Paulson ES, and Tijssen RHN (2018). Nuts and bolts of 4D-MRI for radiotherapy. Phys Med Biol 63:21TR01.

Stemkens B, Tijssen RHN, de Senneville BD, Heerkens HD, van Vulpen M, Lagendijk JJ, and van den Berg CA (2015). Optimizing 4-dimensional magnetic resonance imaging data sampling for respiratory motion analysis of pancreatic tumors. Int J Radiat Oncol Biol Phys 91:571–578.

Steward BW and Wild CP (2014). World cancer report. World Health Organization.

Stichelbaut F and Jongen Y (2003). Verification of the proton beam position in the patient by the detection of prompt gamma-rays emission. Abstract at 39th Meeting of the Particle Therapy Co-Operative Group.

Stokes GC (1951). On the effect of the internal friction of fluids on the motion of pendulums. Trans Cambridge Philos Soc II:8–106.

Suit H, Goldberg S, Niemierko A, Trofimov A, Adams J, Paganetti H, Chen GTY, Bortfeld T, Rosenthal S, Loeffler J, and Delaney T (2003). Proton beams to replace photon beams in radical dose treatments. Acta Oncol 42:800–808.

Thomas DH, Santhanam A, Kishan AU, Cao M, Lamb J, Min Y, O'Connell D, Yang Y, Agazaryan N, and Lee P (2018). Initial observations of intra-and inter-fractional motion variation in MR guided lung SBRT. Br J Radiol 91:20170522.

Trattnig S, Kontaxis G, Breitenseher M, Czerny C, Rand T, Turetschek K, Barth M, and Imhof H (1997). MRT auf Niederfeldtomographen (0,2 Tesla). Radiologe 37:773–777.

Tseung HWC, Ma J, and Beltran C (2015). A fast GPU-based Monte Carlo simulation of proton transport with detailed modeling of nonelastic interactions. Med Phys 42:2967–2978.

Turner B (2007). Shielding issues for medical products: basic magnetic shielding issues for MRI systems. ETS Lindgren.

Uh J, Krasin MJ, and Hua Ch (2018). Feasibility of MRI-based estimation of water-equivalent path length to detect changes in proton range during treatment courses. Med Phys 45:1677–1683.

Vavilov PV (1957). Ionization losses of high-energy heavy particles. Sov Phys JETP 5:749.

Veiga C, Janssens G, Teng CL, Baudier T, Hotoiu L, McClelland JR, Royle G, Lin L, Yin L, Metz J, Solberg TD, Tochner Z, Simone CB, McDonough J, and Teo BKK (2016). First clinical investigation of cone beam computed tomography and deformable registration for adaptive proton therapy for lung cancer. Int J Radiat Oncol Biol Phys 95:549–559.

Wachowicz K, Zanche ND, Yip E, Volotovskyy V, and Fallone BG (2016). CNR considerations for rapid real-time MRI tumor tracking in radiotherapy hybrid devices: Effects of B0 field strength. Med Phys 43:4903–4914.

Walker E and Nowacki AS (2011). Understanding equivalence and noninferiority testing. J Gen Intern Med 26:192–196.

Wang F, Flanz J, and Hamm R (2012). Injection study of the Radiance 330 synchrotron with a 1.6 MeV RFQ linac. AIP Conference Proceedings 1441:649.

Weinrich U (2006). Gantry design for proton and carbon hadrontherapy facilities. Proc EPAC 07:964–968.

Whelan B, Liney GP, Dowling JA, Rai R, Holloway L, McGarvie L, Feain I, Barton M, Berry M, Wilkins R, and Keall P (2016). An MRI-compatible patient rotation system - design, construction, and first organ deformation results. Med Phys 44:581–588.

Wiedemann H (2007). Particle Accelerator Physics. Springer-Verlag, Berlin Heidelberg.

Wohlfahrt P, Möhler C, Richter C, and Greilich S (2018). Evaluation of stopping-power prediction by dual- and single-energy computed tomography in an anthropomorphic ground-truth phantom. IJROBP 100:244–253.

Wolf R and Bortfeld T (2012). An analytical solution to proton Bragg peak deflection in a magnetic field. Phys Med Biol 57:N329–N337.

Yan S, Lu HM, Flanz J, Adams J, Trofimov A, and Bortfeld T (2016). Reassessment of the necessity of the proton gantry: analysis of beam orientations from 4332 treatments at the Massachusetts General Hospital proton center over the past 10 years. Int J Radiat Oncol Biol Phys 95:224–233.

Yuan Y, Andronesi OC, Bortfeld TR, Richter C, Wolf R, Guimares AR, Hong TS, and Seco J (2013). Feasibility study of in vivo MRI based dosimetric verification of proton end-of-range for liver cancer patients. Radiother Oncol 106:378–382.

Yun J, Yip E, Gabos Z, Wachowicz K, Rathee S, and Fallone BG (2016). Improved lung tumor autocontouring algorithm for intrafractional tumor tracking using 0.5 T linac-MR. Biomed Phys Eng Express 2:067004.

Zhang R and Newhauser WD (2009). Calculation of water equivalent thickness of materials of arbitrary density, elemental composition and thickness in proton beam irradiation. Phys Med Biol 54:1383–1395.

Zhang Y, Knopf AC, Weber DC, and Lomax AJ (2015). Improving 4D plan quality for PBS-based liver tumour treatments by combining online image guided beam gating with re-scanning. Phys Med Biol 60:8141–8159.

Zhang Y, Knopf A, Tanner C, and Lomax AJ (2014). Online image guided tumour tracking with scanned proton beams: a comprehensive simulation study. Phys Med Biol 59:7793–7817.

Zhao L and Das IJ (2010). Gafchromic EBT film dosimetry in proton beams. Phys Med Biol 55:N291–N301.

Ziegler J (1999). Stopping of energetic light ions in elemental matter. J Appl Phys 85:1249–1272.

Acknowledgement

"*Alone we can do so little,*
together we can do so much." (Helen Keller)

It is obvious that this work would not have been possible without the help of other people, and certainly impossible to adequately thank everyone who contributed, but the following is a futile attempt.

Firstly, I want to thank Wolfgang Enghardt for recommending me for this Ph.D. position and for being my official doctoral adviser and the first referee of this thesis. I have to admit I believe that only knowing that you would critically review this work has boosted its quality massively. Thank you for your support during the last years.

Secondly, I thank Oliver Jäkel for being my second thesis referee. Actually, it was your short lecture at a student orientation seminar in 2012 that made me switch gears from environmental physics to medical physics. Thank you. I am honoured that you have agreed to be the second referee of my Ph.D. thesis and hope you will enjoy reading it.

Thirdly, I thank Aswin Hoffmann for being my supervisor and group leader. It is incredible how much a Ph.D. student's fate depends on their supervisor, and you have taken this responsibiliy with grace. Thank you for the countless discussions, for your always comprehensive, precise and constructive feedback, for all your support regarding organisational and scientific issues, and for preparing the ground for this work to blossom.

I have been lucky to have two more remote supervisors, whom I'd like to thank. Michael Bussmann, thank you for introducing me to the world of Geant4 and for letting me become a temporary part of your research group. Bradley Oborn, thank you for helpful advice regarding Geant4 and MRiPT and, of course, for lending me your surfboard.

I want to thank my colleagues in Dresden, especially Sebastian Gantz, Armin Lühr, Pia Grossinger, Layla Riemann, Sergej Schneider, Sebastian Uber, Tom Päßler, Lukas Dünger, Leonhard Karsch, Jörg Pawelke, Malte Gotz, Patrick Wohlfahrt, Stefan Leger, Steffen Löck, Esther Troost, Carlchristian Eckert, Alexander Matthes, Erik Zenker, Richard Pausch, Flo-

rian Brack, Henrik Schulz, Andreas Gommlich, Konstantin Kuhne, Johannes Braun, Johannes Müller, Sona Michlikova, Theresa Werner, Johannes Petzold, Toni Kögler, Stephan Helmbrecht, Marleen Priegnitz, Benjamin Lutz, Jan Eulitz, Stefan Schmidt, Manfred Sobiella, Robert Schönert, Michael Kobel, and Gert Rothe – thank you for all of your help, be it personal or professional. I am blessed to call some of you my friends. A special thanks goes to the brave men who have proofread (parts of) this thesis, namely Aswin Hoffmann, Sebastian Uber, Bradley Oborn, Armin Lühr, Volker Hietschold, Jörg Pawelke, and Sebastian Gantz. I furthermore thank Daniela Kunath for the facility floor plan, Jan Eulitz and Patrick Wohlfahrt for depth dose data, and Susanna Guatelli, Brent Huisman, Andreas Resch and Loic Grevillot for their advice regarding Geant4.

Likewise, I thank the colleagues at Ion Beam Applications for the enjoyable and fruitful collaboration, especially Julien Smeets, Erik van der Kraaij, Sébastien Henrotin, Cosimo L'Abbate, Sébastien Quets, Damien Prieels, and Andreas Schumann. I furthermore thank the colleagues at Paramed, especially Andrea Serra and Leonardo Bertora, for their insightful support regarding MRI, as well as Lorenzo Scotto for shimming the magnet and Stefano Gazzo for support during MR image quality optimisation.

Thanks to all the people listed in the bibliography, whose scientific work I could build upon, and the remarkable researchers I could chat with during conferences. I also thank the people at stackoverflow, stackexchange and quora for their generous support. I am grateful to the volunteer and the patient who underwent the MR scans. I thank the OncoRay administration, our office team, the canteen around the corner, and all the other people working in the background.

Finally, I would like to express my gratitude towards my husband, Sebastian Schellhammer, and towards my family and friends for their love and support throughout these years.

Thank you.

Erklärungen zur Eröffnung des Promotionsverfahrens

1. Hiermit versichere ich, dass ich die vorliegende Arbeit ohne unzulässige Hilfe Dritter und ohne Benutzung anderer als der angegebenen Hilfsmittel angefertigt habe; die aus fremden Quellen direkt oder indirekt übernommenen Gedanken sind als solche kenntlich gemacht.

2. Bei der Auswahl und Auswertung des Materials sowie bei der Herstellung des Manuskripts habe ich Unterstützungsleistungen von folgenden Personen erhalten:
   Aswin Hoffmann, Sebastian Gantz, Sebastian Uber, Bradley Oborn, Wolfgang Enghardt, Armin Lühr, Jörg Pawelke, Volker Hietschold, Leonhard Karsch, Michael Bussmann.

3. Weitere Personen waren an der geistigen Herstellung der vorliegenden Arbeit nicht beteiligt. Insbesondere habe ich nicht die Hilfe eines kommerziellen Promotionsberaters in Anspruch genommen. Dritte haben von mir weder unmittelbar noch mittelbar geldwerte Leistungen für Arbeiten erhalten, die im Zusammenhang mit dem Inhalt der vorgelegten Dissertation stehen.

4. Die Arbeit wurde bisher weder im Inland noch im Ausland in gleicher oder ähnlicher Form einer anderen Prüfungsbehörde vorgelegt.

5. Die Inhalte dieser Dissertation wurden in folgender Form veröffentlicht:

   - Schellhammer SM und Hoffmann AL (2017). Prediction and compensation of magnetic beam deflection in MR-integrated proton therapy: A method optimized regarding accuracy, versatility and speed. Phys Med Biol 62:1548–1564
   - Schellhammer SM, Oborn BM, Lühr A, Gantz S, Bussmann M und Hoffmann AL (2018). Experimental verification of magnetic field induced beam deflection and Bragg peak displacement for MR-integrated proton therapy. Med Phys 45:3429–3434
   - Schellhammer SM, Hoffmann AL, Gantz S, Smeets J, van der Kraaij E, Quets S, Pieck S, Karsch L und Pawelke J (2018). Integrating a low-field open MR scanner with a static proton research beam line: proof of concept. Phys Med Biol 63:23LT01

6. Ich bestätige, dass es keine zurückliegenden erfolglosen Promotionsverfahren gab.
7. Ich bestätige, dass ich die Promotionsordnung der Medizinischen Fakultät Carl Gustav Carus der Technischen Universität Dresden anerkenne.
8. Ich habe die Zitierrichtlinien für Dissertationen an der Medizinischen Fakultät der Technischen Universität Dresden zur Kenntnis genommen und befolgt.

Dresden, 10. Januar 2019 _____

Erklärung über die Einhaltung der gesetzlichen Bestimmungen

Hiermit bestätige ich die Einhaltung der folgenden aktuellen gesetzlichen Vorgaben im Rahmen meiner Dissertation

☐ ~~das zustimmende Votum der Ethikkommission bei Klinischen Studien, epidemiologischen Untersuchungen mit Personenbezug oder Sachverhalten, die das Medizinproduktegesetz betreffen~~
nicht zutreffend

☐ ~~die Einhaltung der Bestimmungen des Tierschutzgesetzes~~
nicht zutreffend

☐ ~~die Einhaltung des Gentechnikgesetzes~~
nicht zutreffend

☐ ~~die Einhaltung von Datenschutzbestimmungen der Medizinischen Fakultät und des Universitätsklinikums Carl Gustav Carus.~~
nicht zutreffend

Dresden, 10. Januar 2019 _____

Supplementary Information

A Beam Deflection: Experimental Measurements

A.1 Setup

Protons were accelerated in the isochronous cyclotron to 235 MeV and then decelerated to the requested energy by a degrader (graphite wedge) and an energy selection system. The used beam current was 20 nA to 3 nA at the cyclotron for 80 MeV to 180 MeV, respectively, in this experiment.

The two brass collimators had a cylindrical shape with an outer radius of 9 cm and a combined thickness of 6.6 cm. This thickness allowed to fully stop peripheral protons for all used energies. They were placed in the beam line such that a symmetric beam profile was achieved behind the collimators. The distance between the beam exit window and the surface of the first collimator was 1.63 m, and that between the two collimators was 2 cm. The large air gap between the beam exit and the collimators was defined by the in-room laser system and improved the lateral beam homogeneity by scattering.

The phantom measured $x_{\mathrm{ph}} \times y_{\mathrm{ph}} \times z_{\mathrm{ph}} = 30 \times 15 \times 3$ cm^3. Its density was (1.186 $\pm$ 0.002) g cm^{-3} as measured by density determination scales. It was mounted into the air gap of the magnet assembly by an L-shaped holder (see Figure 3.10b). The two magnet poles had a density of 7.6 g cm^{-3} (Vacuumschmelze, 2014).

The tilt angle of the film ($\alpha = 1°$) was chosen as it rotated the measurement plane minimally out of the central beam plane whilst suppressing air gap effects as good as larger angles (Zhao and Das, 2010). With this angle, the inclination lead to differences in x below 0.02 mm. The air gap between the phantom and the film was minimized by four plastic screws pressing the slabs together.

Due to saturation of the film signal caused by the particles' increasing energy deposition per path length (LET), dose differences between predicted and measured dose increased towards the Bragg peak. The difference in the absolute Bragg peak dose was consistent

with the findings of previous studies (Zhao and Das, 2010; Arjomandy et al., 2012; Perles et al., 2013), and was not increased by the magnetic field. Thus, the introduction of a magnetic field did not compromise the dose prediction accuracy. However, simulated and measured dose was not directly comparable due to this effect.

A.2 Film Handling and Evaluation

Gafchromic EBT3 films (Ashland, Covington, USA; lot 05201501) cut in pieces of 20×15 cm^2 were used to measure the planar dose distribution of the beam. They were scanned with a flat-bed document scanner (Expression 11000XL, Epson America, Long Beach, CA) in landscape orientation, transmission mode, 24-bit color mode, and a resolution of 300 dpi. A stencil was used to ensure a reproducible positioning of the films on the scanner. Scanned images were analysed using in-house developed software written in the Python programming language (Python Software Foundation, www.python.org). The net optical density (netOD) was computed from the red channel pixel intensity I and background intensity I_0 for each pixel i as

$$\mathrm{netOD}_i = \log_{10} \frac{I_0}{I_i} \,, \tag{1}$$

and converted to dose using the calibration $D_i = k_1(\mathrm{netOD}_i) + k_2(\mathrm{netOD}_i)^{k_3}$ with $k_1 = 8.36$, $k_2 = 10.71$ and $k_3 = 1.84$. The calibration had been performed in analogy to a previous study (Zeil et al., 2009). The values of the first 30 pixels (2.55 mm) around film cutting edges were omitted.

Pixels were converted to x-y-coordinates as follows. Pixels were scaled with the image resolution, yielding a distribution on the film plane in x' and y'. The film tilt angle of $\alpha = 1°$ yielded $x = \cos(\alpha)x'$ and $y = y'$ (as mentioned above, $x - x' < 0.02$ mm within the film). The pinholes on the scanned images, whose x-y-positions are given by the manufacturer, were automatically detected on the scanned images and hence defined a translation and rotation of the dose distribution.

A.3 Uncertainty Estimation

The influence of the measurement uncertainties on the Bragg peak lateral deflection Δy_{80} and range retraction ΔR_{80} was assessed as follows (see Table A.1).

Statistical uncertainties such as the reproducibility of the determination of ΔR_{80} and Δy_{80}, and possible remaining displacement of the film relative to the phantom and to the scanner have been assessed by repeating the measurement for 180 MeV three times. Mean absolute deviations between the measurements were used as statistical uncertainties.

Film-to-film variations and the film calibration are subject to percentual dose uncertainties. The calibration has a relative dose uncertainty of 5 % (Zeil et al., 2009). Dose uncertainties due to film and scanner variations add up to 0.5 % (Sorriaux et al., 2012). Being proportional to the dose, these uncertainties were considered to have negligible influence on ΔR_{80} and Δy_{80}, which only depend on the relative dose difference between the measurement with and without magnetic field.

To assess the uncertainty of Δy_{80} and ΔR_{80} introduced by the LET-dependent saturation of the film response a polynomial correction function (Zhao and Das, 2010) was applied to the depth-dose curves. The uncertainty was estimated as the difference in ΔR_{80} and Δy_{80} between the corrected and uncorrected curves.

Systematic setup uncertainties are related to translational and rotational degrees of freedom. A rotation of the beam axis relative to the in-room laser system has a direct impact on the measured peak deflection. The alignment of the axes of the beam and the laser positioning system was energy-dependent and uncertain to within 0.1 °. The impact of this angle on Bragg peak retraction and deflection was assessed by purposefully rotating the dose distribution by this angle.

The reproducibility of the alignment of the magnet relative to the laser and of the phantom relative to the magnet were assessed by repeating the setup and irradiation procedure. For these two repeated experiments, the beam trajectory was determined for each depth as the mean of the two lateral positions receiving 10 % of the maximum dose. As no systematic dependence on the beam energy was observed in the deviations between the two experiments, mean absolute deviations were used as an estimate for this uncertainty. Rotations of the film relative to the phantom are statistical and therefore already covered.

Translational uncertainties of the setup in x-direction were considered to be negligible, as they mostly lead to uncertainties in the amount of air traversed. An exception to this is the uncertainty of the pin positions (see section 2), which was below 10 µm and therefore negligible. Translational uncertainties in y-direction were suppressed by subtracting the mean of the first proximal 10 values of the trajectory from $y_T(x)$. Proton beam deflection in

the magnetic fringe field outside of the magnet assembly was considered to be negligible.

Another factor of uncertainty was introduced by the spatial achromaticity of the incident beam, i.e. a y-z-dependent energy spectrum, caused by the beam line design. The initial proton energy spectrum at the beam exit tends to be higher-energetic in positive y-direction than in negative y-direction. This resulted in a kink towards the end of the trajectory $y_T(x)$, which lead to a small overestimation of the beam deflection. This effect was observed both with and without magnetic field. The kink was about 3 mm in x- and 0.2 mm in y-direction, translating into an uncertainty of the Bragg peak displacement below 0.01 mm in x- and of 0.2 mm in y-direction.

Relevant sources of uncertainty are summarized and quantified in Table A.1. The total uncertainty was estimated as the square root of the quadratic sum of the individual contributions.

Table A.1: Uncertainties of the measured lateral deflection Δy_{80} and longitudinal retraction ΔR_{80} of the Bragg peak. Lower and upper limits are given for energy-dependent effects, where lower energies are related to smaller uncertainties.

Source of uncertainty	ΔR_{80}/mm	Δy_{80}/mm
Statistical	0.4	0.2
Systematic	0.3 ... 0.4	0.4
Thereof:		
LET dependence	0.0 ... 0.2	0.0 ... 0.2
Setup axis alignment	0.3	0.3
Beam achromaticity	$<$ 0.01	0.2
Total	0.5	0.4 ... 0.5

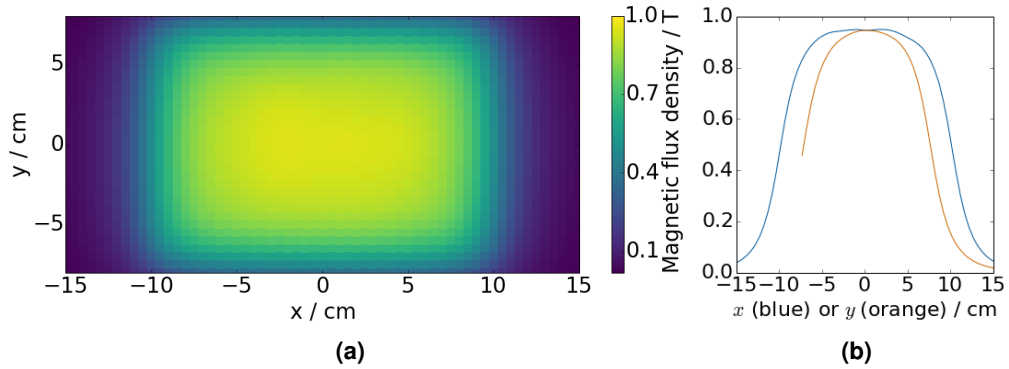

Figure B.1: Central plane of the measured magnetic field (a) and central field profiles (b) along the x-(blue) and y-(orange) axes. Values for $y > 7.5\,\text{cm}$ are not displayed due to the presence of the magnet yoke.

B Beam Deflection: Monte Carlo Simulations

B.1 Magnetic Field Model

A model of the magnetic field was generated using finite-element modelling (COMSOL Multiphysics, COMSOL AB, Stockholm, Sweden). The geometry of the magnet assembly was implemented as given by the manufacturer (Vacuumschmelze GmbH, Hanau, Germany) and surrounded by the pre-defined material 'Air'. The remanent field strength of the magnetic poles was set to $B_r = 1.37\,\text{T}$, as specified for the VACODYM 764 TP material by the manufacturer (Vacuumschmelze, 2014). The hysteresis curve $B(H)$ for the yoke was inherited from the COMSOL material library using the predefined material 'Soft Iron (without losses)'.

In air, the field of the magnet was mainly limited to the gap between its two poles, and had a maximum magnetic flux density of 0.95 T (see Figure B.1). A look-up-table (LUT) of the magnetic field was exported from the finite-element model with a grid spacing of 5 mm in a volume of $x_\text{B} \times y_\text{B} \times z_\text{B} = 70 \times 40 \times 20\,\text{cm}^3$. The LUT covered the three magnetic field components in the volume of $x \in [-50\,\text{cm}, 20\,\text{cm}]$ and $y \in [-20\,\text{cm}, 20\,\text{cm}]$ and $z \in [-10\,\text{cm}, 10\,\text{cm}]$ and thus contained the whole fringe field necessary to accurately predict beam deflection (Oborn et al., 2015).

The magnetic flux density maps of the main magnetic field predicted by the finite-element model and determined by the Hall probe measurements agreed within 2 %. The experimen-

tal verification of the modelled magnetic flux density maps is described in detail in Gantz (2017).

To monitor the temporal stability of the main field component, point measurements along the central x-axis at 5, 10 and 15 cm depth relative to the front face of the phantom were performed after each irradiation experiment. Deviations were within 3 mT, which was smaller than the measurement precision (4 mT), not systematic, and therefore considered negligible.

B.2 Uncertainty Estimation

To assess the influence of the different uncertainties of the simulations, a number of separate simulations were performed while varying the input parameters. For each of these uncertainty simulations, Δy_{80} and ΔR_{80} were extracted and compared to the original simulations (i.e. a sensitivity study was performed). All uncertainties were calculated for the lowest (80 MeV) and highest (180 MeV) energy used and interpolated linearly for intermediate energies.

Relevant systematic uncertainties of the input parameters were those of the initial proton energy E_0, of the density of the PMMA phantom ρ and of the main magnetic field component B_z. Each of these parameters was separately increased by its uncertainty (i.e. $E_0 + \Delta E_0$, $\rho + \Delta\rho$ and $B_z + \Delta B_z$) in an additional simulation to assess its influence on Δy_{80} and ΔR_{80}. It was assumed that the influence of the parameter uncertainties was equally large in positive and negative direction.

The uncertainty of the range measurements performed for section 3.2.2 amounted to 0.25 mm (Wohlfahrt et al., 2018). Using tabulated stopping-power data (Berger et al., 2005), this corresponded to an uncertainty of the beam energy E_0 of $\Delta E_0(80\,\text{MeV}) = 0.25\,\text{MeV}$ to $\Delta E_0(180\,\text{MeV}) = 0.15\,\text{MeV}$. The absolute uncertainty of the measured PMMA density amounted to $\Delta\rho = 0.002\,\text{g cm}^{-3}$, and that of the simulated magnetic field map to $\Delta B_z = 0.02\,\text{T}$.

Furthermore, there is an influence of systematic uncertainties which are inherent to the Monte Carlo simulation, for example in the physical process models and the mean excitation energy applied. As an estimate for this uncertainty, the range differences of the model to the reference measurements (section 3.2.2) of $\Delta R = 0.2\,\text{mm}$ was used. The influence of this range uncertainty on Δy_{80} and ΔR_{80}, was assessed by varying the initial energy

accordingly, i.e. with $\Delta E_0^R(80\,\text{MeV}) = 0.20\,\text{MeV}$ to $\Delta E_0^R(180\,\text{MeV}) = 0.12\,\text{MeV}$.

The statistical uncertainty of the simulation was estimated by repeating the original simulation five times with different random number seeds and calculating the standard deviation of Δy_{80} and ΔR_{80}. It was found that all simulations needed to be performed with $2.048 \cdot 10^7$ primary particles each to acquire a statistical uncertainty of the Bragg peak position of 0.1 mm or smaller.

The total uncertainty was estimated as the square root of the quadratic sum of the individual contributions.

Table B.1: Uncertainties of the predicted lateral deflection Δy_{80} and longitudinal retraction ΔR_{80} of the Bragg peak. Lower and upper limits are given for energy-dependent effects, where lower energies are related to smaller uncertainties.

Source of uncertainty	ΔR_{80}/mm	Δy_{80}/mm
Systematic	0.1 ... 0.2	0.1 ... 0.3
Thereof:		
Beam energy	0.1	0.0 ... 0.1
Phantom density	0.0	0.1
Magnetic field	0.0 ... 0.1	0.0 ... 0.2
Physics modelling	0.0 ... 0.1	0.0 ... 0.1
Statistical	0.0 ... 0.1	0.0 ... 0.1
Total	0.1 ... 0.2	0.1 ... 0.3

C Integrated MRiPT Setup

C.1 Magnetic Field Map

The measured magnetic field map in the central horizontal plane of the MR scanner is depicted in Figure C.1.

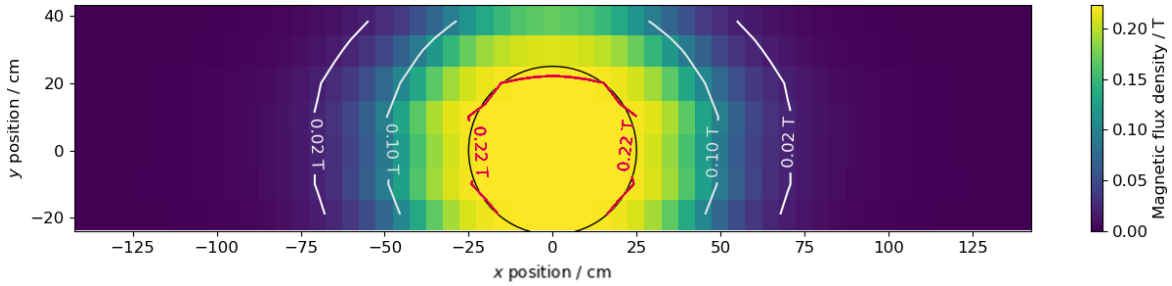

Figure C.1: Measured central horizontal plane of the static magnetic field of the MR scanner. $y = 0$ demarks the central beam axis. The black line demarks the homogeneous region of the field with a radius of about 25 cm.

C.2 Sequence Parameters

The MR sequence parameters for beam alignment and profile measurement are given in Table C.1. Sequence parameters for the qualitative in vivo and ex vivo tests are given in Table C.2.

Table C.1: MR spin echo (SE) and gradient echo (GE) sequence parameters for beam alignment (section 4.1.4) and beam profile measurement (section 4.2.1).

	Beam alignment	Beam profile		
Sequence	SCOUT SE	vertical SE	horizontal SE	vertical GE
FOV	26	12	12	12
Slice thickness / mm	8	5	5	5
Number of slices	1	1	1	1
Matrix	160 × 128	192 × 152	192 × 152	192 × 152
Number of excitations	1	1	1	1
Echo time / ms	18	20	20	8
Repetition time / ms	100	500	200	30
Flip angle / °	90	90	90	20
Acquisition time (min:s)	0:18	1:21	0:35	0:10
Pixel bandwidth / Hz	79	68	68	153

Table C.2: Pulse sequence parameters for extremity imaging and phantom irradiation (section 4.2.3).

	Anatomical images			Phantom irradiation
Sequence	STIR GE	T_1 GE	T_1 SE	T_1 SE
FOV	20	18	20	16
Interslice space /mm	5	4	4.5	3
Slice thickness / mm	4.5	3.5	4	5
Number of slices	14	11	20	3
Matrix	192×160	320×224	320×208	192×152
Number of excitations	1	1	1	4
Echo time / ms	16	16	24	20
Repetition time / ms	1003	510	962	500
Inversion time / ms	65	-	-	-
Flip angle / º	90	80	90	90
Acquisition time (min:s)	4:54	4:03	5:25	5:18
Pixel bandwidth / Hz	45	45	45	54

Table C.3: Image quality parameters for T_1-weighted SE sequence with and without simultaneous proton beam irradiation. Statistically equivalent parameters are marked by $^{\mathrm{eq}}$. Statistically significant differences are marked by an asterisk (*).

	ACR criterion	Without irradiation median (interquartile range)	During irradiation median (interquartile range)	Difference of medians
Phantom diameter in slice 1 / mm	100 ± 2	$99.8(99.7 - 100.0)$	$99.9(99.8 - 100.0)$	-0.1 $^{\mathrm{eq}}$
Phantom diameter in slice 3 / mm	100 ± 2	$100.0(100.0 - 100.0)$	$100.0(100.0 - 100.0)$	0.1 $^{\mathrm{eq}}$
Horizontal phantom centre / mm		$61.6(61.4 - 61.9)$	$61.4(61.4 - 61.8)$	0.2 $^{\mathrm{eq}}$
Vertical phantom centre / mm		$60(59.6 - 60)$	$59.7(59.5 - 60)$	0.3 $^{\mathrm{eq},*}$
Slice position error / mm	≤ 4	$0.8(0.2 - 1.4)$	$0.9(0.3 - 1.4)$	-0.2 $^{\mathrm{eq}}$
Slice thickness / mm	5.0 ± 0.7	$5.4(5.2 - 5.6)$	$5.5(5.2 - 5.6)$	-0.1 $^{\mathrm{eq}}$
SNR		$45.4(45.0 - 46.3)$	$44.8(43.7 - 46.0)$	0.6 $^{\mathrm{eq},*}$
Image Uniformity / %	≥ 87.5	$83.2(82.9 - 83.7)$	$83.1(82.3 - 83.5)$	0.1 $^{\mathrm{eq}}$
Ghosting Ratio / %	≤ 0.025	$0.054(0.053 - 0.057)$	$0.055(0.053 - 0.056)$	-0.001 $^{\mathrm{eq}}$
Number of detected low-contrast spokes	≥ 9	$13(10 - 13)$	$12(11 - 13)$	1 $^{\mathrm{eq}}$
Resolution horizontal / mm	≤ 0.8	$0.7(0.7 - 0.7)$	$0.7(0.7 - 0.7)$	0.0 $^{\mathrm{eq}}$
Resolution vertical / mm	≤ 0.8	$0.7(0.7 - 0.7)$	$0.7(0.7 - 0.7)$	0.0 $^{\mathrm{eq}}$

Table C.4: Image quality parameters for T_2-weighted SE sequence with and without simultaneous proton beam irradiation. Statistically equivalent parameters are marked by $^{\mathrm{eq}}$. Statistically significant differences are marked by an asterisk (*).

	ACR criterion	Without irradiation median (interquartile range)	During irradiation median (interquartile range)	Difference of medians
Phantom diameter in slice 1 / mm	100.0 ± 2	$99.8(99.7 - 100.0)$	$99.8(99.6 - 99.9)$	0.0 $^{\mathrm{eq}}$
Phantom diameter in slice 3 / mm	100.0 ± 2	$100.0(100.0 - 100.0)$	$100.0(99.9 - 100.0)$	-0.1 $^{\mathrm{eq}}$
Horizontal phantom centre / mm		$61.6(61.4 - 61.9)$	$61.6(61.4 - 61.9)$	0.0 $^{\mathrm{eq}}$
Vertical phantom centre / mm		$59.8(59.5 - 60.3)$	$59.8(59.3 - 60.1)$	0.0
Slice position error / mm	≤ 4	$0.9(0.4 - 1.4)$	$0.9(0.4 - 1.3)$	-0.1 $^{\mathrm{eq}}$
Slice thickness / mm	5.0 ± 0.7	$4.8(4.7 - 5.0)$	$4.8(4.7 - 4.9)$	0.0 $^{\mathrm{eq}}$
SNR		$47.3(46.6 - 47.6)$	$46.4(45.6 - 47.1)$	0.9 $^{\mathrm{eq},*}$
Image Uniformity / %	≥ 87.5	$76.5(75.9 - 77.1)$	$76.2(75.7 - 76.9)$	0.3 $^{\mathrm{eq}}$
Ghosting Ratio / %	≤ 0.025	$0.044(0.037 - 0.050)$	$0.045(0.036 - 0.052)$	-0.001
Number of detected low-contrast spokes	≥ 9	$11(10 - 12)$	$10(9 - 12)$	1 $^{\mathrm{eq}}$
Resolution horizontal / mm	≤ 0.8	$0.7(0.7 - 0.7)$	$0.7(0.7 - 0.7)$	0.0 $^{\mathrm{eq}}$
Resolution vertical / mm	≤ 0.8	$0.7(0.7 - 0.7)$	$0.7(0.7 - 0.7)$	0.0 $^{\mathrm{eq}}$

Table C.5: Image quality parameters for T_1-weighted GE sequence with and without simultaneous proton beam irradiation. Statistically equivalent parameters are marked by $^{\mathrm{eq}}$. Statistically significant differences are marked by an asterisk (*).

	ACR criterion	Without irradiation median (interquartile range)	During irradiation median (interquartile range)	Difference of medians
Phantom diameter in slice 1 / mm	100 ± 2	$99.8(99.7 - 99.8)$	$99.7(99.5 - 99.8)$	0.1 $^{\mathrm{eq}}$
Phantom diameter in slice 3 / mm	100 ± 2	$99.9(99.8 - 100.0)$	$99.9(99.7 - 100.0)$	0.0 $^{\mathrm{eq}}$
Horizontal phantom centre / mm		$61.6(61.4 - 61.9)$	$61.4(61.3 - 61.7)$	0.2 $^{\mathrm{eq}}$
Vertical phantom centre / mm		$60.0(59.9 - 60.2)$	$59.8(59.5 - 60.0)$	0.2 $^{\mathrm{eq},*}$
Slice position error / mm	≤ 4	$0.4(-0.1 - 1.0)$	$0.3(-0.2 - 0.6)$	0.1 $^{\mathrm{eq}}$
SNR		$14.2(13.3 - 15.3)$	$13.4(12.6 - 14.3)$	0.8
Image Uniformity / %	≥ 87.5	$88.0(83.8 - 92.7)$	$86.0(83.9 - 94.5)$	2.0 $^{\mathrm{eq}}$
Ghosting Ratio / %	≤ 0.025	$0.016(0.013 - 0.019)$	$0.015(0.013 - 0.017)$	0.000
Number of detected low-contrast spokes	≥ 9	$0(0 - 0)$	$0(0 - 0)$	0 $^{\mathrm{eq}}$
Resolution horizontal / mm	≤ 0.8	$0.8(0.8 - 0.8)$	$0.8(0.8 - 0.8)$	0.0 $^{\mathrm{eq}}$
Resolution vertical / mm	≤ 0.8	$0.8(0.7 - 0.8)$	$0.8(0.8 - 0.8)$	0.0 $^{\mathrm{eq}}$

Table C.6: Image quality parameters for T_2^*-weighted GE sequence with and without simultaneous proton beam irradiation. Statistically equivalent parameters are marked by $^{\mathrm{eq}}$. Statistically significant differences are marked by an asterisk (*).

	ACR criterion	Without irradiation median (interquartile range)	During irradiation median (interquartile range)	Difference of medians
Phantom diameter in slice 1 / mm	100 ± 2	$99.9(99.6 - 100.0)$	$99.9(99.7 - 100.0)$	0.0 $^{\mathrm{eq}}$
Phantom diameter in slice 3 / mm	100 ± 2	$100.0(99.3 - 100.0)$	$100.0(99.9 - 101.0)$	0.1
Horizontal phantom centre / mm		$61.9(61.6 - 62.0)$	$61.9(61.7 - 62.0)$	0.0 $^{\mathrm{eq}}$
Vertical phantom centre / mm		$59.6(58.7 - 60.2)$	$58.9(58.1 - 59.8)$	0.7 *
Slice position error / mm	≤ 4	$0.8(0 - 1.2)$	$0.9(0.1 - 1.1)$	-0.1 $^{\mathrm{eq}}$
Slice thickness / mm	5.0 ± 0.7	$5.7(5.5 - 5.9)$	$5.7(5.5 - 5.9)$	0.0 $^{\mathrm{eq}}$
SNR		$53.2(50.9 - 54.4)$	$51.7(49.2 - 52.6)$	1.5 *
Image Uniformity / %	≥ 87.5	$82.8(79.7 - 86.6)$	$82.6(81.0 - 85.1)$	0.2 $^{\mathrm{eq}}$
Ghosting Ratio / %	≤ 0.025	$0.097(0.080 - 0.111)$	$0.092(0.078 - 0.10)$	0.005
Number of detected low-contrast spokes	≥ 9	$1(1 - 2)$	$2(1 - 3)$	-1 $^{\mathrm{eq}}$
Resolution vertical / mm	≤ 0.8	$0.8(0.8 - 0.8)$	$0.8(0.8 - 0.8)$	0.0 $^{\mathrm{eq}}$
Resolution horizontal / mm	≤ 0.8	$0.8(0.8 - 0.8)$	$0.8(0.8 - 0.8)$	0.0 $^{\mathrm{eq}}$

Table C.7: Image quality parameter for the Locator SE sequence. The phantom length was statistically equivalent with and without irradiation (as indicated by $^{\mathrm{eq}}$).

	ACR criterion	Without irradiation median (interquartile range)	During irradiation median (interquartile range)	Difference of medians
Phantom Length / mm .	100 ± 2	$99.9(99.9 - 100)$	$100(99.9 - 100)$	-0.1 $^{\mathrm{eq}}$

C.3 Image Quality Parameters

The image quality parameters measured with and without simultaneous irradiation for the four sequences are given in the Tables C.3 to C.7.

C.4 Range Verification Sequences

The MR images acquired with the six tested sequences without simultaneous irradiation are given in Figure C.2.

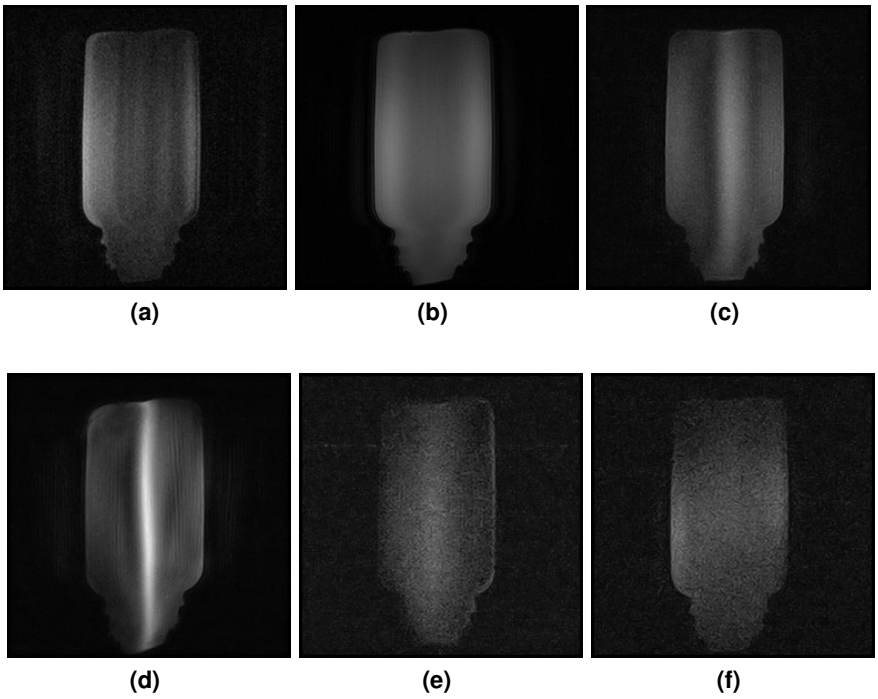

Figure C.2: Reference MR images for different sequences acquired without proton beam irradiation. (a) T_1-weighted SE, (b) T_2-weighted SE, (c) proton density-weighted GE, (d) T_2^*-weighted GE, (e) IR SE, and (f) IR GE sequence.